Chapter 5
Capillary forming of VA-CNT

In this Chapter I describe a methodology for the construction of robust three-dimensional (3D) assemblies of filamentary nanostructures by exploiting balances between elastic and capillary forces. Lithographically defined patterns of VA-CNTs are transformed into complex 3D architectures by self-directed capillary action initiated by liquid evaporation. I demonstrate the utility of this method, which we called *capillary forming*, via fabrication of a diverse library of CNT building blocks having complex geometries such as bending and twisting beams, conical wells and pins, and ordered foams. These building blocks have a higher packing fraction than as-grown VA-CNT microstructures and hence better electrical and mechanical properties. The manipulation of nanoscale filaments using local mechanical deformations facilitates the structural programming of complex surface architectures having spatially controlled geometry and properties, yet requires only standard two-dimensional patterning and ambient pressure thermal processing.

5. 1 Elastocapillary forces in micro- and nanofabrication

The elastocapillary effect is the deformation of solid elements due to the surface tension of a drying liquid. Aggregation of wet hair is a daily encountered example of elastocapillary effect (**Figure 5.1**).[1] On the other hand, aggregation and stiction of micro- and nanostructures due to capillary forces is a nuisance for fabrication of small structures.[2] For instance, in microfabrication, supercritical drying is used to avoid the sticton and collapse of thin structures by removing the liquid *via* the supercritical phase without going through the liquid-vapor phase transition of natural evaporation.[3] Recently, the dominance of interfacial over bulk forces at small length scales has become an important

tool to assemble and manipulate small structures in a local fashion (**Figure 5.1**). For instance, the force exerted by the surface of a wetting liquid has been used to fold planar films of polymers,[4] silicon and silicon nitride,[5] and to fabricate miniature photovoltaic devices. Surface forces of a melted solder droplet can act as hinges to fold polyhedral from planar copper and SU-8.[6-8]

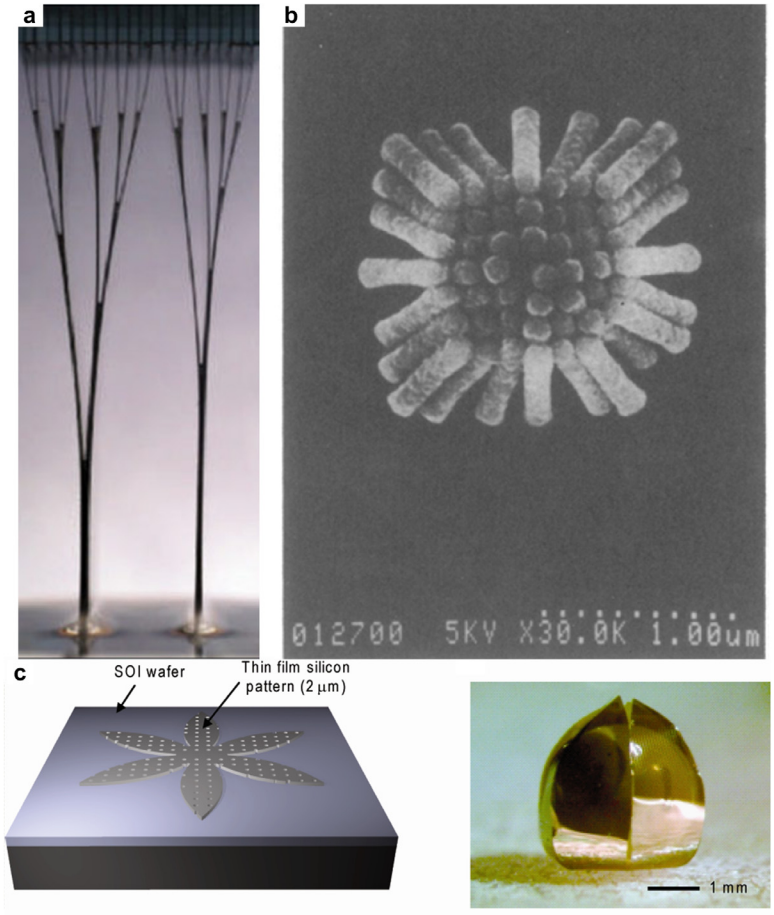

Figure 5.1 Elastocapillary effect in nature and microfabrication. (a) Elastocapillary coalescence of wet hair.[1] (b) Unwanted elastocapillary stiction in microfabrication.[2] (c) Elastocapillary origami for making three-dimensional Si substrates.[5]

Capillary forces were previously used to densify uniform CNT forests, however this led to the formation of complex CNT cellular foams instead of uniformly densified CNT solids (**Figure 5.2**).[9] The in-plane morphological structure of these foams can be controlled by patterning ordered voids in the forest. On the other hand, isolated VA-CNT microstructures with small feature size (10 -300 μm range) and high aspect ratio (1-10) aggregate into individual vertical bundles without any internal voids.[10] Further,

lithographically patterned thin gratings of VA-CNTs collapse into HA-CNT films due to capillary forces.[11] The direction of collapse is controlled by the direction of dipping and withdrawal from the solvent. For CNT microstructures of arbitrary cross section, capillary rise and solvent evaporation are affected by the cross section geometry and this results in densification, cross section shape change and geometry change along the vertical direction. Therefore, self-directed capillary action enables the formation of heterogeneous 3-D transformations programmed by the catalyst patterns. We call this process "*capillary forming*".[12]

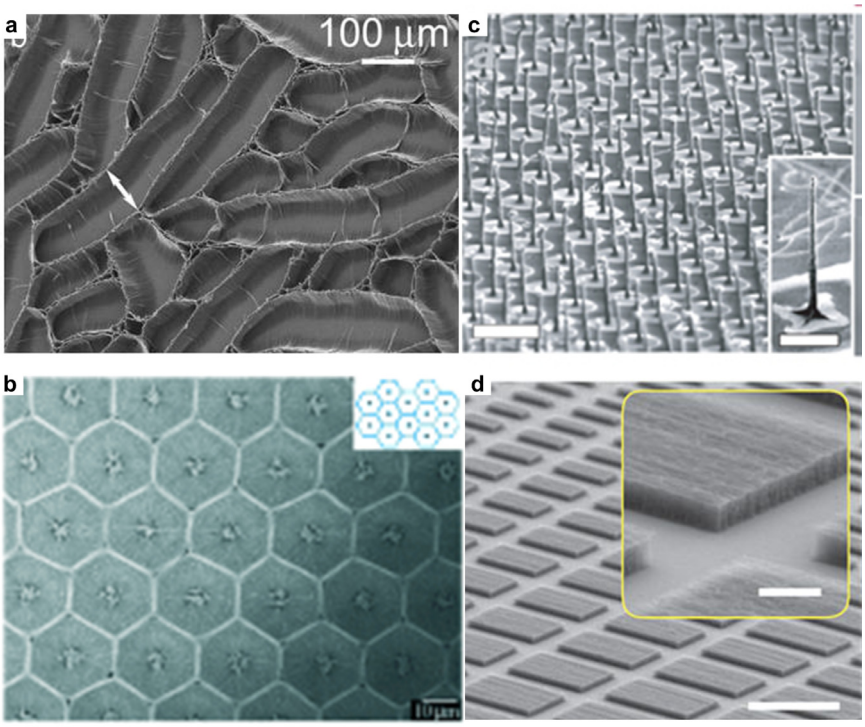

Figure 5.2 Elastocapillary aggregation of CNTs.(a) Formation of cellular foam from capillary densification CNT forest.[9] (b) Formation of uniform foam from capillary densification of patterned CNT forest.[13] (c) Densification VA-CNT microstructures by capillary forces.[10] (d) Formation of HA-CNT by capillary collapse.[11]

5. 2 Structural programming for capillary forming

Methods of capillary forming were developed in collaboration with Michael De Volder. VA-CNT microstructures are prepared on silicon substrates as described in Chapter 3. The samples are placed upside down on a metal mesh covering a beaker containing a boiling organic solvent such as acetone as shown in **Figure 5.3**. The

parameters of this step are set to cause the solvent vapor to condense on the substrate without pooling. The condensed liquid wets the CNTs by rising independently within each CNT microstructure due to capillary action (**Figure 5.4**). The solvent is subsequently set to evaporate which causes elastocapillary densification of the CNTs.

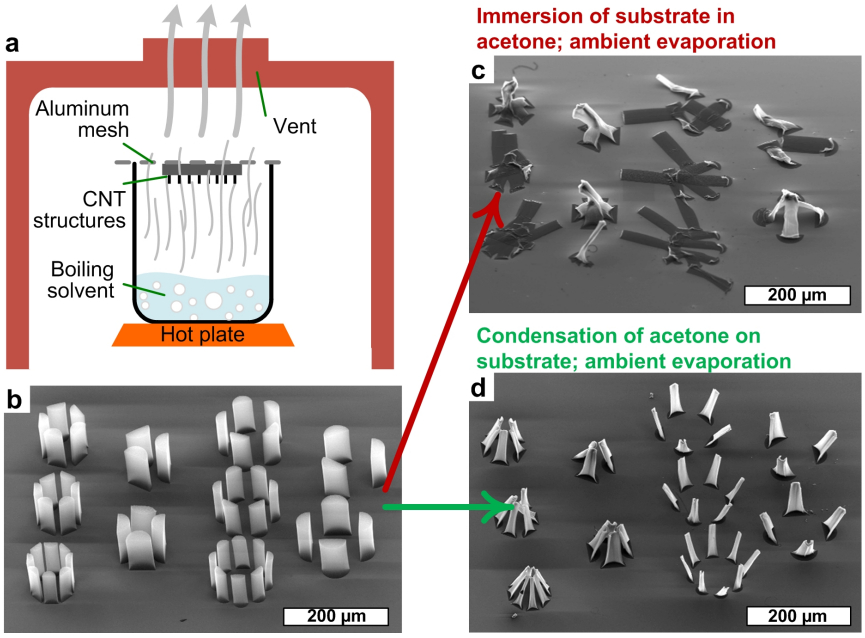

Figure 5.3 Capillary forming setup. (a) Schematic of setup for acetone condensation and evaporation from the substrates. (b) As-grown VA-CNT microstructures. (c) Structures in (b) collapsed after immersion in acetone. (d) Structures in (a) capillary formed after controlled acetone condensation and evaporation from the sample.

Although elastocapillary aggregation occurs locally within filamentary networks regardless of how the liquid is delivered, we found a critical difference between the known immersion method and our method of liquid delivery by condensation. First, as the sample breaks the liquid surface during immersion and/or withdrawal, non-uniform lateral forces cause small microstructures to collapse. Further, after withdrawal, large droplets are formed thus coupling closely spaced structures. This creates lateral forces that draw structures toward each other and/or the substrate. As a result, immersion detrimentally couples and flattens thin-walled and delicate CNT forests as shown in **Figure 5.3**. On the other hand, condensation of the liquid isolates the surface tension forces within each local group of filaments. Thus it allows the structures to be densified individually by self-directed capillary action and enables the formation of small closely

packed individual microstructures because the liquid does not bridge neighboring structures.

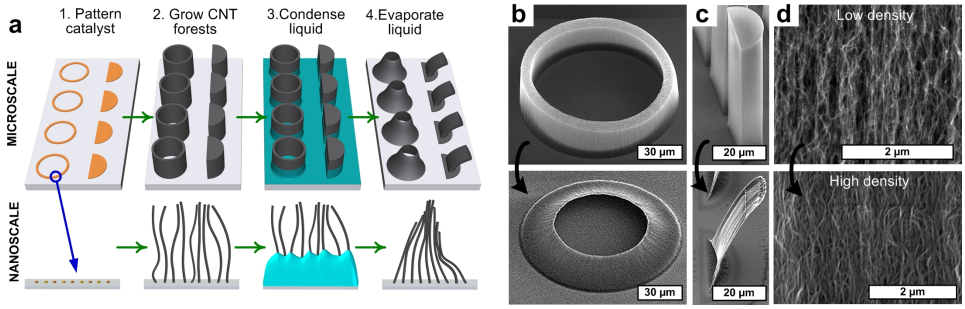

Figure 5.4 Method and mechanism of capillary forming of CNT microstructures. (a) Illustration of CNT forest growth and capillary forming method. **(b)** SEM images of hollow cylindrical (axisymmetric) and (c) semicylindrical (asymmetric) CNT microstructures before and after capillary forming. **(d)** SEM images showing the change in CNT density due to capillary forming.

Using this controlled condensation-evaporation process, we engineered a deterministic transformation from prismatic forests to robust 3D architectures. The created 3D geometries are determined by the 2D cross section shape of the VA-CNT microstructures as shown in **Figure 5.4**. Scanning Electron Microscope (SEM) is used to compare the morphology of CNT microstructures before and after this densification step, which reveals that the reduction of the cross-section area of the microstructure correlates to the decrease in the interspacing between individual CNTs .

5.2.1. Capillary forming of axisymmetric VA-CNTs

Upon liquid condensation and evaporation, surface tension causes the CNTs to aggregate locally according to the elastocapillary mechanism, and the forest globally contracts toward the centroid of its cross-sectional shape. Thus, for a circle, the contraction is toward the center; while for a semicircle, the contraction is toward the point at a distance $4R/3\pi$ from the straight edge of the semicircle (**Figure 5.4**). As this contraction occurs, the CNTs near the substrate are pulled inward toward the centroid; and because the CNTs are continuous through the forest, the contraction pulls down on the upper portions of the forest. For circles, the force distribution is axisymmetric and the final structure therefore slopes toward its apex. For semicircles, the force distribution

is asymmetric due to the asymmetric location of the centroid. This causes the structure to deflect laterally along its axis of symmetry, creating a curved beam.

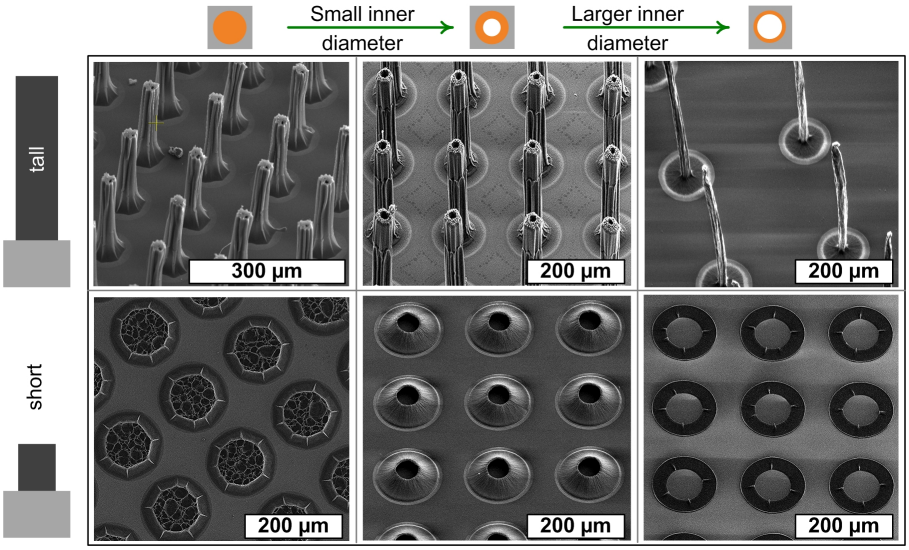

Figure 5.5 Map of capillary forming transformations of axisymmetric shapes showing the effect of CNT height for various inner/outer diameter values.

Design of annular catalyst patterns facilitates fabrication of sloped CNT micro-wells, which experience axisymmetric force distributions during capillary forming. Specifically, the displacement of the CNTs toward the center of the annulus depends on the height and the wall thickness of the annulus, as shown in **Figure 5.5**. Thin-walled tall cylinders (having aspect ratio L/R>4) contract forming needles with small inner diameter. If the walls are very thin, the annuli collapse forming solid pins. Short annuli (having aspect ratio L/R<1) fold inward and onto the substrate, creating circular thin films of radially oriented CNTs, while thick-walled annuli remain straight. Short solid cylinders form cellular foam with randomly organized voids. The array of sloped micro-wells in **Figure 5.6** emphasizes that capillary forming enables simultaneous fabrication of a large number of conical microwells having different wall inclination.

Figure 5.6 demonstrates exemplary catalyst shapes and arrangements of shapes that are transformed into complex micro-scale topologies which are difficult or impossible to make using known fabrication approaches. For instance, concentric annuli can be

designed to form structures with overhanging walls having different slopes, or radially-aligned sheets surrounding vertical needles.

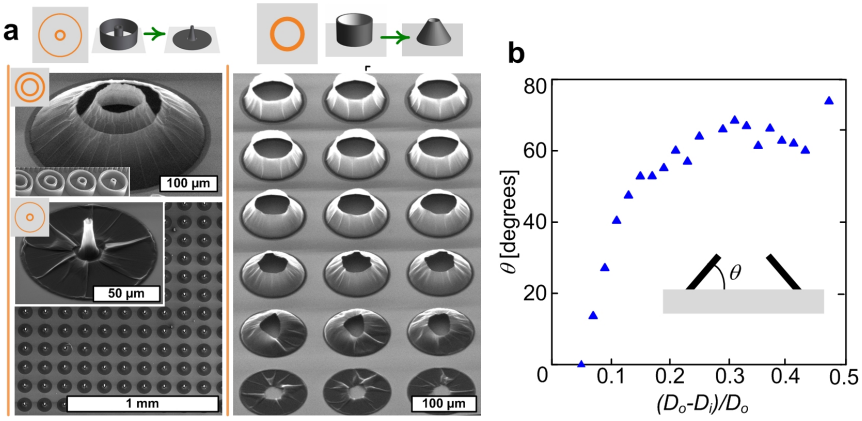

Figure 5.6 Programming inclination of conical wells by catalyst shape design (a) Arrays of heterogeneous conical wells with variable inclination angles. (b) Measured sidewall slope angles of the CNT conical wells shown in (a) (right).

5.2.2. Bending of asymmetric VA-CNTs

In contrast with axisymmetric shapes, asymmetric shapes such as semicircles and C-shaped annuli bend due to capillary forming. The mechanism leading to this geometrical transformation is discussed in more details in Chapter 6.[12, 14] Further, circular arrangements of bending structures resemble arrangements of flower petals, which can be designed to bend inward or outward from a common point, as shown in **Figure 5.7**. This demonstrates the self-directed bending as opposed to geometrical transformations caused by immersion into a liquid. The deflection angle of bent beams made by capillary forming of semiannular CNT forests depends precisely on the catalyst pattern design parameter *r,* where $r = R_i / R_o$. The deflection angle also depends on the amount of slip among the CNTs during capillary forming. Slip can be controlled by etching the top surface of the CNT forests before capillary forming, as discussed in Chapter 6.

5.2.3. Twisting and hierarchical assembly of asymmetric VA-CNTs

Intricate micro-helices with deterministic handedness are formed from shapes comprising semicircles merged with a thin annulus, as shown in **Figure 5.8**. These catalyst shapes combine the elementary motions of contraction and bending, and the helical angle and pitch of the final structure are determined by the dimensions of the catalyst shape. Additionally, polar arrays of CNT semicylinders wrap around each other

during densification, thus forming twisted micro-joints that resemble miniature yarns as shown in **Figure 5.8**. This programmed helicity is similar to the hierarchical twisting of polymer bristles studied by Pokroy et al.

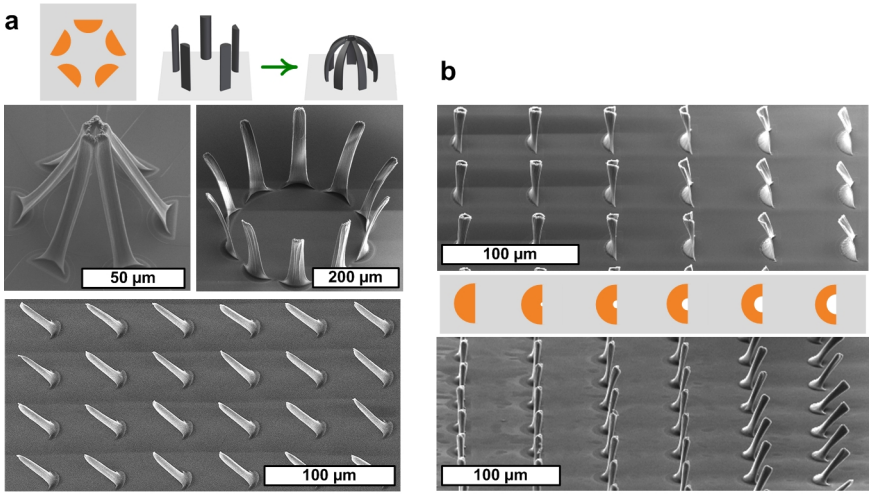

Figure 5.7 Bending of asymmetric CNT microstructures by capillary forming. (a) Blooming flowers" of radially-oriented bending CNT structures and large arrays of CNTs bending in the same direction. (b) Precise control of bending angle by catalyst shape design (shown in middle stripe).

Solid CNT forests with arrays of small holes are transformed to well-ordered cellular structures with sub-micron wall thickness. The circular holes are transformed to regular hexagons due to the interplay between the nonlinear stiffness modulus of the CNTs and the designed spacing between the holes as described in more details in Chapter 6.

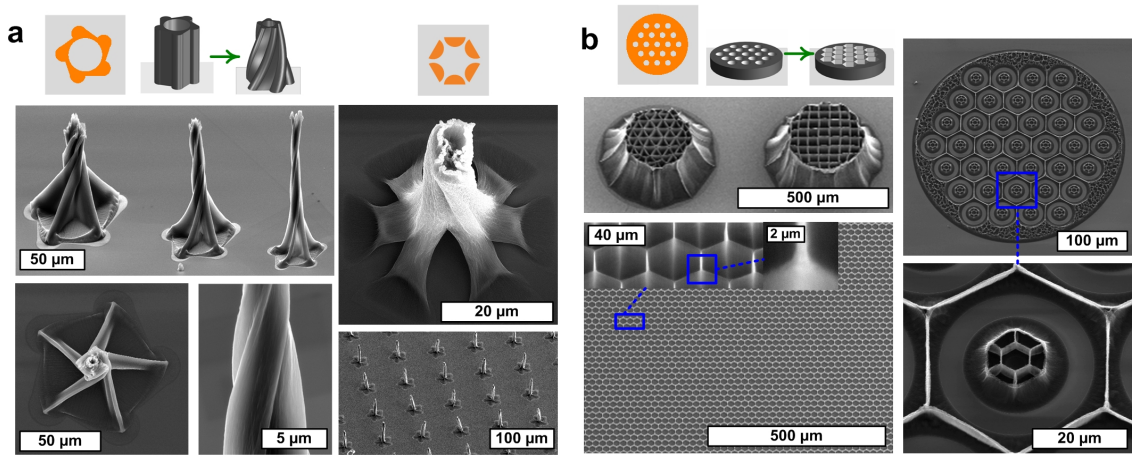

Figure 5.8 Fabrication of complex geometries by capillary forming. (a) Helical twisting of VA-CNTs due to coordinated bending and folding. (b) Uniform and hierarchical CNT cellular structures by lithographically designing void shape, size and spacing.

5. 3 Capillary folding of HA-CNTs

Self-directed wetting of vertically-aligned nanostructures enables folding of multi-directional anisotropic HA-CNT patches.[15] This strategy arose from my observation that patterned thin "walls" of vertically aligned CNTs (VA-CNTs) spontaneously fold when a solvent is condensed onto the substrate (**Figure 5.9**). Further, the folding direction can be controlled by lithographically patterning self-directing features that resemble arrows at the edges of the catalyst line that dictates the cross-sectional shape of the CNT wall. As a result, the folding transformation is structurally programmable via the geometric design of the catalyst pattern for CNT growth.

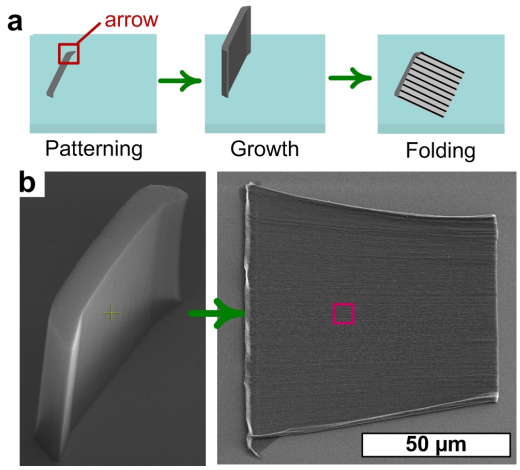

Figure 5.9 Fabrication of HA-CNT patches by structurally programmed capillary folding: (a) schematic of patterning, growth, and folding sequence; (b) SEM image of a thin wall of vertical CNTs before folding (left), and after folding (right).

The self-directed nature of capillary folding can also be exploited to create unique multi-directional and multi-layered CNT architectures. For example, arrays of rectangular HA-CNT "circuits" are made by patterning thin semicircular CNT walls that fold at right angles to one another (**Figure 5.10**). Compound structures such as three thin walls connected in an "I" shape fold to create an arrangement including overlapping HA-CNTs with perpendicular orientations. The transformation of the I-beam to a HA-CNT patch also tears the structure internally at the location of greatest lateral stress. Indeed, exploiting the size-dependent dynamics of liquid infiltration into CNT walls of different dimensions enables deterministic fabrication of overlapping folded patterns having orthogonal textures (**Figure 5.10**). This shows how the capillary folding method can overcome the serial nature of multi-step printing or sequential patterning methods, and achieve multi-directional architectures in a self-registered fashion. Finally, combinations of folding CNT walls with larger CNT structures which remain vertical during elastocapillary densification result in even more complex arrangements, comprising both horizontal and vertical CNTs having engineerable orientation in three dimensions (**Figure 5.11**).

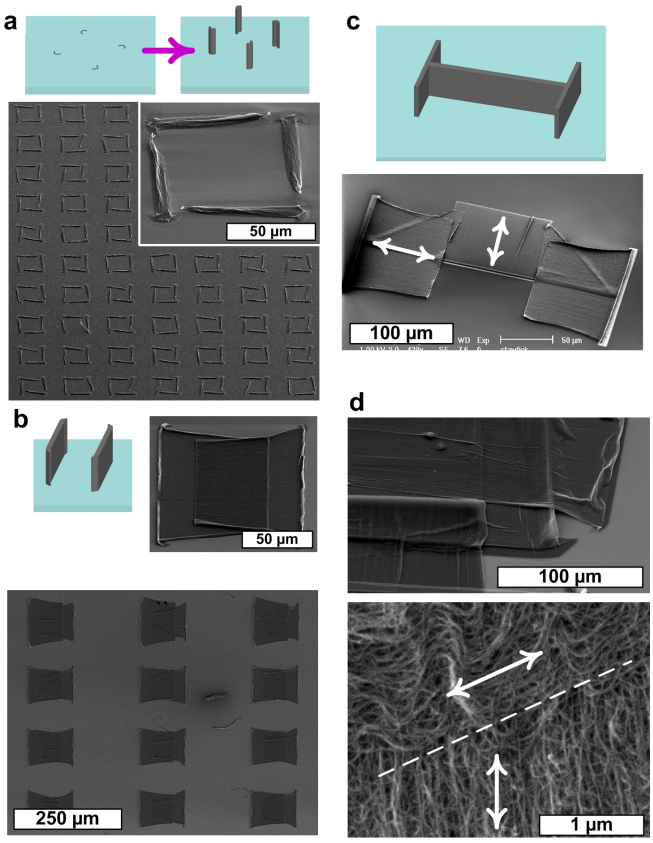

Figure 5.10 Multi-layered and multi-directional CNT networks. (a) Rectangular circuits of HA-CNTs. (b) Folding of HA-CNTs facing in opposite directions. (c) Folded I-beam with multi directional CNT orientation. (d) Multidirectional and multilayered CNTs with SEM showing the overlapping CNTs aligned in different directions.

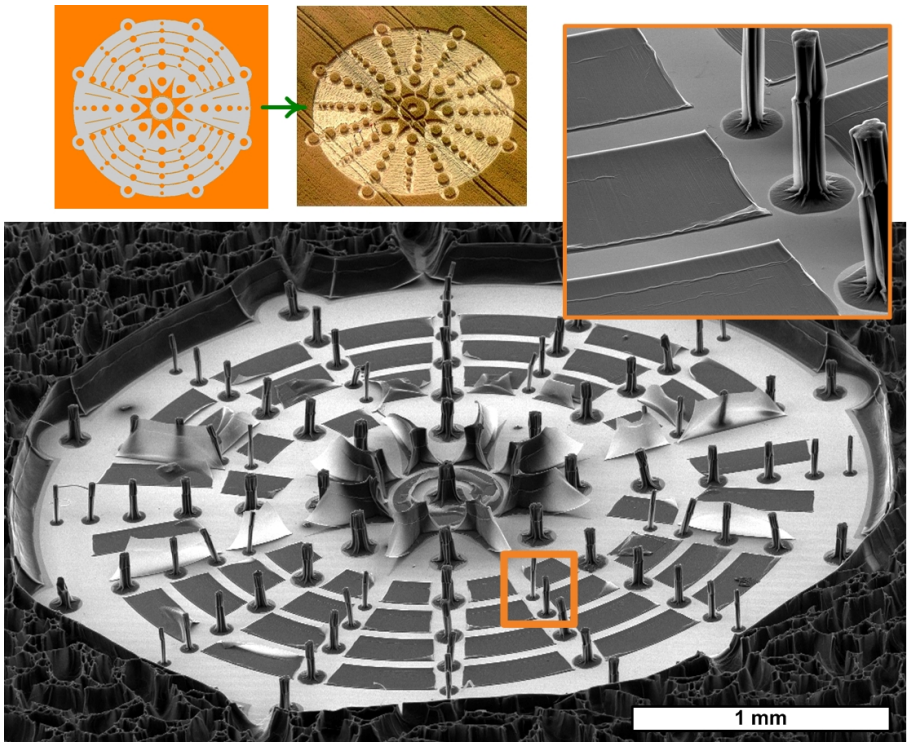

Figure 5.11 A micro CNT crop circle made by precisely folding HA-CNTs and forming VA-CNTs.

5. 4 Bibliography

1. Bico, J.; Roman, B.; Moulin, L.; Boudaoud, A., Elastocapillary coalescence in wet hair. *Nature* **2004,** *432* (7018), 690-690.

2. Tanaka, T.; Morigami, M.; Atoda, N., Mechanism of Resist Pattern Collapse. *Journal of The Electrochemical Society* **1993,** *140* (7), L115-L116.

3. Maboudian, R.; Howe, R. T., Stiction reduction processes for surfacemicromachines. *Tribology Letters* **1997,** *3* (3), 215-221.

4. Py, C.; Reverdy, P.; Doppler, L.; Bico, J.; eacute; Roman, B.; icirc; Baroud, C. N., Capillary Origami: Spontaneous Wrapping of a Droplet with an Elastic Sheet. *Physical Review Letters* **2007,** *98* (15), 156103.

5. Guo, X.; Li, H.; Yeop Ahn, B.; Duoss, E. B.; Hsia, K. J.; Lewis, J. A.; Nuzzo, R. G., Two- and three-dimensional folding of thin film single-crystalline silicon for photovoltaic power applications. *Proceedings of the National Academy of Sciences* **2009,** *106* (48), 20149-20154.

6. Leong, T. G.; Lester, P. A.; Koh, T. L.; Call, E. K.; Gracias, D. H., Surface Tension-Driven Self-Folding Polyhedra. *Langmuir* **2007,** *23* (17), 8747-8751.

7. Leong, T. G.; Benson, B. R.; Call, E. K.; Gracias, D. H., Thin Film Stress Driven Self-Folding of Microstructured Containers. *Small* **2008,** *4* (10), 1605-1609.

8. Azam, A.; Laflin, K.; Jamal, M.; Fernandes, R.; Gracias, D., Self-folding micropatterned polymeric containers. *Biomedical Microdevices* **2011,** *13* (1), 51-58.

9. Chakrapani, N.; Wei, B. Q.; Carrillo, A.; Ajayan, P. M.; Kane, R. S., Capillarity-driven assembly of two-dimensional cellular carbon nanotube foams. *Proceedings of the National Academy of Sciences of the United States of America* **2004,** *101* (12), 4009-4012.

10. Futaba, D. N.; Hata, K.; Yamada, T.; Hiraoka, T.; Hayamizu, Y.; Kakudate, Y.; Tanaike, O.; Hatori, H.; Yumura, M.; Iijima, S., Shape-engineerable and highly densely packed single-walled carbon nanotubes and their application as super-capacitor electrodes. *Nat Mater* **2006,** *5* (12), 987-994.

11. Hayamizu, Y.; Yamada, T.; Mizuno, K.; Davis, R. C.; Futaba, D. N.; Yumura, M.; Hata, K., Integrated three-dimensional microelectromechanical devices from processable carbon nanotube wafers. *Nature nanotechnology* **2008,** *3*, 289-94.

12. De Volder, M.; Tawfick, S. H.; Park, S. J.; Copic, D.; Zhao, Z. Z.; Lu, W.; Hart, A. J., Diverse 3D Microarchitectures Made by Capillary Forming of Carbon Nanotubes. *Advanced Materials* **2010,** *22* (39), 4384-4389.

13. Liu, H.; Li, S.; Zhai, J.; Li, H.; Zheng, Q.; Jiang, L.; Zhu, D., Self-Assembly of Large-Scale Micropatterns on Aligned Carbon Nanotube Films. *Angewandte Chemie International Edition* **2004,** *43* (9), 1146-1149.

14. Zhao, Z.; Tawfick, S. H.; Park, S. J.; De Volder, M.; Hart, A. J.; Lu, W., Bending of nanoscale filament assemblies by elastocapillary densification. *Phys. Rev. E* **2010,** *82* (4), 041605.

15. Tawfick, S.; De Volder, M.; Hart, A. J., Structurally Programmed Capillary Folding of Carbon Nanotube Assemblies. *Langmuir* **2011,** *27* (10), 6389-6394.

Chapter 6
Mechanism of capillary forming

This chapter describes the mechanism of capillary forming. In situ imaging is combined with wetting theories to elucidate how local and global capillary forces cause the geometric transformation of VA-CNT microstructures. Capillary forming comprises three stages: self-directed capillary rise during condensation; evaporation of liquid from the substrate; and densification upon liquid evaporation from the CNT microstructures. Condensation induced capillary filling of the solvent **inside** the microstructures has little effect on the final geometry or structural characteristics of VA-CNT microstructures. The self-directed capillary rise of the solvent **around** the microstructure depends on the curvature of the boundary, and this influences both symmetric and asymmetric shapes that remain straight, or bend, respectively. Specifically, asymmetric rise exerts forces that can deform thin microstructures, such as by causing bending or buckling of thin vertical columns. As the liquid evaporates, the liquid-air interface migrates inwards, causing densification of the VA-CNTs. Hence, motion of the liquid as it passes **inside** the microstructures is the dominant driver of reduction in cross-sectional area which is viewed as densification of the microstructure. The final geometry also depends on the normal and shear stresses created as the CNTs are deformed, and the corresponding material properties of the VA-CNTs. Thus, the geometric transformations are influenced by the internal structure of the CNT forests, including the CNT diameter, straightness, and packing density. This is verified by experiments that modify the CNT forest structure to change these properties independently or in concert.

6. 1 Capillary forming building blocks

Capillary forming causes transformations in the structural characteristics and the geometry of VA-CNT microstructures. These transformations are:

- Densification due to local CNT aggregation
- Change of the cross-section shape due to collective CNT motion
- Inclination due to bending (changes in the Zenith angle)
- Folding due to buckling (90° change in the Zenith angle)
- Twisting due to coordinated bending (changes in the Azimuth angle)

Figure 6.1 illustrates how these transformations are programmed by the cross-sectional shape of the starting CNT microstructure. Four building blocks relate the transformations described above to the catalyst shape design: axisymmetric, symmetric, asymmetric, and thin shapes. Further, by understanding these building blocks, novel shapes can be designed leading to more complex transformations such as twisting due to coordinated bending and buckling.

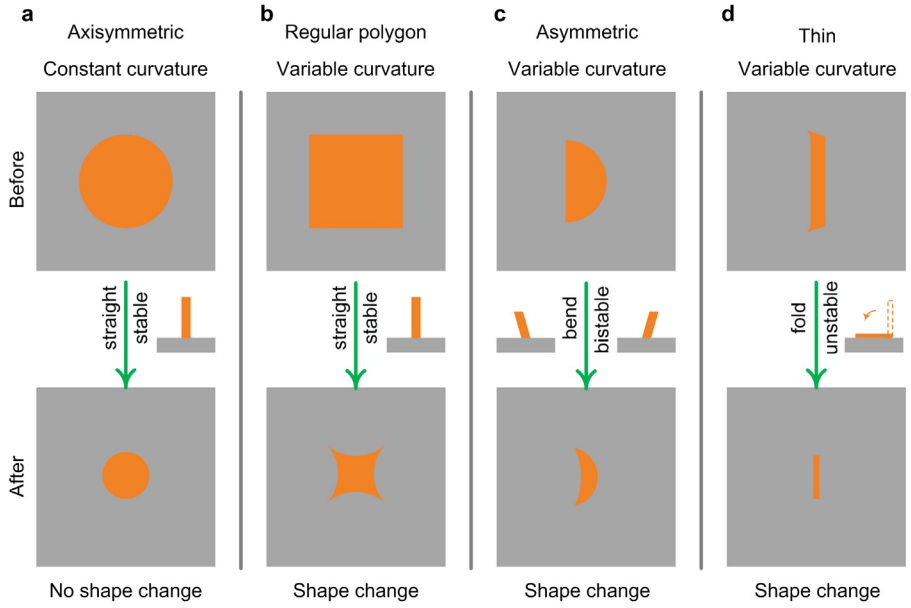

Figure 6.1 Capillary forming building blocks. (a) Axisymmetric. (b) Regular polygons. (c) Asymmetric. (d) Thin shapes.

The building blocks are described next, and the mechanisms of their transformations which were studied by in situ and ex situ experiments are described in the following sections.

Axisymmetric shapes:
This shape has full circular symmetry. Solid cylindrical CNT microstructures experience axisymmetric forces, and as a result these shapes don't change cross section[1] or inclination angle during capillary forming. Circular cross sections uniformly shrink due to local CNT aggregation and global CNT migration towards the center. The CNT migration towards the center results from the meniscus shrinking during evaporation as discussed later in this chapter.

Regular polygons:
These shapes have (i) mirror symmetry[2] and (ii) n-fold rotation symmetry where n>2. Thus it has corners or variable radii of curvature along its circumference. As a result, CNT microstructures these geometries undergo a change in cross-section shape during capillary forming but don't change their inclination. For a square (n=4), the liquid surface tension and the nonlinear stiffness of the CNTs cause the formation of sharper corners (**Figure 6.1**) for during capillary forming. All regular polygons hence belong to this category (e.g. equilateral triangle (n=3), regular pentagon (n=5), hexagon (n=6), etc.).

Asymmetric shapes:
These shapes have mirror symmetry but no rotational axes of symmetry. External asymmetric forces from the meniscus and internal stresses in the CNTs cause this shape to bend parallel to the plane of symmetry. Further, the corners become sharper during evaporation. Semi-annular and crescent shapes belong to this category.

[1] Wrinkling of circular cross section is a nonlinear buckling effect beyond the scope of this discussion
[2] This conditions insures that this building block doesn't twist during capillary folding

Thin shapes:

Thin asymmetric shapes are asymmetric shapes but with high aspect ratio. These shapes become mechanically unstable due to capillary forces and fold over to the substrate due to buckling. The design of these shapes predicts the folding direction.

6. 2 Dynamics of capillary forming

Capillary forming dynamics are studied by *in situ* imaging experiments. These experiments show that capillary forming occurs in three stages: liquid condensation and self-directed capillary rise; liquid evaporation from the substrate; and liquid evaporation from the CNT microstrcutures. The geometric transformations mainly occur during the third stage as shown in the schematic and video snapshots of **Figure 6.2**.

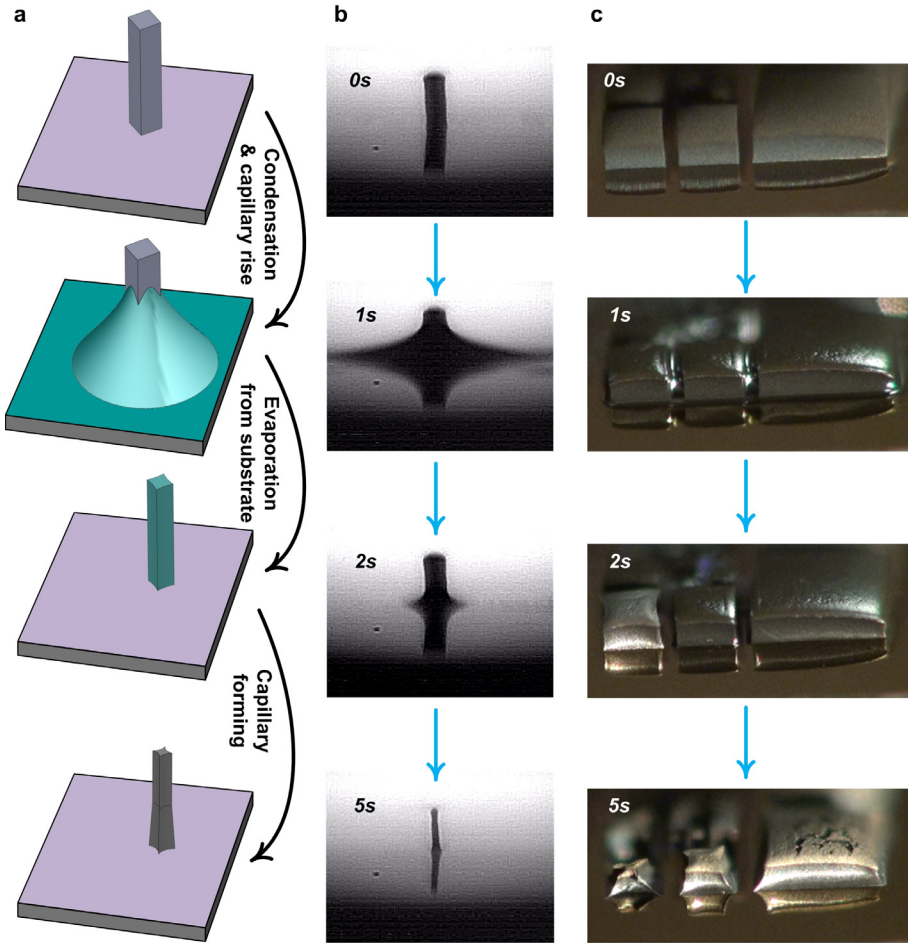

Figure 6.2 *In situ* dynamics of capillary forming showing solvent condensation and evaporation. (a) Schematic. (b) Optical side view snapshots.(c) Optical isometric view snapshots.

6.2.1. Solvent condensation and evaporation

Figure 6.2b shows the time evolution of a 100 μm square CNT microstructure imaged from a side view. In this experiment, a 10μL droplet of acetone is carefully deposited approximately 5 mm from the CNT square pillar. The droplet wets and spreads over the substrate until it reaches the CNT microstructure. Then, the acetone wets the CNT microstructure, and the meniscus rises inside and around the structure. This is the first stage of capillary forming. Similar results are obtained using different experimental conditions and a different imaging system as shown in **Figure 6.2c**. Capillary forming is imaged using Sony HDR-CX700V. A 32-dopter macrolens from Raynox (model MSN 505) is directly mounted on the camcorder using the built-in filter thread mount. In the experiments of **Figure 6.2c**, acetone is condensed onto the substrate by placing the sample close to the opening of a tilted flask. The second snapshot from the top also shows that as condensation on the substrate proceeds, a meniscus is formed around the edges of the CNT microstructures. Thus, during condensation at ambient conditions and subsequent capillary rise, the changes in shape are small, especially for features > 50 μm.

6.2.2. Self-directed capillary rise

The changes in geometry during this stage are caused by local capillary forces acting among the CNTs and surfaces forces acting on the edges of the CNT microstructure body. When a liquid rises against a solid surface, the height depends on the local radius of curvature.[1] Examples of how the height of capillary rise depends on the radius of curvature of the perimeter are shown in **Figure 6.3.** Capillary rise is related to capillary pressure by the resulting radius of curvature of the meniscus (Eq. 6.1)

$$\Delta P = \gamma\left(\frac{1}{R} + \frac{1}{R'}\right) \tag{6.1}$$

where ΔP is the pressure difference which results in the capillary rise, γ is the liquid surface tension, R and R' and the radii of curvature in two orthogonal planes where the center is always considered to be inside the meniscus. For instance, R and R' have the same sign inside tubes and opposite signs outside and hence the capillary rise outside the tube is smaller.

Figure 6.3 shows four basic cases illustrating the capillary rise height on bodies with the following geometrical features: positive and negative curvature, straight edges, and inclined edges. It illustrates that the height of capillary rise inside a hollow tube is much higher than the rise outside the tube. We observe this is the case with CNT microstructures, even though the liquid infiltrates the porous interior. **Figure 6.4** shows an SEM of a CNT microstructure with square cross section. In this experiment, the condensation of solvent was stopped prematurely which results in partial capillary rise and solvent infiltration. As a result, this image clearly illustrates the dynamics of capillary rise and confirms the profile of the liquid at the edges. It also shows that little densification occurs as the liquid partially infiltrate the structures.

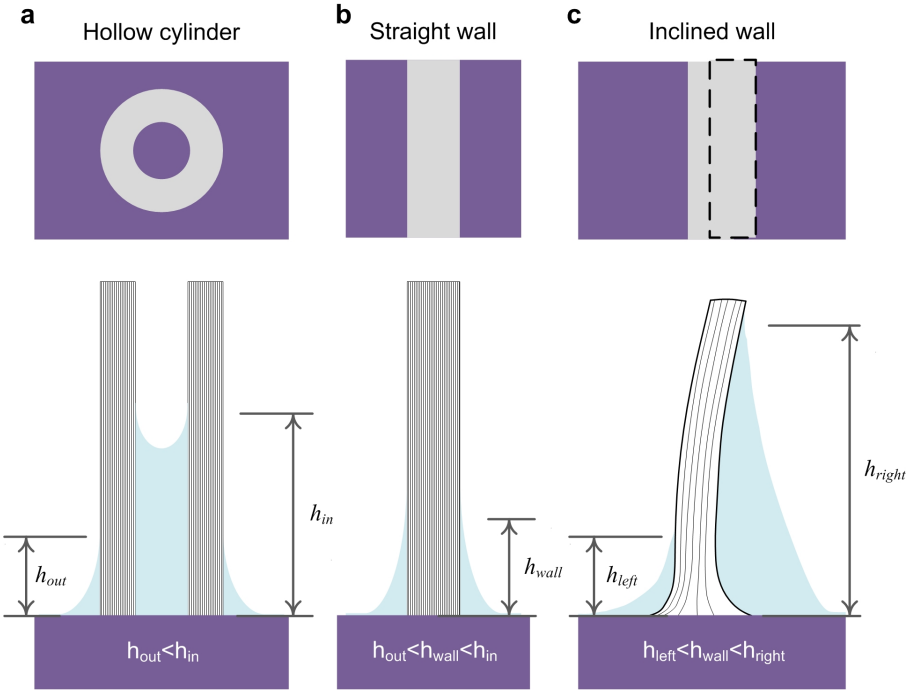

Figure 6.3 Capillary rise around various geometries. (a) Rise in and outside tubes. (b) Rise on straight infinite walls. (c) Rise on inclined infinite walls.

It is noteworthy to indicate that the microstructures are porous due to the low density of the VA-CNTs. Hence, accurate estimation of the capillary rise height and profile around their edges must take into consideration the longitudinal porosity. Establishing a detailed model of capillary rise around the edges of CNT-microstructures is a future direction which can lead to more in depth understanding and control of capillary forming.

6.2.3. In situ capillary forming of conical wells

In situ capillary forming experiments were also conducted at low pressure and temperature in the Environmental Scanning Electron Microscope (ESEM).[2] **Figure 6.5** shows the top view of a hollow cylindrical CNT microstructure (outer diameter 300 μm, inner diameter 240 μm, height 130 μm). A flask of 2-propanol was heated to 60°C and connected to the chamber *via* a computer controlled valve. The CNT substrate was mounted on a thermoelectric stage inside the chamber. The ESEM chamber is sealed and evacuated to a pressure < 10^{-2} Torr. The substrate was then cooled[3] to -2°C by the thermoelectric chip. The hot side of the chip was cooled by water circulation connected through vacuum tight tube fittings to the cold water bath located outside the chamber. The valve to the 2-propanol flask was gradually opened and the pressure of the chamber was increased until condensation starts (≈13.5 Torr). The pressure of the chamber was gradually raised to 19 Torr.

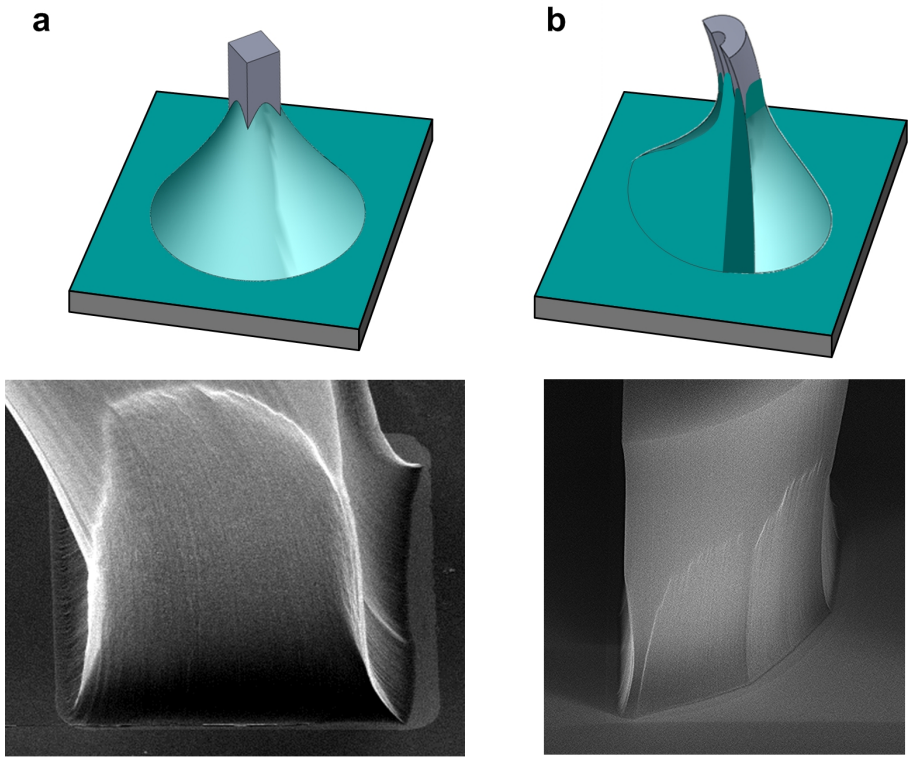

Figure 6.4 Capillary rise around various VA-CNT geometries. Rise profile on (a) square and (b) circular microstructures.

[3] The cooling must start at low pressure otherwise ambient water vapor would condense on the substrate

The snapshots of **Figure 6.5** show that condensation started occurring on the substrate and the CNT microstructure as the pressure increased, which caused the wall of the CNT microstructure to get thinner. This was due to the high evaporation rate at the low pressure even though condensation was occurring on the substrate. Next, the valve connecting the 2-propanol flask to the chamber was abruptly closed. As the pressure was gradually decreased, the CNTs were pulled together by the meniscus thus locally aggregating. Owing to the adhesion of the CNTs to the substrate, the CNTs were gradually less constraint from bottom to top. Gradient tangential densification caused the walls to incline thus forming a conical microwell.

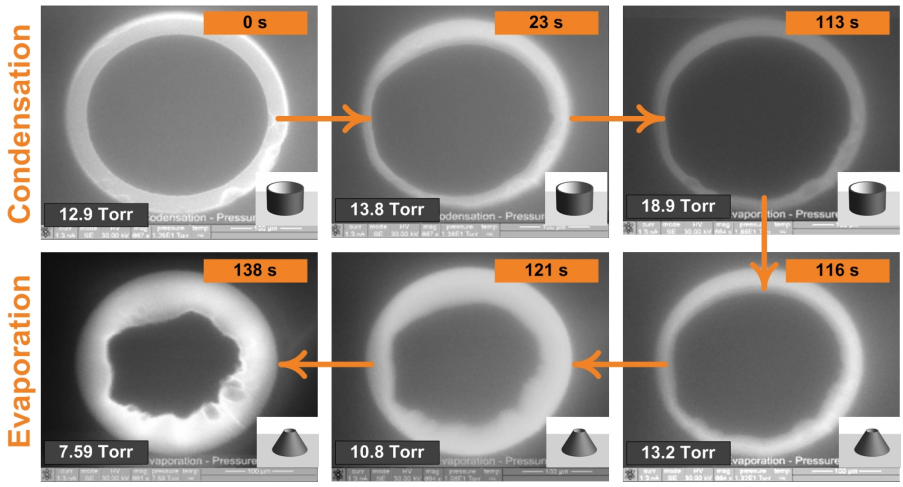

Figure 6.5 In situ capillary forming of a conical well imaged in Environmental SEM.

6.2.4. Kinetics of shape evolution

The kinetics of densification is measured using the camcorder-macrolens setup at ambient conditions, as described in Section 6.2.3. **Figure 6.6** shows the time evolution of the cross section area of a 200 µm square CNT microstructure having 200 µm height. The shape evolution is quantified by measuring the change in the perimeter and area of the top surface of the microstructure (Δ perimeter/initial perimeter; Δ area/initial area). The kinetics follows a nearly linear trend until the densification ratio reaches 10 (area strain 0.9) then the slope of the curve abruptly decays.

During the first stage, the kinetics of the shape evolution is limited by the rate of evaporation of the solvent and by the diffusion through the pores.[3, 4] At one limit, the rate

of volumetric change during the evaporation of a free droplet is ~$(t/t_f)^n$ where n is 1.3-1.5; and t and t_f are the real and final time respectively(**Figure 6.6b**).[5, 6] On the other hand, evaporation from porous material typically follows nearly linear trends due to the diffusion time scale of the material. Hence, as densificaton proceeds, the kinetics might have become limited by the diffusion rate and not only the evaporation rate because the internal pores become smaller. Further, the nearly linear trend observed from the videos indicates that the effect of the CNT material properties on the shape of the curve was only observed at the termination stage.

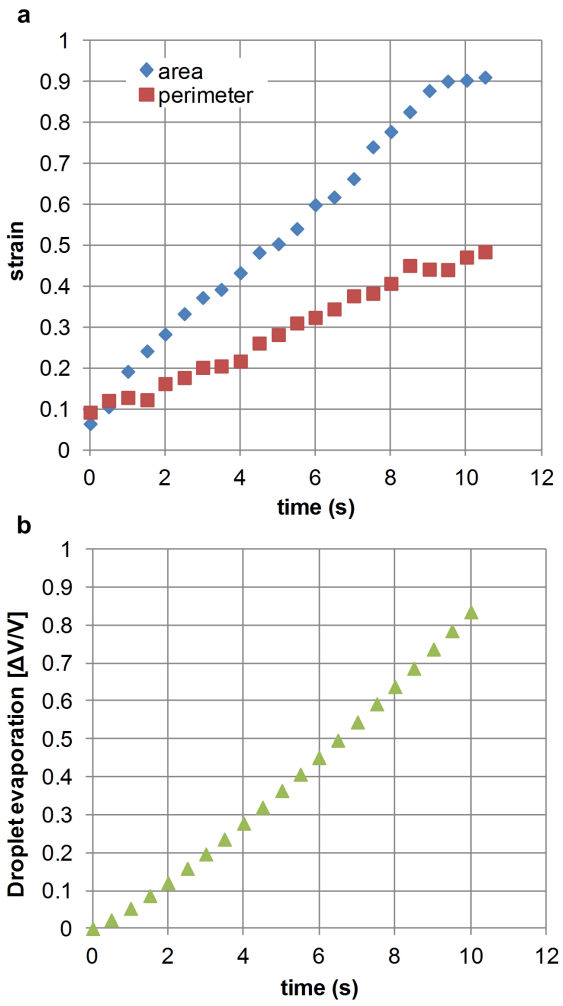

Figure 6.6 Kinetics of densification induced shape change. (a) Measurements from in situ experiments. (b) Theoretical droplet evaporation kinetics.

In the termination stage, the linear slope decreases abruptly until densification stops. The measurement capability does not resolve the dynamics of this stage. In the

following section, the mechanical properties of the CNT microstructure are discussed in more details. The non linear increase in stiffness modulus as the CNTs become more densely packed dictate the abrupt transition from the linear trend to termination at strains higher than 0.9. Hence, after ≈ 0.9 area strain, the droplets evaporate without causing any further densification to the structures.

6.2.5. Interface migration during evaporation

As the meniscus evaporates, the liquid interface migrates inwards and locally densifies the CNTs. This evaporation induced interface migration is responsible for the change in shape of symmetric shapes such as squares (**Figure 6.7**). During the process, balance is maintained between the surface tension and the lateral stiffness of the CNT network. This drives the **global migration** of the CNTs towards the centroid.[7] Due to the rounding of the meniscus as it evaporates the cross section shape changes as the meniscus recedes. For example, the corners of a square shape become more pointed as the meniscus recedes from these corners to minimize the surface energy. Hence, evaporation of the meniscus inside the microstructures is the dominant driver of shape change. For tall CNT structures the shape does not vary along the height; thus, evaporation occurs uniformly along the length and the substrate only affects the shape near the base. This also confirms that the evaporation is occurring from the side of the CNT microstructures (along their length) is responsible for the densification and the shape change.

6. 3 Forces and stresses in mechanocapillary forming

Capillary forming results in densification of the CNT microstructures. The decrease in cross section area confirms that the microstructures are subject to normal compressive forces as shown in **Figure 6.8**. And, high resolution SEM images indicate that the as-grown CNT microstructures have low density network-like morphology characterized by bends and entanglements along their length. This entangled structure is caused by the large spacing and the non uniform growth rates among neighbouring CNTs. The structure is schematically illustrated in **Figure 6.8** to highlight the the CNT organization that leads to highly anisotropic stiffness modulus.

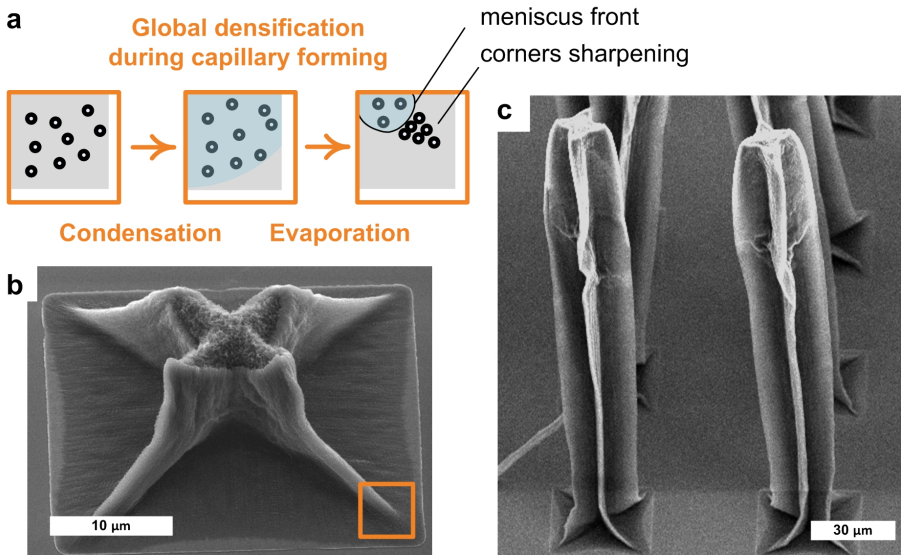

Figure 6.7 Global CNT migration during capillary forming. (a) Schematic of migration towards the centroid. Global CNT aggregation in (a) short and (b) high aspect ratio microstructures.

The stress stain curve of **Figure 6.9** is measured by compressing a delaminated CNT forest in the lateral direction. This curve guides our understanding of the reaction of CNT microstructures to lateral normal stresses (**Figure 6.9b**). The slope of the curve (≡ stiffness modulus) is linear at small strain (< 0.1); linear plateau (having a smaller slope) at strains $0.1 < \varepsilon < 0.5$; and exponential increasing at strains > 0.5. This stress-strain relationship is typical for the compression of low density foams and, as shown by the kinetics data, it strongly affects the capillary forming process.

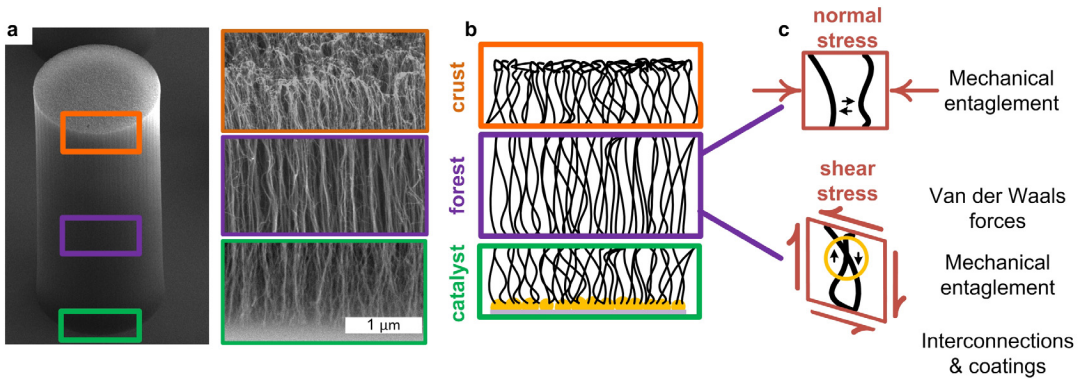

Figure 6.8 Structural characteristics of CNTs causing normal and shear moduli.(a) SEM image and (b) schematic of the various locations in the CNT microstructure. (c) Schematic of the structure causing the observed normal and shear stress.

Considering an ideal model of the CNT forest as spaced rods, we can estimate the compressive stress caused by the acetone surface tension on the sidewall of the CNT microstructure; this varies between 0.7 and 2.3 MPa, as indicated by the shaded area in **Figure 6.9a**. These values which correspond to engineering and true stress respectively can be estimated by multiplying the value of the surface tension of acetone (25 mN/m) by the linear density of CNTs per edge (~ 14 CNTs/µm for as-grown CNTs; ~ 46 CNTs/µm for capillary densified CNTs) by 2 (accounting for 2 contact lines per CNT) (**Figure 6.8d**)[4]. This shows that the densification stops when the compressive stress caused by the capillary forces on the CNTs is lower than the required stress to induce any further strain. This simple calculation accurately estimates the observed densification ratio (**Figure 6.9b**).

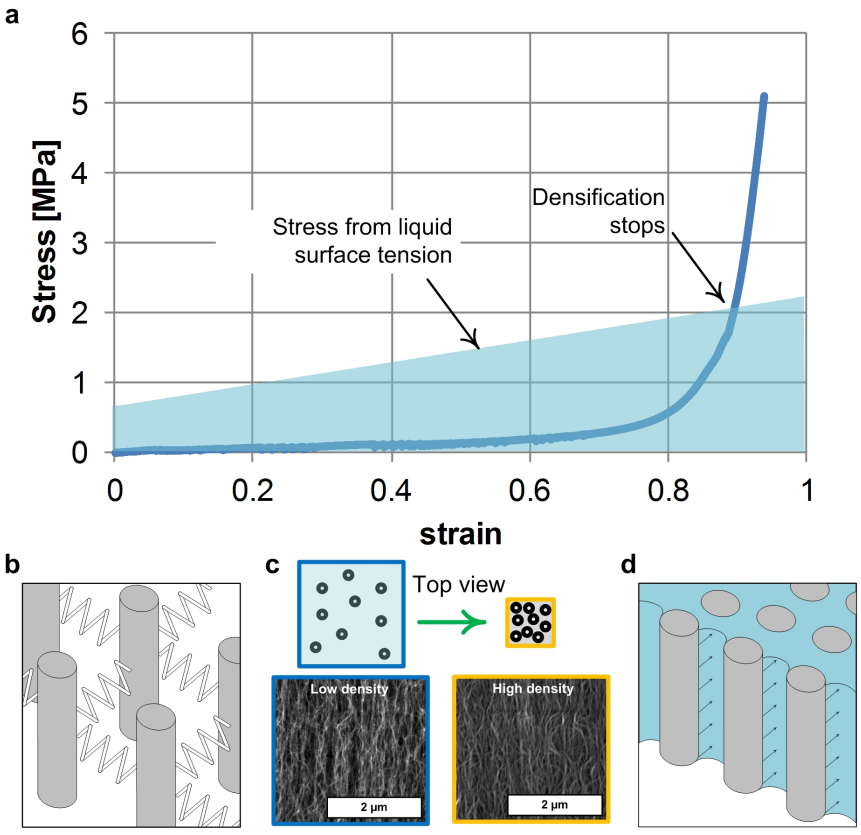

Figure 6.9 Competition of CNT mechanics and liquid surface tension. (a) Measurement of lateral stress strain of CNT forests. (b) Schematic of CNT microstructure mechanical model. (c) Schematic and SEM of local aggregation. (d) Schematic of surface forces on the CNT microstructure.

[4] In this calculation, the effect of the CNT adhesion to the substrate is not taken into consideration

In addition, the densification of CNTs results in development of shear stresses in the network. This effect is similar to shear flow in continuum mechanics. In the case of CNT microstructures, the shear stresses result from the van der Waals attraction and the mechanical entanglements among the CNTs. The shear stresses contribute to the bending asymmetric CNT microstructures as discussed in the Section 6.3.3. In fact the competition between the relative values of normal and shear moduli leads to the final geometry of capillary formed microstructures.

6.3.1. Local aggregation of CNTs (with Michael De Volder)

While small CNT microstructures do not exhibit internal voids, we observed that larger structures aggregate into the cellular morphology with large voids due to capillary forces.[8] We used this observation, along with elastocapillary theory to develop design guidelines to create uniform and robust solid materials. Considering CNTs to be cylindrical beams, the distance between the substrate and the point where two CNTs are pulled into contact during capillary forming is given by Eq. (6.2).[9]

$$L_I = C_1 \cdot \sqrt{d \cdot \sqrt{\frac{E \cdot \pi \cdot R^3}{4 \cdot \gamma}}} \ . \tag{6.2}$$

Here, d is the initial spacing of the CNTs in the forest, E is the Young's modulus of a CNT, R is the CNT radius, γ is the surface tension, and C_1 (= 1.4) is a constant. To prevent void formation, a structure comprising N CNTs must have length exceeding L_S, according to Eq. (6.3).

$$L_S = C_2 \cdot L_I \cdot \sqrt{\beta} \cdot N^{3/8} \tag{6.3}$$

Here, β (= 0.7) accounts for the arrangement of CNTs, and C_2 (= 0.8) is a numerical constant. If the CNT forest is initially shorter than L_S, the capillary formed structure has randomly distributed voids. This important boundary is validated experimentally by measurements of cylindrical CNT forest microstructures, shown in **Figure 6.10**, which indicate good agreement with the elastocapillary densification model.

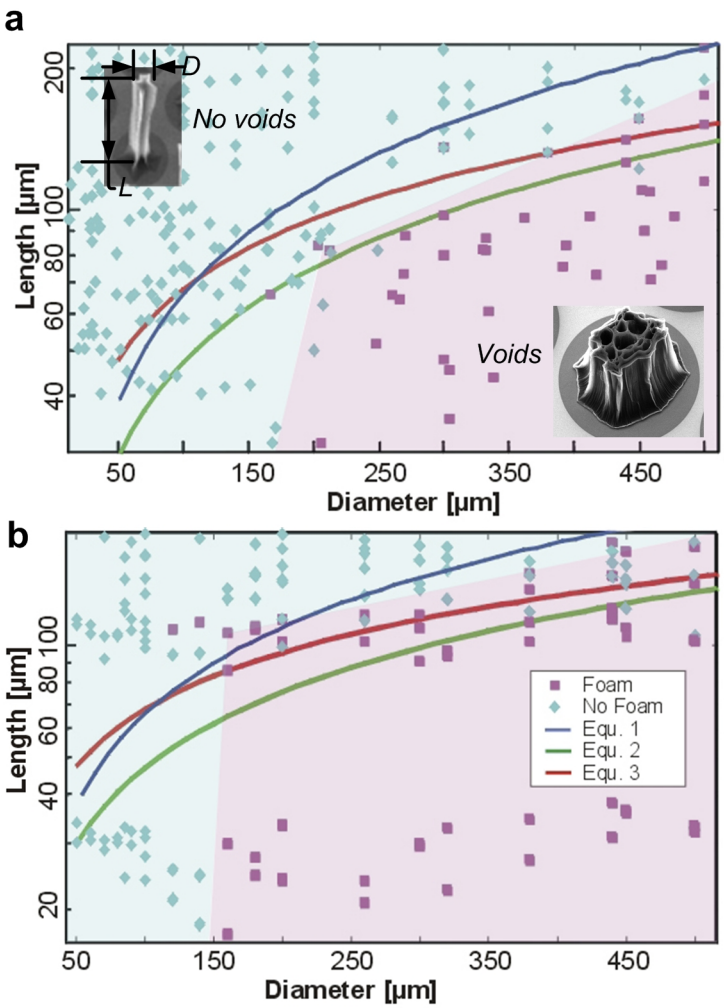

Figure 6.10 Comparison of elastocapillary theory with experiments. (a) as-grown CNTs. (b) Plasma etched CNTs.

6.3.2. Capillary induced bending (with Zhouzhou Zhao and Professor Wei Lu)

In addition to densification and cross-section change, asymmetric microstructures bend during capillary forming. Working closely with Zhouzhou Zhao and Professor Wei Lu we identified that the bending of asymmetric shapes is due to a combination of effects:[7]

- asymmetric external forces from non-uniform capillary rise
- asymmetric normal stresses in the material due to global migration of the CNTs towards the centroid
- internal shear stresses also due to the global migration of the CNTs

The contribution from the external capillary forces is small for larger features. My observations indicate that CNT micropillars features having width > 20 µm are not strongly affected by these forces. As a result, the normal and shear stresses have larger contribution to the bending mechanism.

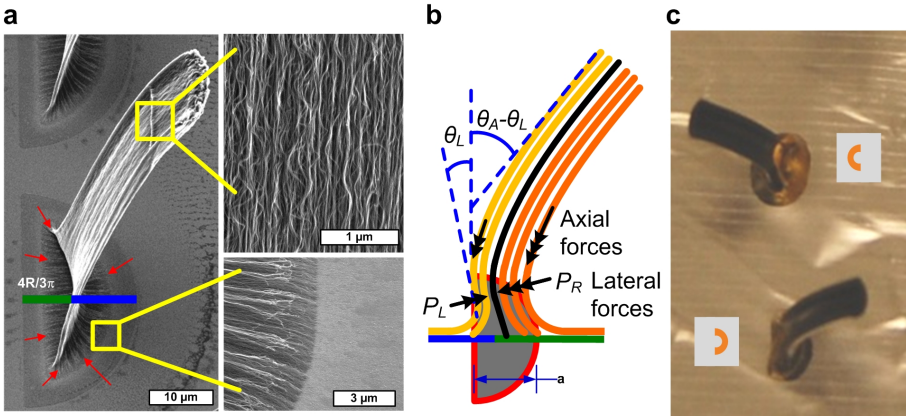

Figure 6.11 Bending of asymmetric CNT microstructures. (a) SEM image of bending structures showing global migration of the CNTs towards the centroid. (b) Schematic of the axial and lateral forces created inside the CNT microstructures. (c) Optical images of shrink tube models bent due to asymmetric migration towards the centroid.

The origin and distribution of forces is understood by examining capillary forming of semicylindrical CNT forests. As the liquid evaporates, surface tension causes the CNTs to aggregate locally according to the elastocapillary mechanism, and the forest globally contracts toward the centroid of its cross-sectional shape. Thus, for a semicircle, the contraction is toward the point at a distance 4R/3π from the straight edge of the semicircle (**Figure 6.11**), which is seen in an SEM image of the base of the structure. As this contraction occurs, the CNTs near the substrate are pulled inward toward the centroid, and this in turn pulls down on the upper portions of the forest. This creates shear stresses inside the CNT material.

The capillary pressure during densification introduces lateral forces on the structure, which are proportional to the number of CNTs on either side of the centroid as discussed in Section 6.3(**Figure 6.11**). A net bending moment results and causes the structure to deflect (θ_L) toward the straight edge of the semicircle. The lateral forces hence create normal stresses inside the structures similar to the densification of symmetric shapes.

Additionally, because of mechanical coupling between the base and the upper portion of the forest, the lateral motion of the CNTs creates a distribution of axial pulling forces, which acts on the CNTs above the substrate. The densification thus develops shear stresses inside the CNT microstructure. The axial forces create another bending moment at the base, which causes the structure to deflect (θ_A) toward the curved edge of the cross-section. The net deflection angle is calculated by modeling the structure as a cantilever beam, and adding the contributions due to the lateral and axial forces, $\theta = -\theta_L + k\theta_A$. The relaxation factor k ($0 < k < 1$) accounts for slip among the CNTs during capillary forming, which partially relaxes the bending moment and reduces the lateral deflection.

The balance between lateral and axial forces depends on the shear modulus of the CNT microstructure. As previously discussed, the amount of slip among the CNTs is dependent on the structural characteristics of the CNTs. Slip can be controlled by etching the top surface of the CNT forests before capillary forming or coating the CNTs with polymers or ceramics as discussed in Section 6.4.

To confirm the effect of shear stresses on bending of asymmetric shapes, I built mm scale models from heat shrink tubing. **Figure 6.11c** shows mm scale annular beams made by cutting heat shrink tubing in half using scissors. The tubes were vertically bonded to a metal foil surface using 5-minute epoxy. The models were placed in the oven for 5 minutes at 100°C. The images show that the heat shrink tubes bend towards the curved sides. Because heat shrink tubes are made out of an isotropic continuum solid, their ratio of shear modulus to elastic modulus is higher than that of VA-CNT microstructures. This result indicates that as the CNTs tend to bend towards the curved side as the shear modulus of the CNT microstructure is increased. Observations indicate that this occurs when as-grown CNTs have high density.

6.3.3. Capillary folding of thin microstructures

As mentioned earlier, thin CNT microstructures are more greatly influenced by external capillary forces around their perimeter. When their dimensions are beneath a stability limit, they can't withstand the downwards forces from the meniscus during capillary rise.

Thin structures hence become unstable and fold onto the substrate.[10] As a result, the direction of collapse can be engineered by designing asymmetric shapes with features leading to deterministically predict the direction of folding. The self-directed folding of patterned VA-CNT walls into HA-CNT patches shown in Chapter 5 is caused by a mechanical instability induced by capillary forces. The mechanism is understood by considering the collective deformations and motions of the CNTs, due to both internal and external capillary forces on the CNT forest. As the solvent is condensed on the sample the high affinity of acetone to CNTs causes it to infiltrate the VA-CNT forest and to form a meniscus around its boundary as shown in **Figure 6.12**.

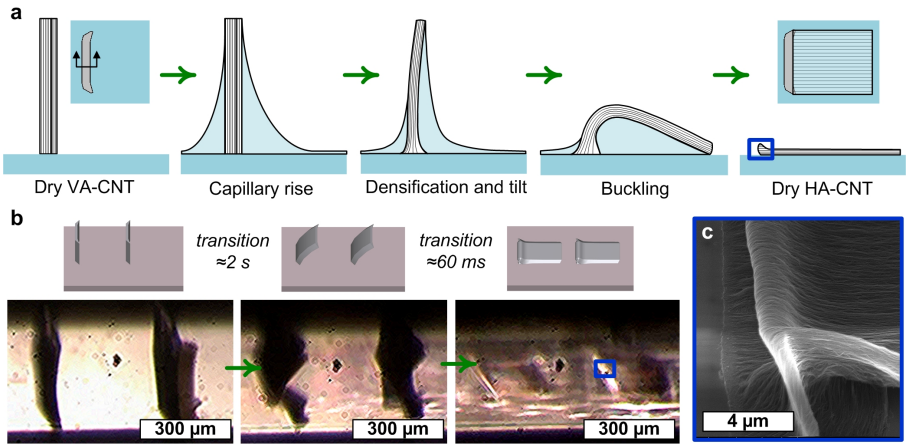

Figure 6.12 Mechanism of capillary folding. (a) Schematic showing the asymmetric capillary rise and buckling. (b) Optical snapshots of bending and buckling and their time scale. Insets are solid models of the structures in the images.

Thin CNT walls serve as model geometry to understand the effect of external forces during capillary folding. The local in-plane curvature of the forest boundary (perimeter) determines the local curvature and height of the meniscus, resulting in a distribution of forces with varying heights and directions of action around the boundary of the wall. For the wall with arrow, the meniscus rises higher at the concave wedge (right side) than the convex side (left).[1] A solution to the Laplace equation for the meniscus height on both sides of the tilted wall indicates that the height of the meniscus changes as the forest tilts according to the equations,

$$h_{in} = \sqrt{2}\kappa^{-1}(1-\sin(\theta_c + \alpha - \pi/2))^{1/2} \tag{6.4}$$

$$h_{out} = \sqrt{2}\kappa^{-1}(1-\sin(\theta_c - \alpha + \pi/2))^{1/2}. \tag{6.5}$$

$$\kappa^{-1} = \sqrt{\gamma/\rho g} \tag{6.6}$$

Here, h_{in} and h_{out} are the meniscus heights as shown in **Figure 6.3**, θ_c is the contact angle between the CNT wall and the liquid, α is the angle between the wall and the horizontal plane, κ^{-1} is the capillary length, γ is the liquid surface tension, ρ is the liquid density, and g is acceleration of gravity. Based on these equations, the meniscus tends to be higher on the right side of the wall (the side facing the direction of tilt). Moreover, the equations indicate that the initial tilt of the wall, caused by capillary rise and some elastocapillary densification (during condensation), creates an additional bending moment in the direction of the tilt. This moment increases with the magnitude of tilt, thus acting as a destabilizing moment which is resisted by the bending stiffness of the CNT wall. Results are independent of the orientation of the sample with respect to gravity.

We observe that relatively short walls densify and tilt, but do not fold to the substrate. Therefore, these structures reach a static equilibrium under the influence of capillary forces. Taller walls densify, tilt, and then fold to the substrate. In our experiments where acetone was condensed from a heated vapour stream under otherwise ambient conditions, tilting happened over a duration of 2 seconds, and folding occurred abruptly within one frame of video (60 milliseconds). Snapshots of the video are shown in **Figure 6.12**.

A model to predict folding considers the external (downward) force exerted on the CNT wall by the liquid, which causes the wall to buckle. We specify that the CNTs within the thin wall behave collectively as an elastic beam, with a force distributed around the perimeter of the wall. Further, due to the small contact angle between the liquid and the CNTs, and the small tilt angle, we approximate that this force acts along the axis of the CNTs. Consequently, CNT walls that are taller than a critical height fold to the substrate forming HA-CNT patches, and walls shorter than this height remain vertical and tilted after liquid evaporation. This critical height is known as the capillary buckling length (l_B), and was previously defined as the minimum height of an elastic column that buckles rather than pierces a liquid surface when the column is being pushed upward into the liquid-air interface. Therefore, the capillary buckling length is derived by equating the force due to the liquid surface tension on the column to the critical buckling load, such that

$$l_B = \sqrt{\left(\frac{E}{\gamma}\right)\frac{I}{w}}\,. \tag{6.7}$$

Here, E is the elastic modulus of the densified CNT wall, γ is the solvent surface tension, t is the thickness of the wall (parallel to the folding direction), w is the width of the wall (perpendicular to t), and I is the second moment of area of the cross section ($I = wt^3/12$). Thus, for rectangular walls the capillary buckling length is proportional to $t^{3/2}$ and is independent of w.

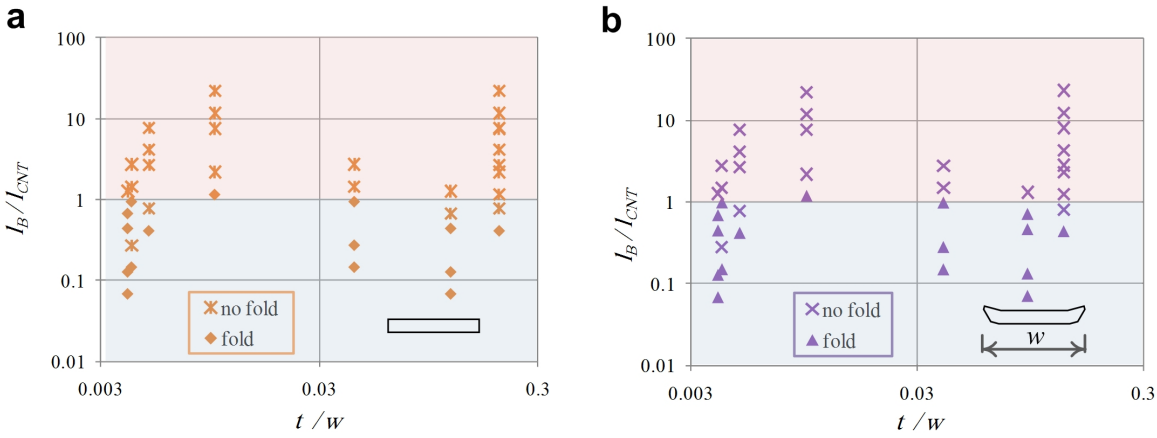

Figure 6.13 Plots comparing the theory and experiments of elastocapillay buckling. Red and blue shaded areas are the no fold and fold regions according to the model. (a) For rectangular microstructures. (b) For microstructures with arrows.

Examination of a folded CNT patch shows that the wall bent near its base with a small radius curvature (**Figure 6.12**), verifying that buckling occurred. Based on this model, we engineer capillary folding of VA-CNTs to HA-CNTs by specifying the linewidth of the catalyst pattern, and by controlling the wall height h, which is determined by the CNT growth time (50-100 μm/minute). Accordingly, we show in **Figure 6.13** that the elastocapillary buckling length accurately predicts the folding behaviour of CNT walls over two orders of magnitude of the scaling parameter l_B/h. Here, walls with $l_B/h > 1$ fold to the substrate, whereas walls with $l_B/h < 1$ remain vertical. The direction of the arrows patterned at the end of each wall determines the folding direction with 100% experimental certainty, whereas walls without arrows obey the same stability criterion but fold in randomly in either lateral direction. Arrays of CNT patches fabricated over the tested set of dimensions comprise individual patches with thickness from 300 nm to 2

μm, and lateral areas from several μm^2 to mm^2. Thus, by simply choosing the wall dimensions to be in the folding regime, HA-CNT patches can be fabricated over a wide range of length scales. The high packing density and lateral alignment of the CNTs within the folded patches are attractive attributes due to the anisotropic electrical and electromagnetic properties of CNTs.

As the size of the arrows is increased, the centroid of the cross-section is shifted farther from the centreline of the wall. This leads to larger bending angles during densification. However, the steeper arrows also increase the lateral stiffness of the structures, thus making the structures more resistant to buckling as shown in **Figure 6.13b**. Thus, due to these competing effects, the accuracy of the present model based solely on Euler beam buckling theory is limited, and a more advanced model should be implemented for folding of thin-walled CNT structures with other cross-sectional shapes.

As discussed in the beginning of this chapter higher order transformations can be achieved by combining several building blocks. For example, by combining thin features (folding) and asymmetric features (bending) we observed twisting of CNT microstructures during capillary forming. In particular, this occurs when circular array of catalyst semicircles are integrated in a thin walled circle as discussed in Chapter 5.2.3. The mechanism of the twisting hasn't been studied in details, but coordinated twisting of pillars due to capillary forces is observed in many nanoscale systems. In Figure 5.8 the semicircular catalyst patterns are oriented to achieve coordinated bending following the same rotation direction. Additionally, the thin walled cylinder connecting them folds inwards thus leading to constraining their deformation to helical twisting around the shape's centroid.

6. 4 Effect of material modification on capillary forming

Capillary forming of VA-CNT microstructures can be tuned by small changes in the structural characteristics of the CNT microstructures. For example, the competition between the normal and shear modulus determines the bending direction and angle of asymmetric shapes. By tuning the CNT material properties, the transformation geometry and the final density during capillary forming can be further controlled.

For example, **Figure 6.14** shows the effect of plasma etching on the capillary forming of cylindrical microstructures. The SEM images indicate that plasma etching removes the crust which allows more slip among the CNTs. This leads to the formation of rings having no wrinkles by capillary folding.

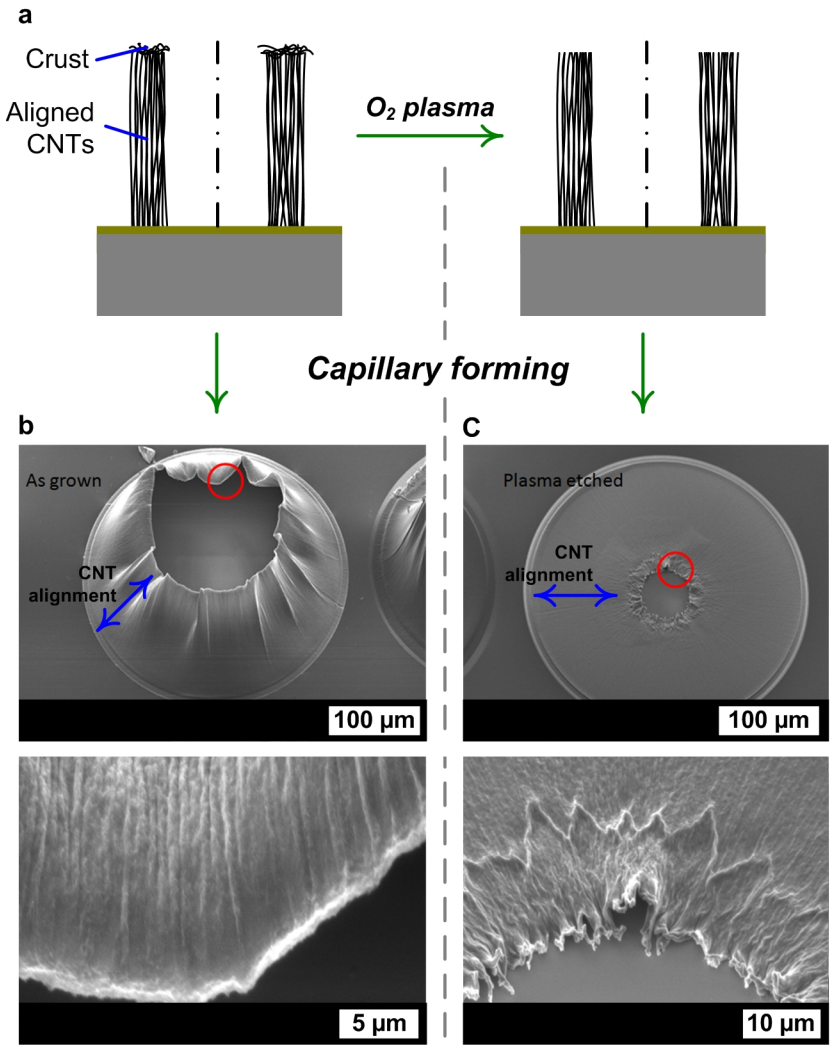

Figure 6.14 Tuning capillary forming by plasma etching. (a) Schematic and (b) SEM images of non plasma etched structures. (c) SEM images of plasma etched structures having no wrinkles.

Figure 6.15 shows combined structural changes effects. Structural control of the CNT forest is achieved by changing the growth recipe to make forests with larger diameter. This is achieved by flowing He during annealing (with no hydrogen) thus allowing the formation of larger metal particles as discussed in Chapter 3. The CNTs with larger average diameter but lower density show larger densification factor due to the

decrease in stiffness associated with the density decrease. On the other hand, the effect of plasma etching is the formation of more uniform microstructures with less wrinkling by allowing more slip and hence more effective re-organization of the CNTs in the forest during solvent evaporation.

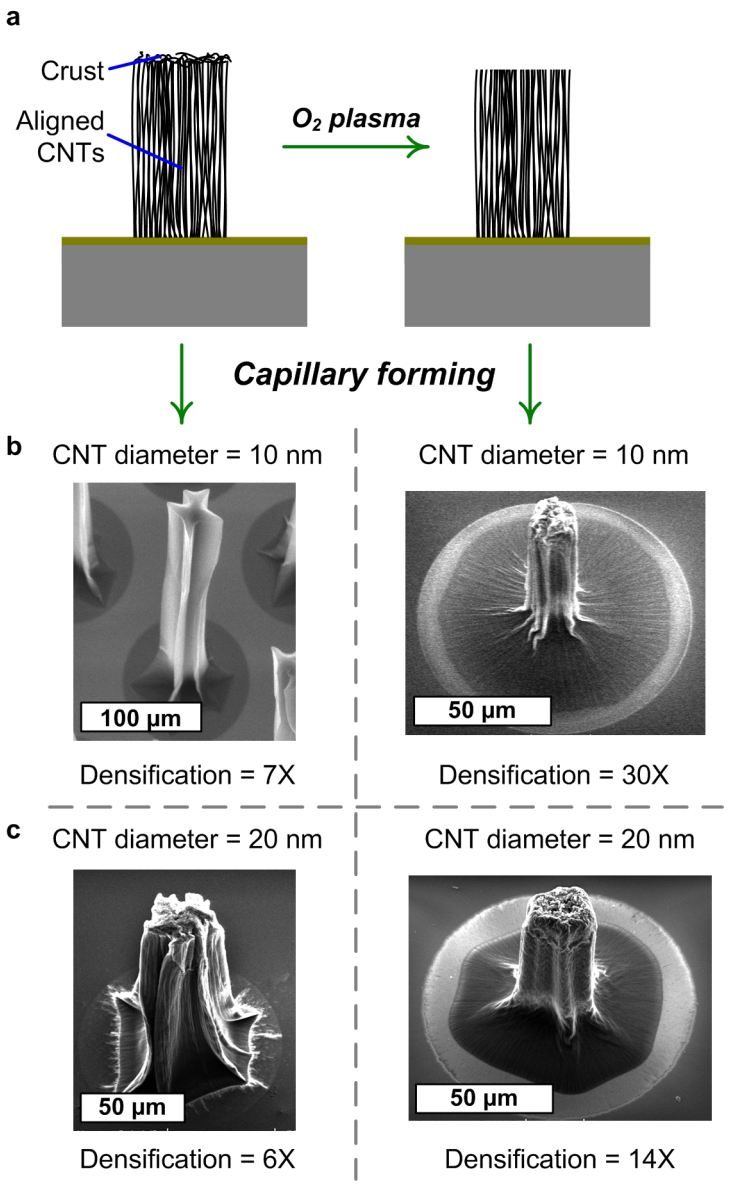

Figure 6.15 Tuning capillary forming by changing the diameter of the CNTs and/or plasma etching. (a) Schematic. (b) Capillary forming of (left) as-grown and (right) plasma etched CNTs with 10 nm diameter. (c) Capillary forming of (left) as-grown and (right) plasma etched CNTs with 20 nm diameter.

6. 5 Bibliography

1. Gennes, P.-G. d.; Brochard-Wyart, F.; Quere, D., *Capillarity and wetting phenomena: drops, bubbles, pearls, waves*. Springer: New York, 2004; p xv, 291 p.

2. De Volder, M.; Tawfick, S. H.; Park, S. J.; Copic, D.; Zhao, Z. Z.; Lu, W.; Hart, A. J., Diverse 3D Microarchitectures Made by Capillary Forming of Carbon Nanotubes. *Advanced Materials* **2010,** *22* (39), 4384-4389.

3. Tanaka, T.; Fillmore, D. J., Kinetics of swelling of gels. *The Journal of Chemical Physics* **1979,** *70* (3), 1214-1218.

4. González-Méijome, J. M.; López-Alemany, A.; Almeida, J. B.; Parafita, M. A., Dynamic in vitro dehydration patterns of unworn and worn silicone hydrogel contact lenses. *Journal of Biomedical Materials Research Part B: Applied Biomaterials* **2009,** *90B* (1), 250-258.

5. Sokuler, M.; Auernhammer, G. K.; Liu, C. J.; Bonaccurso, E.; Butt, H.-J., Dynamics of condensation and evaporation: Effect of inter-drop spacing. *EPL (Europhysics Letters)* **2010,** *89* (3), 36004.

6. Deegan, R. D.; Bakajin, O.; Dupont, T. F.; Huber, G.; Nagel, S. R.; Witten, T. A., Capillary flow as the cause of ring stains from dried liquid drops. *Nature* **1997,** *389* (6653), 827-829.

7. Zhao, Z.; Tawfick, S. H.; Park, S. J.; De Volder, M.; Hart, A. J.; Lu, W., Bending of nanoscale filament assemblies by elastocapillary densification. *Phys. Rev. E* **2010,** *82* (4), 041605.

8. Volder, M. D.; Park, S. J.; Vidaud, D.; Tawfick, S.; Vidaud, D.; Hart, A. J., Fabrication and electrical integration of robust carbon nanotube micropillars by self-directed elastocapillary densification. *Journal of Micromechanics and Microengineering* **2011,** *21* (4), 045033.

9. Py, C.; Bastien, R.; Bico, J.; Roman, B.; Boudaoud, A., 3D aggregation of wet fibers. *EPL (Europhysics Letters)* **2007,** *77* (4), 44005.

10. Tawfick, S.; De Volder, M.; Hart, A. J., Structurally Programmed Capillary Folding of Carbon Nanotube Assemblies. *Langmuir* **2011,** *27* (10), 6389-6394.

Chapter 7
Integration and properties of mechanocapillary formed CNTs

The mechanical, chemical and electrical properties of capillary formed CNTs are measured and compared to the as-grown microstructures, thereby demonstrating significant advantages of the mechanocapillary forming method. The chapter presents results from compression tests performed on individual VA-CNT cylindrical microstructures (≈90 μm diameter and ≈100 μm height). Capillary formed pillars have a stiffness modulus of 5 GPa, which represents ≈100-fold enhancement in modulus over as-grown CNT microstructure (54 MPa). Infiltrating the pillars with SU-8 and PMMA by spin coating increases the stiffness to 18 GPa and 25 GPa respectively. Further, coating of as-grown VA-CNT with parylene by CVD can effectively tune the stiffness of low-density VA-CNT microstructures from 60 MPa to 80 MPa using thin conformal layers ranging from 8 to 25 nm. A 400-fold increase in reactivity towards a florescent dye is observed for parylene coated VA-CNT compared to pristine CNTs. This demonstrates that the coating facilitates the chemical functionalization of VA-CNTs. A model is formulated to describe the changes in stiffness modulus due to conformal coatings and it suggests that the mechanical properties of the microstructures are governed by the interconnections among the aligned CNT network and thus are strongly affected by thin coating layers.

Integration with standard microfabrication processes is demonstrated by performing lithography and lift-off of Au electrodes on horizontal and inclined CNT microstructures. Resistivity measurements on as-grown and capillary formed VA-CNT show enhancement trends similar to those observed for the mechanical measurements. For example,

individual VA-CNT cylinders (40 μm diameter and 300 μm height) have 9 mΩ-cm resistivity after capillary densification which is a 2300-fold reduction compared to as-grown CNTs. This result can be attributed to the change structural characteristics of densified CNT microstructures and to the reduced contact resistance. The resistivity of flexible HA-CNT interconnects made by rolling and printing is 2 mΩ-cm due to the combination of mechanical compression and capillary densification. Radially oriented horizontal CNT rings made by capillary folding demonstrate 16:1 anisotropy in electrical resistivity.

Finally, the fabrication and integration of mechanically and electrically responsive microstructures is presented. Active CNT-hydrogel composite structures are prototyped and tested by combining isotropic moisture-induced swelling of the hydrogel with the anisotropic stiffness of CNTs to induce directed shape changing which can also be electrically transduced.

7. 1 Mechanical properties of CNT-polymer composite microstructures

7.1.1. Dense composites by capillary forming and polymer infiltration

VA-CNT microstructures having ≈90 μm diameter and ≈100 μm height are grown by CVD as described in Chapter 3. The mechanical properties of as-grown, capillary densified, and polymer infiltrated samples are compared.[1] The samples are prepared according to the standard processes of CNT growth and capillary forming described in chapters 3 and 5 respectively. After this, composite pillars are fabricated by spin coating and curing. The CF-CNT structures are spin-coated with SU8-2002 (Microchem) at 3000 rpm for 60 seconds. The SU-8 is pre-baked on a hot plate for 2 minutes at 65 °C, cured by UV exposure using a Dymax 2000 EC Flood Lamp (75 mW/cm2, 20 s), and post-baked for 4 minutes at 95 °C. Alternatively, the CF-CNT are spin-coated with PMMA-950K-A6 at 3000 rpm and baked for 90 s at 180°C on a hot plate. Capillary forces lead to the self-directed rise of liquid polymer and infiltration into the spacing among the CNT microstructures thus filling the nanoscale voids.

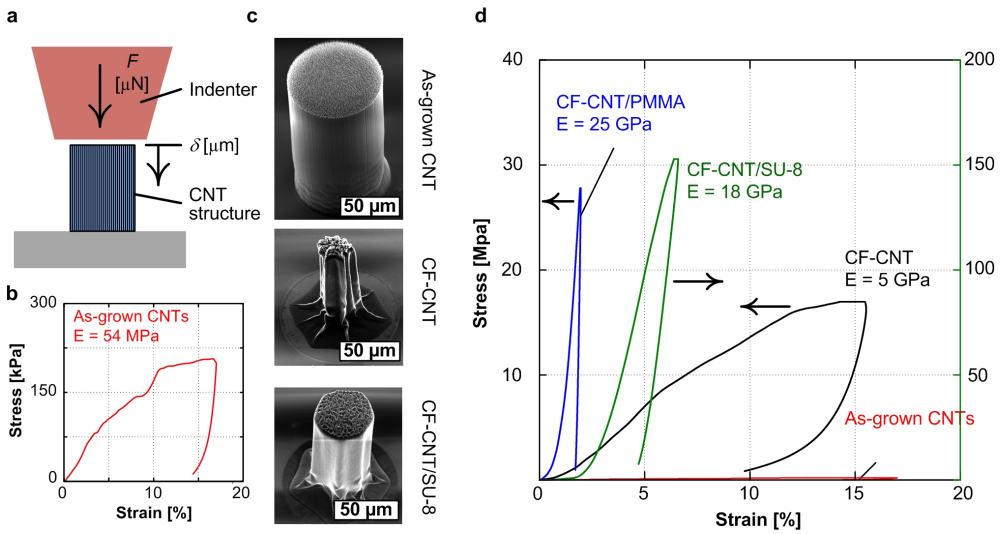

Figure 7.1 Mechanical testing of capillary formed CNT structures. (a) Compression schematic. (b) Stress-strain curve for as-grown CNTs. (c) Exemplary capillary formed CNT and composite microcylinders. (d) Stress-strain curves of capillary formed and polymer infiltrated CNTs.

The testing was done in a Nano Indenter XP (MTS) with flat diamond punch (200x200 μm cross section). This system is located in Professor Weidian Shen's lab at Eastern Michigan University. At the beginning of each test, the punch is aligned to the CNT composite pillar by an optical microscope and the vertical position of the top surface of the pillar is automatically detected by measuring the increase in stiffness as the tip approaches the surface of the pillar using a built-in algorithm. The load on the pillar is increased at a rate of 2 mN per minute. First, the maximum is strength is determined by increasing the load on the samples until they break. Second, the samples are loaded to <50% of the maximum strength. At the maximum load, the tip is held for 30 seconds to allow for creep relaxation. Finally, the load is decreased at a rate of 2 mN per minute. The elastic stiffness (k) of the pillar is determined from the slope of the unloading curve at the location of maximum compression of the pillar. The stiffness modulus of each pillar is then calculated as

$$E = \frac{\sigma}{\varepsilon} \tag{7.1}$$

Here, σ is the engineering stress (force/area) and ε is the strain (tip displacement/pillar height). Dimensions and mechanical properties of various CNT pillars are summarized in the table below.

Table 7.1 Dimensions and properties of various capillary formed CNT microstructures characterized by mechanical compression

Pillar material	**Densification factor**	**Diameter [µm]**	**Height [µm]**	**Stress [MPa]**	**Strain**	**Modulus [GPa]**
As-grown CNTs	1	90±5	120	0.21	17 %	0.05
Densified CNTs (D-CNTs)	14	25±5	74	17	16%	5
D-CNTs/SU-8	4	45±5	85	153	7%	18
D-CNTs/PMMA	11	27±2	74	28	2%	25

Capillary formed pillars have a stiffness modulus of 5 GPa, which represents ≈100-fold enhancement in modulus over as-grown CNT microstructure (54 MPa). Infiltrating the pillars with SU-8 and PMMA by spin coating increases the stiffness to 18 GPa and 25 GPa respectively. These values are 5- to 10-fold enhancements over pure SU-8 (E = 2-4 GPa[2]) and pure PMMA (E = 2-5 GPa[3]). To our knowledge, these are the highest values yet reported for CNT-polymer composite microstructures, and are notably higher than the value of E = 12 GPa obtained by immersion of as-grown CNT forests in SU-8.[4, 5] Therefore, this new two-step approach to densify the CNTs by capillary forming prior to polymer infiltration thus achieves a higher CNT packing density, avoids distortion of the as-grown CNT forests by polymer infiltration, and enables formation of unique 3D composite shapes over large areas.

Notably, while the reduction in cross-sectional area is 12, the modulus increases by a factor of more than 100. The great increase in the modulus can be attributed to the change in collective loading mechanism of individual tubes within the forest which is caused by the reduction in CNT-CNT spacing. In fact, if the CNTs were straight rods under compression, changing the spacing between the CNTs should lead to a measured change in modulus corresponding to the reduction in area. However, in these tests the CNTs are not straight columns under compression forces. Due to the waviness of the

CNTs, the microstructures behave like complex networks of interconnected CNTs supporting one another at periodic contact points. Thus individual CNTs within a forest are not feeling pure compression (unlike a rod under compression), instead they are mostly subject to bending and shearing loads. The CNT-CNT spacing changes the topography of the network thus modifying their collective stiffness. This mechanism is quantitatively studied and a model is set up to capture the changes in stiffness measured for coated VA-CNT (Chapter 7.2). The expected ability of the CNT microstructures to withstand large compressive strains without breaking at high temperatures (exceeding 600 C in air) makes them attractive elements for MEMS devices operating in harsh environments.

7.1.2. Porous composites by CVD coating

Figure 7.2 shows SEM images of as-grown CNT microstructures after deposition of the Reactive Coating as described in Chapter 3.[6] The growth and deposition processes are described in Chapter 3. Depending on the deposition time, the polymer thickness varied between 0 and 100 nm, as determined by ellipsometry on Si coupons placed next to the CNT structures.

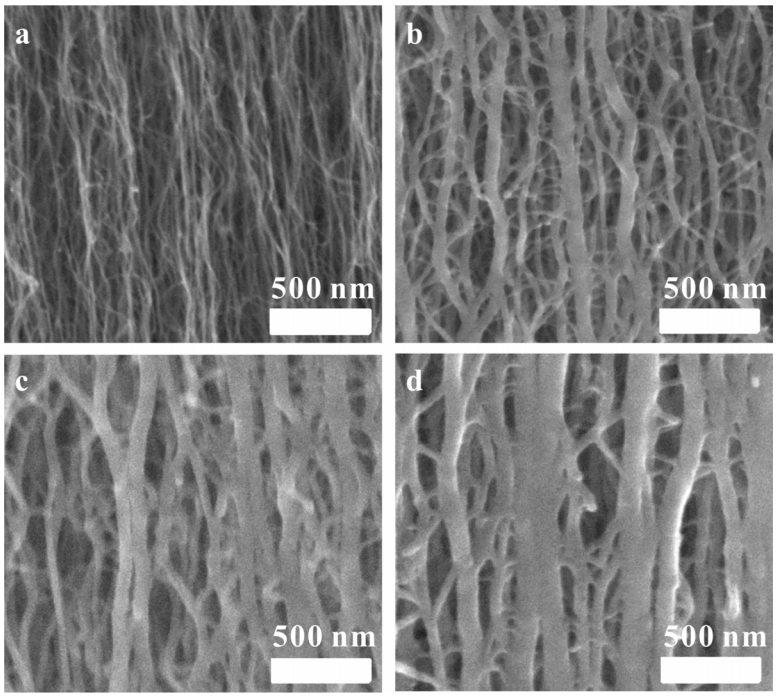

Figure 7.2 SEM image of CNT microstructures coated by Reactive Coating. (a) As-grown CNTs. (b) 10 minute coating. (c) 20 minute coating. (d) 30 minute coating.

Figure 7.2 compares the sidewall of an uncoated CNT forest (a), with composite structures (b-d) obtained after CVD polymerization for 10, 20 and 30 min, respectively. Based on the SEM images, the respective polymer thicknesses were estimated to be 10, 19, and 27 nm, which correspond to polymer contents of 93.1, 97.6, and 98.7 vol% in the final hybrid material. These images show that the polymer has good conformity on the individual CNTs and CNT bundles within the forest at the nanoscale. However, the interpenetration depth is not known.

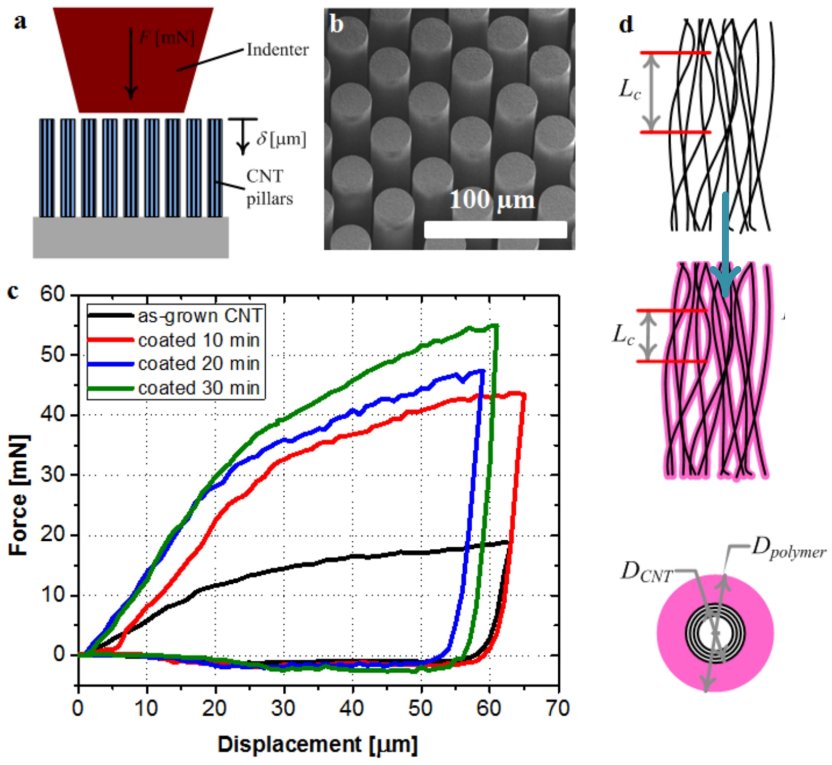

Figure 7.3 Compression testing of CNTs coated with Reactive Coating. (a) Test configuration. (b) SEM image of the tested CNT microstructures. (c) Stress-strain curves for the as-grown and coated CNTs described in Table 7.2. (d) Schematic of the conformal Reactive Coating of CNTs and the modification in the characteristic length L_c.

Mechanical testing of as-grown and polymer-coated CNT forest microstructures was performed using a custom-built micro-compression tester, with computer controlled displacement and force acquisition. The pillars were contacted using a stainless steel tip machined to a diameter of ≈300 μm as shown in **Figure 7.3**. The deposition of reactive coatings within CNT forests facilitates tuning of the mechanical properties of the complex microstructures. Specifically, the stiffness modulus of the structures, determined from compression testing, can be designed by selecting the thickness of the polymer layer. **Figure 7.3** presents the measurement configuration and results of micro-compression tests of arrays of bare CNT pillars, along with arrays coated for 10, 20, and 30 minutes. For each sample, the elastic modulus of the pillars (E_f) is calculated from the slope of the unloading curve, after loading to the sample to a strain of ≈35%.

To understand how the polymer coating increases the modulus of the structures, I built a mathematical model to capture the mechanics of VA-CNT microstructures. The

CNTs are modeled as hollow circular beams having flexural rigidity *EI*, where *I* is the moment of inertia of its cross-section. Then, after polymer coating, the CNTs form core-shell composite beams, having rigidity

$$(EI)_c = (EI)_{CNT} + (EI)_{polymer} \tag{7.2}$$

The model relates the elastic modulus of as-grown and coated forests to the known modulus and dimensions of individual CNTs with the different coatings. Such a model has not previously been developed for VA-CNTs because of the complex morphology and interactions in the network. For example, while the stiffness of CNT forests has been studied by means of cyclic compression tests; only the critical buckling stress could be theoretically predicted based on the known properties of individual CNTs.

Due to their high aspect ratio and their tortuosity within the forest, individual CNTs are mostly subject to bending, when the forest is compressed. Consequently, the flexural rigidity of the individual CNTs dominates the collective stiffness of the CNT forests. The flexural rigidity is equal to *EI,* where *E* is the elastic modulus of the CNT, and *I* is the second moment of area of the CNT cross-section. Thus, the film stiffness (k_f) can be related to the elastic modulus of the forest (E_f) and the flexural modulus of an individual polymer-coated CNT according to the equations below.

$$k_f = \frac{E_f A_{tip}}{h_f} = c(EI)_c \tag{7.3}$$

$$c = \frac{n\lambda}{mL_c^3} \tag{7.4}$$

I introduce a constant of proportionality (c) that accounts for the geometry, loading, and collective morphology of the individual CNTs. Within equation (2), λ is a constant and L_c is a characteristic length; both of these parameters depend on the geometry of the individual CNTs and loading conditions. For example, if the CNT forest could be modeled as a number of cantilever beams each subject to a transverse tip force,

then $\lambda = 3$, and L_c would be equal to the beam length. For curved beams, $\lambda = 2/\pi$, and L_c is the radius of curvature of the beam.

Using this expression, each CNT (extending vertically through the forest) is modeled as a number of identical compression springs loaded in series, regardless of their exact geometry. Consequently, the forest is a number of CNTs loaded in parallel. The constant *m* accounts for the periodicity of the characteristic length within the forest, which can be depicted as the number of identical springs that constitute each CNT. Thus, *m* is related to the waviness of the individual CNTs, because the amount of contact with other CNTs determines the characteristic "free" length of each spring section. Finally, *n* represents the number of load-bearing elements resisting the load in parallel and thus relates to the areal density of the CNT forest (CNTs/cm^2).

Using the measured values of the outer diameter of the polymer-coated CNTs, and the known value (E_p = 1 GPa) of the modulus of parylene, *c* is calculated for the three composites that were tested. These values, along with the value for uncoated CNTs, are shown in Table 7.2. In the case of the 10 minute coating, the increase in the elastic modulus of the forest (80%) cannot be related only to the increase in flexural rigidity (2%). According to the model, the *c* value increases to 1.09×10^7 μm^{-3}, and therefore the polymer connects neighboring CNTs and CNT bundles. Considering that all parameters are constant except for the polymer thickness, we predict that the characteristic CNT length decreases by ≈20% due to the increased coupling within the composite.

For the 20 minute deposition time, the composite rigidity significantly increases due to the increase in polymer diameter. However, the value of *c* remains almost unchanged compared to the 10 minute sample, indicating that the mechanism of film deformation and the characteristic length remain unchanged. For the 30 minute deposition time, the composite modulus of rigidity keeps increasing due to the diameter increase. Interestingly, the value of *c* decreased slightly but remains higher than that for the as-grown CNTs. This may be attributed to inaccuracy in average diameter

measurement after polymer coating, owing to the polydisperse collection of individual CNTs and bundles within the forest.

Further, the loading region stress strain curve of the nanotubes show two distinct slopes. The first slope is linear and extends to ≈12-18% where a transition to a smaller slope takes place. This transition can be attributed to a change in deformation mechanism between individual tube compression and collective buckling of the CNTs. In the latter case, the proximity of the individual CNTs induces self-organization of wavelike buckles, as has been observed previously.

Table 7.2 Dimensions and properties of various parylene coated CNT microstructures characterized by mechanical compression

	Measurements			**Model**	
Polymer CVD time [min]	**Polymer thickness on flat substrate [nm]**	**Diameter of polymer-coated CNT [nm]**	**E [MPa]**	**(EI)composite [mN/nm^2]**	**c [μm^{-3}]**
0	0	9	36	0.900	6.18×10^6
10	38	28	64.5	0.918	1.09×10^7
20	70	47	73.1	1.04	1.08×10^7
30	100	63	80.15	1.36	$9.09\ 10^6$

7. 2 Chemical functionality of coated CNT microstructures (with Xiaopei Deng and Professor Joerg Lahann)

To confirm that reactive coatings deposited within CNT structures still maintained their chemical reactivity towards binding partners, we used a model ligand, fluorescein-5-thiosemicarbazide, for coupling to the Reactive Coatings. These experiments were done by Xiaopei Deng in Professor Lahann's group. **Figure 7.4** details the outcome of this experiment. As anticipated, after immobilization of the fluorescence label, enhanced fluorescence was observed on the CNT structures. Note, that the high background fluorescence of the substrate present before and after reaction with the fluorescence label is due to the autofluorescence of the photoresist used during photolithography. To quantitatively compare the fluorescence intensity of the CNT structure area, the mean gray values of the CNT structures were measured using ImageJ. The normalized

fluorescence intensity (NFI) was calculated as the mean gray value of the CNT structures divided by the mean gray value of the flat surface (background) surrounding the structures. The fluorescence intensity of the CNT structures increases by approximately 400% after polymer coating, confirming that deposition of Reactive Coatings imparted chemical functionality to the CNTs. Based on this study, it is very plausible that chemically modified and mechanically reinforced CNT microstructures could play a pivotal role in future development of thin films for energy absorption, materials exhibiting chemical and/or optical transduction of mechanical stimuli, and/or as elements of next-generation biointerfaces.

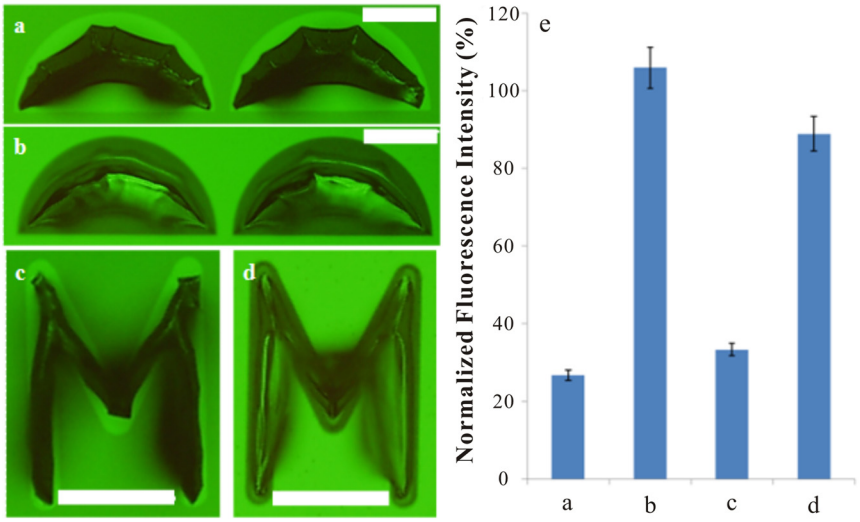

Figure 7.4 Demonstration of selective chemical functionality of CNT microstructures enabled by polymer coating: (a, c) CNT structures without polymer coating, with dye coating; (b, d) CNT structures with poly[4-trifluoroacetyl-p-xylylene-co-pxylylene] coating and dye coating, exhibiting significant fluorescence enhancement. Structures were densified by infiltration and evaporation of acetone before dye coating to prevent distortion due to capillary forces from the dye solution. The normalized fluorescence intensity (NFI), plotted in (e), is defined as the mean gray value of the CNT structures divided by the mean gray value of flat surface background. Scale bars represent 100 µm.

7. 3 Electrical conductivity of VA-CNT microstructures

In addition to being mechanically robust, the densified CNT micropillars can be electrically integrated in microsystems. This was demonstrated by growing CNT forests on patterned TiN electrodes, followed by densification and electrical characterization. The TiN electrodes were deposited by sputtering and patterned by photolithography before the catalyst patterning step. The catalyst layer consisting of 10nm Al_2O_3 and 1 nm of Fe was subsequently deposited by e-beam evaporation on top of the TiN electrodes through a second layer lithographic step followed by CVD growth as described in Chapter 3 (**Figure 7.5**). The structures are tested by placing a needle probe on the TiN electrode pad while the second probe is in contact with the CNT structure from the top.

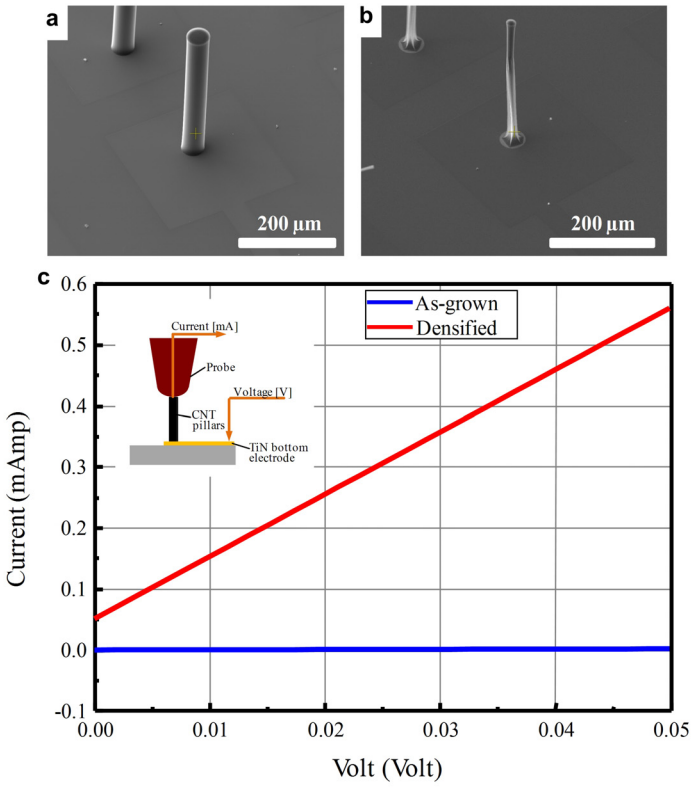

Figure 7.5 Electrical measurement of capillary formed CNTs. (a) SEM images of as-grown and (b) capillary formed CNT micropillars on TiN electrodes. (c) Comparison of two-point probe measurements of the CNT microstructure resistance (D = 40 µm, L = 300 µm), before and after capillary forming.[7]

Figure 7.5c compares two-point probe measurements of an individual cylindrical CNT micropillar (D = 40 µm, L = 300 µm), before and after densification. We find that the presence of the 10nm Al_2O_3 dielectric layer does not prevent the formation of Ohmic electric contact between the CNT structures and the bottom electrodes. The measured resistance of the individual structure shown in **Figure 7.5a** decreased from 373 Ω to 900 mΩ due to densification, which is a factor exceeding 414:1. This measured resistance includes a contribution from the contact resistance between the CNTs and the probes and the series resistance of the Al_2O_3 layer.

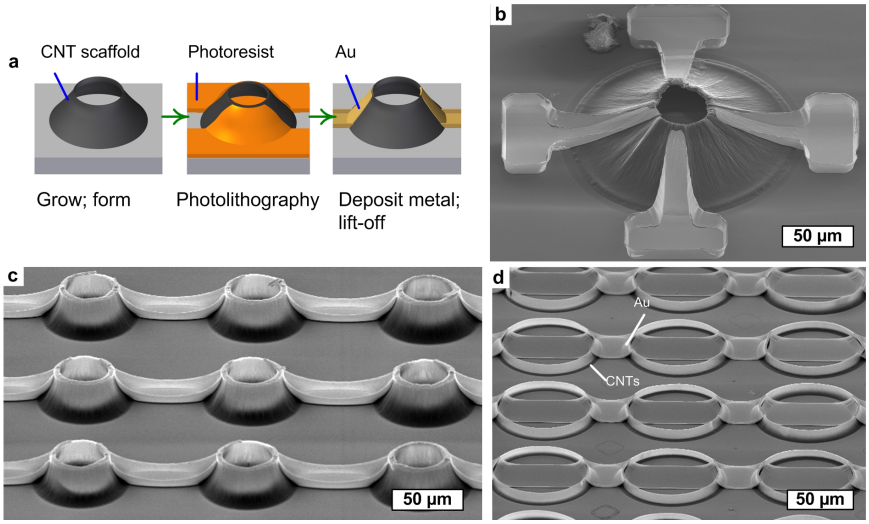

Figure 7.6 Integration of 3-D CNT with microfabrication. (a) Schematic of photolithography process for 3-D CNTs. (b-d) SEM images showing various conical well geometries electrically addressed with Au electrodes.[1]

As discussed for the mechanical stiffness, the enhancement in electrical properties cannot be correlated only to the reduction in cross-sectional area. The conductivity changes from 23 Ω-cm for as-grown pillar to 9.7 m Ω-cm to capillary formed pillar. The significant reduction in resistance is probably due to: (1) the decrease in contact resistance between the CNTs at the bottom of the structures and the TiN electrode pad, because the CNTs are pulled down onto the TiN electrode as they are densified, thus increasing the effective contact area; and (2) improved lateral conduction between CNTs due to densification, which establishes additional electron flow paths around critical faults in individual CNTs; and (3) better contact with the top probe which is enabled by the higher stiffness and robustness of the densified pillars. While the as-grown pillars are

very fragile and might have been poorly contacted during the measurement, we can still conclude that capillary forming is significantly advantageous for both the mechanical and electrical properties of CNT microstructures.

7. 4 Integration of VA-CNT with microfabrication processes

Integration of capillary formed CNT microstructures with several conventional microfabrication processes is illustrated by lift-off patterning of Au strips on the surfaces of slanted micro-wells (**Figure 7.6**). These structures were chosen for possible application as confined environments for electrical stimulation of cells. Subsequent plasma etching can remove the CNTs, thereby allowing use of the CNTs as scaffolds for release of non-planar freestanding film structures. Patterning of Au on radially oriented CNT films (≈400 nm thickness, **Figure 7.7**) produced by capillary folding enabled characterization of their electrical properties. The films have resistivity 45 mΩ-cm in the radial direction (R_r) and 709 mΩ -cm in the circumferential direction (R_θ), which is a ratio of 16:1. This unique radial anisotropy of electrical conductivity would be preserved due to the CNT alignment in the sloped, folded, and twisted structures; and this can be useful for making 3D interconnects and micro-probes that take advantage of the mechanical strength and flexibility of CNTs.

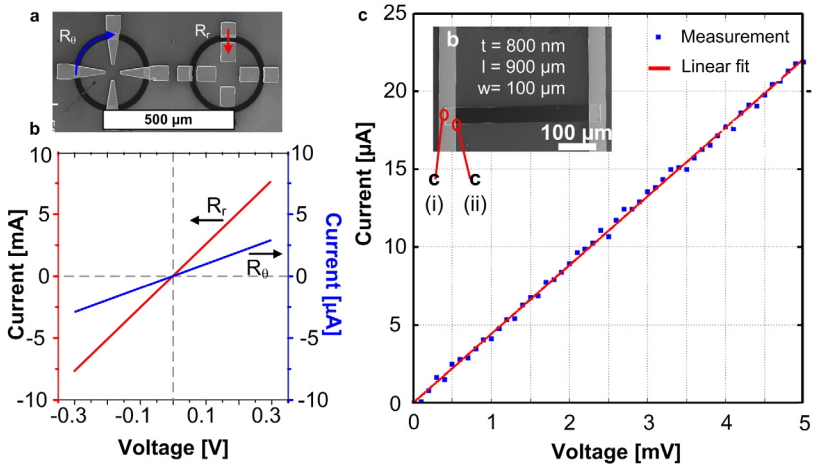

Figure 7.7 *I-V* measurement of radially oriented (RO-) CNTs and HA-CNTs. (a) SEM image showing RO-CNTs. Electrodes are patterned to measure the anisotropy by measuring the *I-V* curve in the radial and tangential directions. (b) *I-V* measurement of RO-CNTs demonstrating 16:1 anisotropy in conductivity. (c) *I-V* measurement of HA-CNTs. Inset showing mm long bundle of continuous CNTs.[8]

Lithography can also be performed on HA-CNTs fabricated by rolling to pattern Au electrodes for electrical addressability as shown in **Figure 7.7**.[8] The HA-CNT interconnects are flexible, can be transferred to plastic substrates as demonstrated in Chapter 4 and their measured resistivity is 2 mΩ -cm. The conductivity is better than CNTs made by capillary forming without rolling because the mechanical compaction due to rolling before the capillary densification is applied leads to a higher packing fraction as discussed in Chapter 4.

7. 5 Responsive CNT-hydrogel composites and transducers

A new class of microtransducers can be fabricated based on the swelling of hydrogels within microfabricated 3-D CNT frameworks.[9] Inspired by plant actuation, the anisotropic organization of CNTs within the framework imparts a directed shape transformation upon isotropic swelling of the hydrogel, which is initiated herein by water uptake.[10, 11] Therefore, this material design and its resulting hydrotropic behaviour emulate the natural response of plant cells. Due to the small scale of the nanocomposite structures, and their directional texture which promotes rapid uptake of liquids, actuation is rapid. Further, we demonstrate that the continuity and electrical conductivity of the CNTs within the structures enables integrated electrical transduction of shape changes within microfluidic channels.

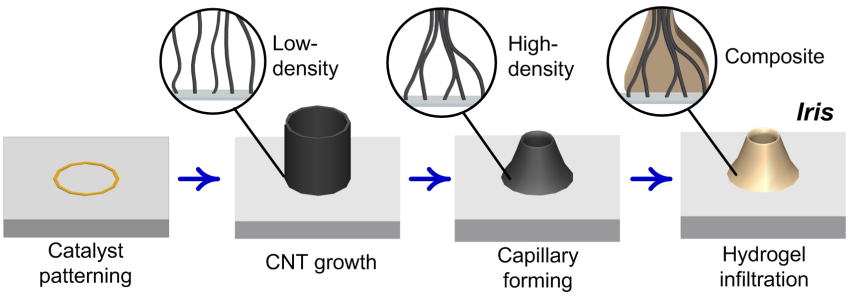

Figure 7.8 Process for fabrication of 3-D CNT-hydrogel composites.

CNT-hydrogel nanocomposite microstructures are fabricated as shown in **Figure 7.8**. First, VA-CNTs conical wells are fabricated by the standard process. After capillary forming, the CNT microstructures are infiltrated with a hydrogel by spin-coating. The substrate is first flooded with hydrogel and then spin-coated for 30s at typical speeds of

3000 rpm, followed by UV curing (5 min at 32 mW/cm² in a Karl Suss MA8 mask aligner in flood exposure mode). The hydrogel mixture comprises; 99 mol% monomer, 2-hydroxyethylmethacrylate (HEMA); 1 mol% cross-linker, ethyleneglycoldimethacrylate (EGDMA); and a photoinitiator.[12] By controlling of the spin-coating parameters, the hydrogel is retained exclusively within the CNT structures. The localized yet parallel nature of self-directed capillary action that occurs during densification and hydrogel infiltration results in highly uniform coating of the CNT microstructures as shown in **Figure 7.8**. The hydrogel is physisorbed to the CNT scaffold because no physical or chemical treatment was performed to promote covalent bonding to the CNTs. Nevertheless, because of the interconnected nature of the spaces within the CNT network, it is likely that the hydrogel is firmly held within the structures, and this interaction is sufficient for repeated reversible actuation.

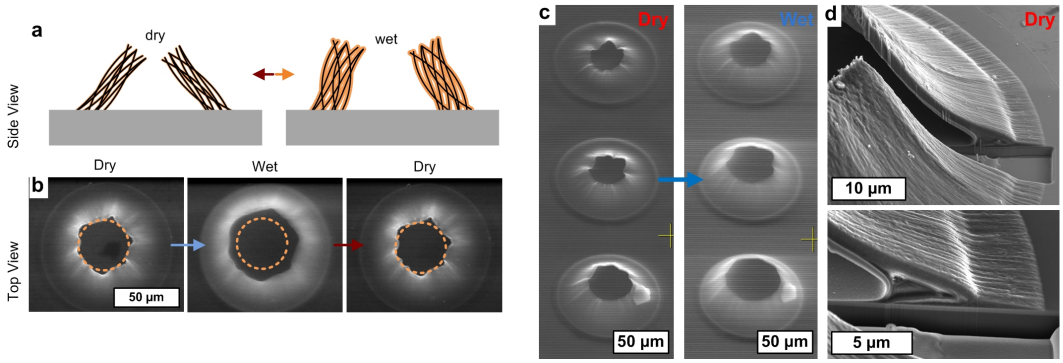

Figure 7.9 Self-directed actuation of 3-D CNT-hydrogel composites. (a) Schematic of the self-directed actuation mechanism. The isotropic swelling of hydrogel opens the iris of the conical well and changes the inclination angle. (b) In situ Environmental-SEM snapshots of CNT-hydrogel actuation due to changing the humudity in the E-SEM chamber. (c) E-SEM images of iris array under dry and wet conditions. (d) FIB section of a dry iris, showing thin nanocomposite sidewall and slight accumulation of residual gel on the interior of the wall.

In **Figure 7.9**, the dynamic swelling and contraction of a conical well is demonstrated by changing the relative humidity in the Environmental SEM chamber from 24% RH (1.4 Torr) to 80% RH (4.6 Torr) and back. Upon contraction, the well returned to its original shape, and recovered its initial texture including the small wrinkles formed during the fabrication process. No deterioration in the actuation was observed over 10 wetting and drying cycles, and the samples exhibited identical behaviour after storage in ambient conditions for 1 year.

To further understand the relationship between the geometry of the nanocomposites and their actuation behaviour, we fabricated arrays of iris structures with different opening angles (**Figure 7.9**). Specifically, we controlled D_{dry} of the iris by varying the slope of the sidewall while keeping the base diameter of the structure constant. The initial wall thickness was measured by cutting the structures using a focused ion beam (FIB) (e.g., ≈ 2 μm in **Figure 7.9**). The FIB sections of the CNT-hydrogel composites shown in **Figure 7.9** also suggest that a void free composite is formed with a slight accumulation of residual gel on the interior wall of the wells.

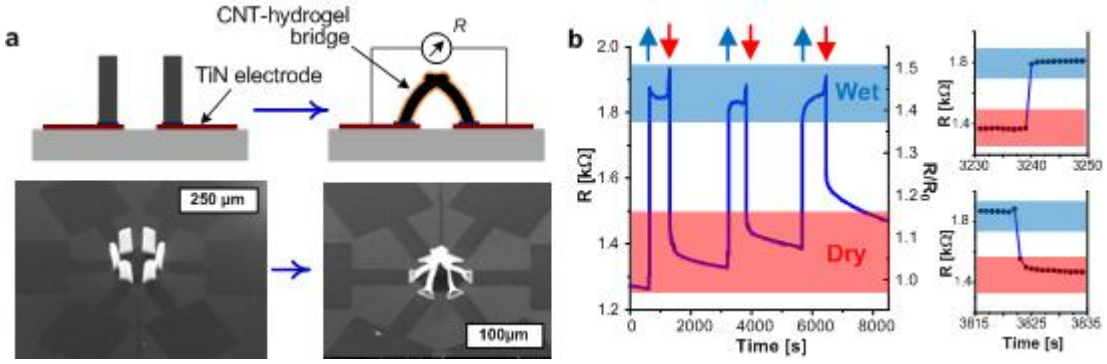

Figure 7.10 Integration of CNT-hydrogel microtransducers: (a) Schematic and SEM of multi-branched 3-D CNT transducer where the branches are electrically addressed by bottom TiN electrodes. (b) reversible resistance changes of CNT-hydrogel bridges, upon DI-H2O immersion.

Last, CNT-hydrogel composite microstructures can be used as integrated transducers with bottom electrode addressability. We fabricated electrically integrated CNT-hydrogel bridges by patterning the CNT growth catalyst on TiN electrodes. After capillary forming, the bridges were infiltrated with hydrogel, and then sealed by plasma bonding a PDMS microchannel over the substrate, as shown in **Figure 7.10**. The apex of each bridge forms a suspended sensing junction. Upon flow of water into the microchannel, the resistance measured across the bridge increases by 230%. Reversible resistance changes were also measured for multi- leg bridge structures like those shown in **Figure 7.10**. The resistance change occurs because swelling of the hydrogel increases the space among the CNTs within the bridge, which modulates transport through nanoscopic lateral CNT-CNT contacts that inherently have a high sensitivity to separation distance. Therefore, this sensor design utilizes the anisotropy of the aligned CNTs within the composite to enable high sensitivity electrical measurement of shape

changes. The resistance change likely occurs throughout the bridge as well as at the apex where the structures contact. This sensitive CNT joint is discussed in more details in Chapter 9.

The sensor response also provides insight on the dynamics of the hygrotropic CNT-hydrogel structures. While hydrogels alone swell and shrink relatively slowly, **Figure 7.10** shows that the CNT-hydrogel bridge sensor nearly reaches steady-state within 1 second of wetting and drying. This is more than 10 times faster than previously reported for bulk CNT-hydrogel composites.[13] Essential for this fast response is the 3D suspended geometry of the bridge and the alignment of the CNTs which speeds water uptake and release. Further, the time constant of hydrogels is typically approximated as $\tau \sim r^2/D$ where r is the characteristic dimension of the hydrogel and D is the cooperative diffusion coefficient.[14] Due to the square dependency of the time constant with the dimensions, scaling down of the composite structures will further improve reaction times, and this can be readily achieved by fabricating smaller CNT frameworks by lithography.

7. 6 Bibliography

1. De Volder, M.; Tawfick, S. H.; Park, S. J.; Copic, D.; Zhao, Z. Z.; Lu, W.; Hart, A. J., Diverse 3D Microarchitectures Made by Capillary Forming of Carbon Nanotubes. *Advanced Materials* **2010,** *22* (39), 4384-4389.

2. LaFratta, C. N.; Fourkas, J. T.; Baldacchini, T.; Farrer, R. A., Multiphoton fabrication. *Angewandte Chemie-International Edition* **2007,** *46* (33), 6238-6258.

3. Zeng, J. J.; Saltysiak, B.; Johnson, W. S.; Schiraldi, D. A.; Kumar, S., Processing and properties of poly(methyl methacrylate)/carbon nano fiber composites. *Composites Part B* **2004,** *35* (2), 173-178.

4. Garcia, E. J.; Hart, A. J.; Wardle, B. L.; Slocum, A. H., Fabrication and nanocompression testing of aligned carbon-nanotube-polymer nanocomposites. *Advanced Materials* **2007,** *19* (16), 2151-+.

5. Coleman, J. N.; Khan, U.; Blau, W. J.; Gun'ko, Y. K., Small but strong: A review of the mechanical properties of carbon nanotube-polymer composites. *Carbon* **2006,** *44* (9), 1624-1652.

6. Tawfick, S.; Deng, X. P.; Hart, A. J.; Lahann, J., Nanocomposite microstructures with tunable mechanical and chemical properties. *Physical Chemistry Chemical Physics* **2010,** *12* (17), 4446-4451.

7. Volder, M. D.; Park, S. J.; Vidaud, D.; Tawfick, S.; Vidaud, D.; Hart, A. J., Fabrication and electrical integration of robust carbon nanotube micropillars by self-directed elastocapillary densification. *Journal of Micromechanics and Microengineering* **2011,** *21* (4), 045033.

8. Tawfick, S.; O'Brien, K.; Hart, A. J., Flexible High-Conductivity Carbon-Nanotube Interconnects Made by Rolling and Printing. *Small* **2009,** *5* (21), 2467-2473.

9. De Volder, M.; Tawfick, S. H.; Copic, D.; Hart, A. J., Hydrogel-driven carbon nanotube microtransducers. *Soft Matter* **2011**.

10. Burgert, I.; Fratzl, P., Plants control the properties and actuation of their organs through the orientation of cellulose fibrils in their cell walls. *Integrative and Comparative Biology* **2009,** *49* (1), 69-79.

11. Fratzl, P.; Elbaum, R.; Burgert, I., Cellulose fibrils direct plant organ movements. *Faraday Discussions* **2008,** *139*, 275-282.

12. Montheard, J. P.; Chatzopoulos, M.; Chappard, D., 2-HYDROXYETHYL METHACRYLATE (HEMA) - CHEMICAL-PROPERTIES AND APPLICATIONS IN BIOMEDICAL FIELDS. *Journal of Macromolecular Science-Reviews in Macromolecular Chemistry and Physics* **1992,** *C32* (1), 1-34.

13. Yang, Z. H.; Cao, Z.; Sun, H.; Li, Y., Composite films based on aligned carbon nanotube arrays and a poly(N-isopropyl acrylamide) hydrogel. *Advanced Materials* **2008,** *20* (11), 2201-+.

14. Skotheim, J. M.; Mahadevan, L., Physical limits and design principles for plant and fungal movements. *Science* **2005,** *308* (5726), 1308-1310.

Chapter 8
Properties of CNT-CNT joints

In this chapter the mechanical and electrical properties of macro-scale CNT sheets are studied. Specifically, cm size sheets of HA-CNTs are fabricated by rolling and capillary densification of VA-CNT line patterns. The sheets comprise overlapping CNT stripes of 200 to 300 μm length, and SEM images indicate that the CNT bundles from the overlapping stripes interpenetrate after capillary densification. By varying the overlapping dimensions, the characteristics of the interactions at the CNT joints are studied. Tension tests on CNT strips (width =500 μm; thickness = 2 μm, length = 4 mm) showed strength and stiffness of 60 and 600 MPa respectively. These properties are of the same order as those previously measured for individual CNT microstructures (with no joints), therefore demonstrating the strong CNT-CNT interactions within these highly ordered assemblies. The measured current-voltage (*I-V*) trends for CNT sheets confirm Ohmic behavior of the CNT joints. Further, the resistivity of cm-scale sheets is on the same order as the segments of continuous CNTs (< 10 mΩ-cm), demonstrating that sheet resistivity is limited by the resistivity of the CNTs and not the joints. Thus, understanding the characteristics of the CNT joints bridges the gap between the micro- and macro-scale CNT materials. Moreover, the CNT joints properties can be enhanced by mechanical twisting which enables the fabrication of more robust yarns with higher shear stiffness and strength; and they can be tailored by chemical coating/doping to harness their large contact area in sensing and energy storage.

8. 1 Limits and potential of macro-scale CNT materials

While individual CNTs have exceptional properties, the properties of CNT assemblies suffer from scaling difficulties. This is due to inadequate control of the CNT

length and diameter distribution within CNT assemblies, and due to variations in CNT packing density and interconnection. In particular, the strength and toughness of CNT fibers are limited by macro-scale defects affecting the adhesion of the CNTs to one another and hence their collective load-bearing capacity. This has been reported by Li and colleagues for CNT yarns made by direct spinning CNTs from a gas phase reactor.[1] By testing 10 to 20 µm diameter yarns in tension to fracture, a bimoldal distribution of strength values was found: 1 GPa and 8 GPa for yarns of 20 mm and 1 mm gauge length respectively (**Figure 8.1**). It was suggested that the millimeter gauge lengths were close to the average length of individual CNTs within the fiber, and therefore these short "fibers" were closer to the intrinsic properties of individual continuous CNTs.

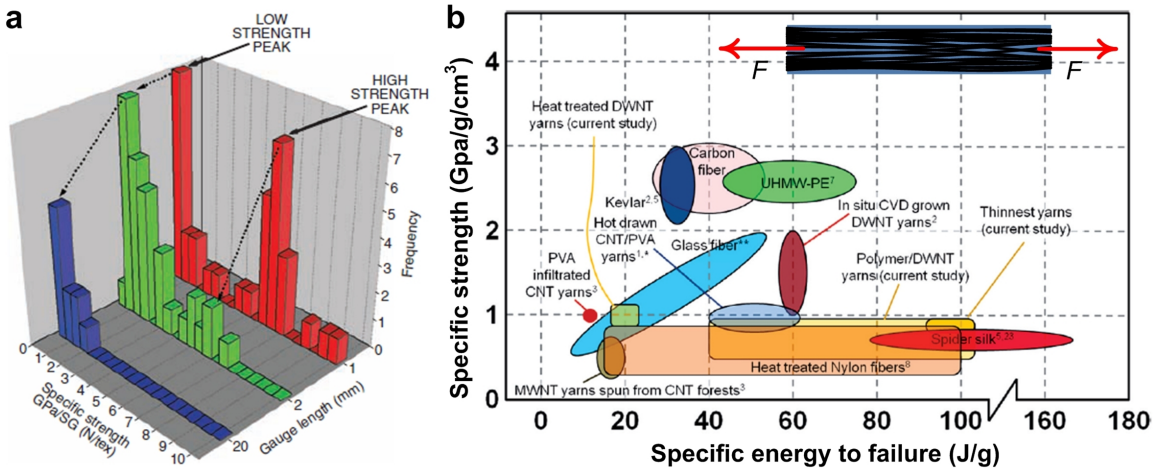

Figure 8.1 Mechanical properties of CNT yarns. (a) Best reported CNT yarns showing low strength al 20 mm gauge length and bimodal strength at 1 and 2 mm gauge length which highlights the defect density in these yarns.[1] (b) Comparison of specific strength and specific energy to failure of best CNT yarns to several standard yarn materials.[2]

A recent study by Naraghi et al. provides further insight on the load transfer and failure mechanisms of CNT fibers.[2] In this study, fibers of double-wall CNTs (DWNTs) were spun from tangled CNT films first produced by thermal CVD on substrates, thereby mimicking the gas-phase production process. By measuring the load-displacement characteristics of individual DWNT bundles from within the mats, in comparison to the characteristics of the fibers themselves, it was shown that the tensile strength of DWNT bundles is 8X higher than the fiber strength. Therefore, fiber strength is severely limited by CNT-CNT interfaces, and not by the properties of individual CNTs. Further, the CNTs were incidentally coated by a thin polymer layer by pyrolysis within the CVD

furnace. A comparison of mechanical properties after this layer was removed by oxidation of the fibers showed that even nanoscale polymer interfaces between mating CNTs impart significantly higher fiber toughness. Analogous to the behavior of natural nanocomposites such as nacre, the polymer layer shears under tensile deformation of the fiber, and the contrast in properties between the filament (CNT) and the matrix isolates nanoscale flaws. This permits very large energy absorption before failure of the material. The relationship between strength and toughness for extant CNT fibers and other materials is summarized in **Figure 8.1**b, emphasizing there is a significant opportunity for improvements.

Further, the lack of precise control over CNT assembly hinders understanding of the collective interactions among the CNTs which govern the ultimate scalable properties of CNT-based materials. These properties depend on the CNT organization and the type/quality of interactions among nearby CNTs. Therefore, to achieve ultimate CNT materials, we must develop new methods of precisely assembling long CNTs to give tight packing and strong interconnection, and concomitantly understand the governing mechanisms of collective CNT properties at the macro scale.

The electrical conductivity of CNT films is another example of the scaling challenge of CNT based materials. Large area thin CNT films have a great potential for use in transparent conducting films,[3] battery electrodes,[4, 5] flexible interconnects,[6] and electrically conductive polymer composites. However, the electrical conductivity of CNT networks is limited by conductivity of the intersecting CNT joints (S_{JT} =1/contact resistance). For example, for networks of randomly aligned CNTs exceeding the percolation threshold[1], experiments show that the conductivity increases with increased CNT length.[7] This indicates that charge transport is favorable in conducting paths consisting of longer CNTs and lesser joints. The network conductivity in this regime is said to be limited by S_{JT}. On the other hand, if the conductivity were nearly independent of the CNT length, the network properties would be limited by S_{CNT}. For random CNT networks, this is found to follow a power law with the CNT length ~$L_{CNT}^{2.5}$.

[1]Percolation is a statistical measure indicating whether a network of CNTs reached the required interconnectivity for having uniform electrical conductivity. It is used to predict the conductivity of CNT films and polymer-CNT composites as a function of the CNT weight fraction.

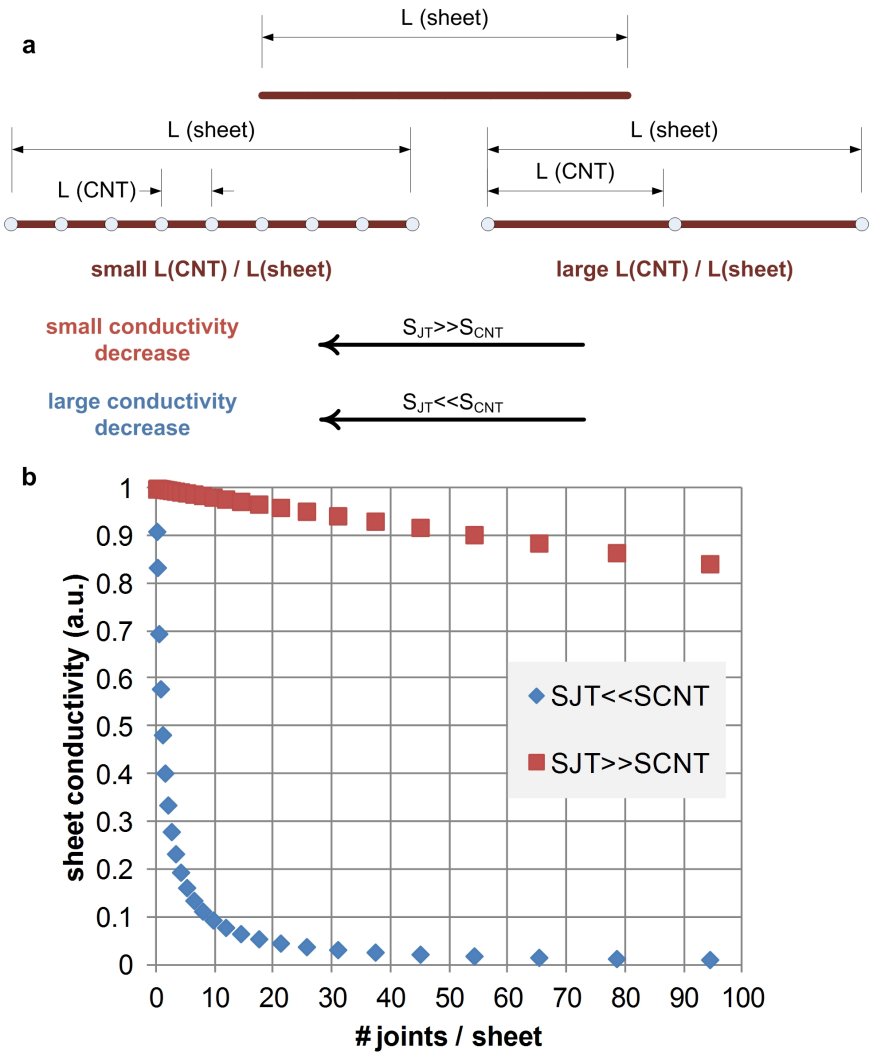

Figure 8.2 1-D model of CNT sheet conductivity. (a) Schematic of the model where the same CNT length comprises from one to a large number of joints.

A simple 1-D model is formulated to understand the effect of the CNT joints resistance on the properties of cm scale HA-CNT sheets. The model illustrated in **Figure 8.2** consists of continuous micro-scale CNT (conductivity S_{CNT}) joint by point-contact resistance (conductivity S_{JT}). Simulations show a sharp decrease (following a power law) in sheet conductivity with increased number of CNT joints for $S_{JT} << S_{CNT}$ and a linear decrease for sheets with $S_{JT} >> S_{CNT}$. In fact, the CNT joints made by overlapping CNT stripes are expected to have several contact points along the overlapping length and hence

S_{JT} os dependent on the overlapping architecture. This is discussed in more details in Section 9.3.

Here, we use rolling and capillary densification of CNT line patterns to fabricate cm scale HA-CNT sheets. After rolling, the CNT line patterns are overlapping thus creating aligned CNT-CNT joints. Therefore, cm scale CNT sheets are used as model systems to understand the mechanical and electrical properties of joints of aligned CNTs.

8. 2 Mechanical stiffness and strength of CNT joints

VA-CNT line patterns were grown by CVD, rolled and densified by condensation and evaporation of acetone. **Figure 8.3** shows a CNT sheet with 50% overlap. This is defined as

$$\%\ overlap = \frac{height_{CNT} - line\ spacing}{line\ spacing}$$

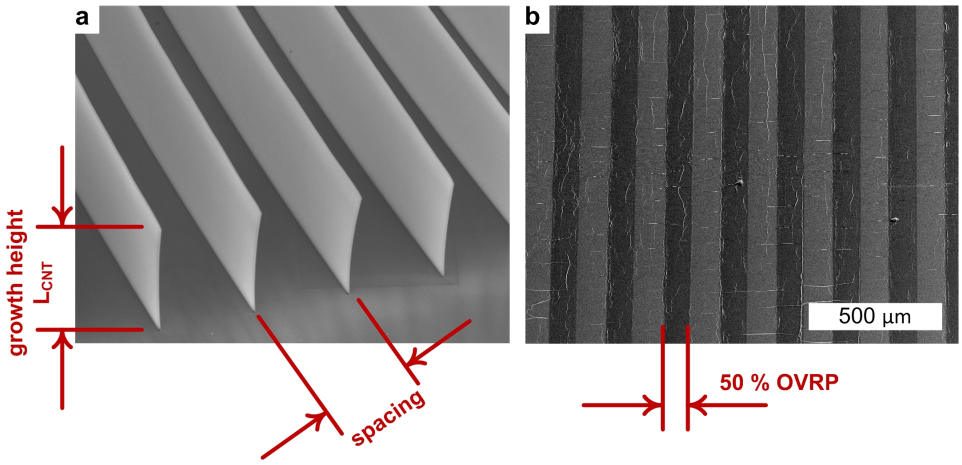

Figure 8.3 HA-CNT sheets. (a) Line patterns of VA-CNTs. (b) HA-CNT sheet with 50% overlap.

High resolution SEM images show that the capillary densification causes the CNTs to interpenetrate in the overlap region therefore enhancing the contact area among CNTs at the joint as shown in **Figure 8.4**. This is the same effect as the local aggregation seen in capillary forming, but here the surface forces during evaporation aggregate the CNTs

from different bundles because they are already in intimate contact after mechanical rolling.

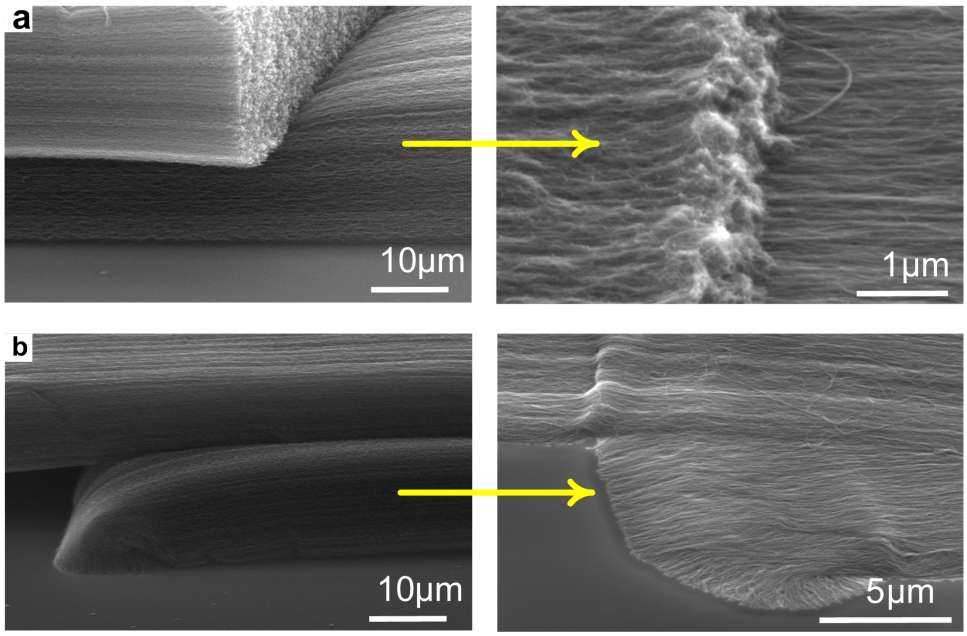

Figure 8.4 Mechanocapillary joining of CNTs by rolling and overlapping. (a) The top and (b) the bottom of overlapping CNT stripes showing the CNT interpenetration at the joint after capillary joining.

The sheets were cut into strips of approximately 0.5 mm width using a sharp razor blade. The termination step in the growth was selected to lead to low CNT-substrate adhesion as described in Chapter 3; thus these thin yarns could be pulled off the substrate using sharp tweezers or a tape. After peeling, copper SEM tape was used to contact one end of the stripe and to fix the CNT strip in the mechanical testing machine (**Figure 8.5c**). Mechanical testing was perfomed in the Dynamic Mechanical Analyzer (DMA) located in Professor Ellen Arruda's lab (**Figure 8.5b**).

The strips have 10 mm length. However, the gauge length during the different tests was about 2-3 mm and the remaining length was used to secure good contact to the tape, thus avoiding slip between the strip and the tape. During testing, if a strip failed at the boundary with the tape, the test was discarded. If the strip broke somewhere in the middle of the gauge length, the results from that test were analyzed.

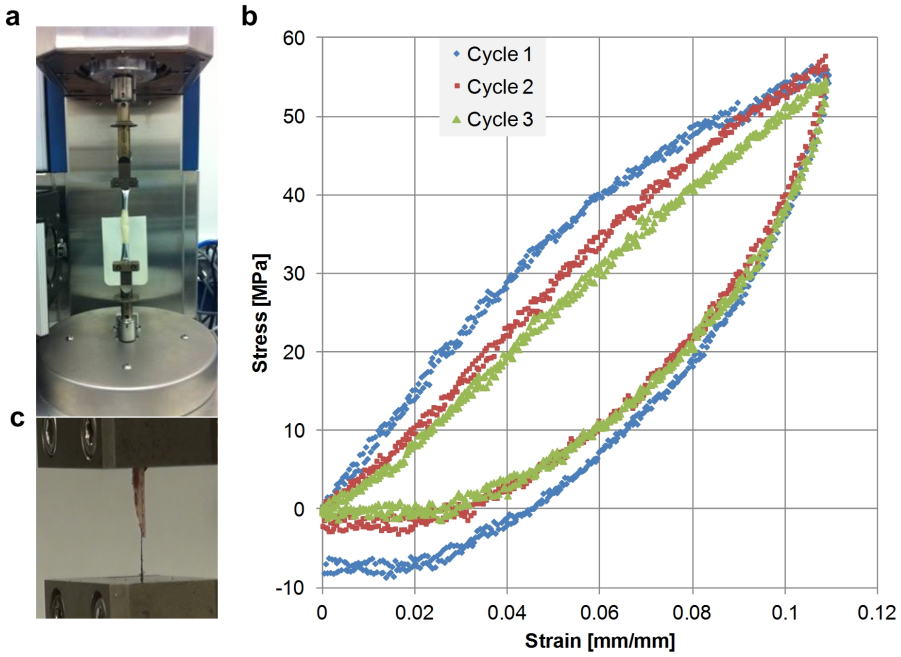

Figure 8.5 Mechanical stiffness of CNT strips. (a) DMA testing machine. (b) Optical image showing the CNT strip pulled between the chucks of the DMA. (c) Tree stress strain cycles of CNT strip (width = 0.5 mm, height = 3 mm, thickness = 2 µm)

The measured stress-strain relation for a 3 mm gauge length strip with 40% overlap is shown in **Figure 8.5a**. Three load-unload cycles were performed for the strip. After the first cycle, the gauge length was increased by 4% as seen for the x-axis intercept of the first cycle's unloading curve. This may have been due to initial rearrangement of the CNTs as discussed later. During the second and third cycles, less extension to the gauge length was observed. During loading, the stress-strain relation is linear. The elastic modulus is 750 MPa for the first cycle until about 5% strain, and then the slope decreases and the elastic modulus is 470 MPa at the maximum strain of 11 %. The strip reaches the same stress-strain value at the end of each cycle. The unloading curve is not linear indicating that there is a small amount of irreversible strain in the strips after testing. After the unloading cycle, the shape of the curve during the following loading cycle changes showing an initial decrease in slope. These observations indicate that some slip occurs during each cycle. The negative value of the load seen in particular after the first cycle also indicates the extension in the strip's length during the loading cycles. This extension caused the strip to slightly buckle as the chuck move to the zero-displacement location. As long as the magnitude of the slip is smaller than the % overlap, the strip

doesn't break; and in fact the changes in the strip stiffness are minimal after many cycles for strains of ≈11 %. The mechanism responsible for the robustness of the strips even after the slip events is discussed in more details next in light of the strength measurements.

Table 8.1 Calculated stiffness, strength and energy stored and dissipated for cycles 1 to 3.

	stiffness		strength		max. energy		energy dissipated		
	MPa	$N.Tex^{-1}$	MPa	$N.Tex^{-1}$	J/m^3	$J.g^{-1}$	J/mm^3	$J.g^{-1}$	%
Cycle 1	750	5.00	57	0.38	0.0120	80	0.0087	58	73
Cycle 2	550	3.67	57	0.38	0.0108	72	0.0065	43	60
Cycle 3	500	3.33	55	0.37	0.0095	64	0.0049	33	52

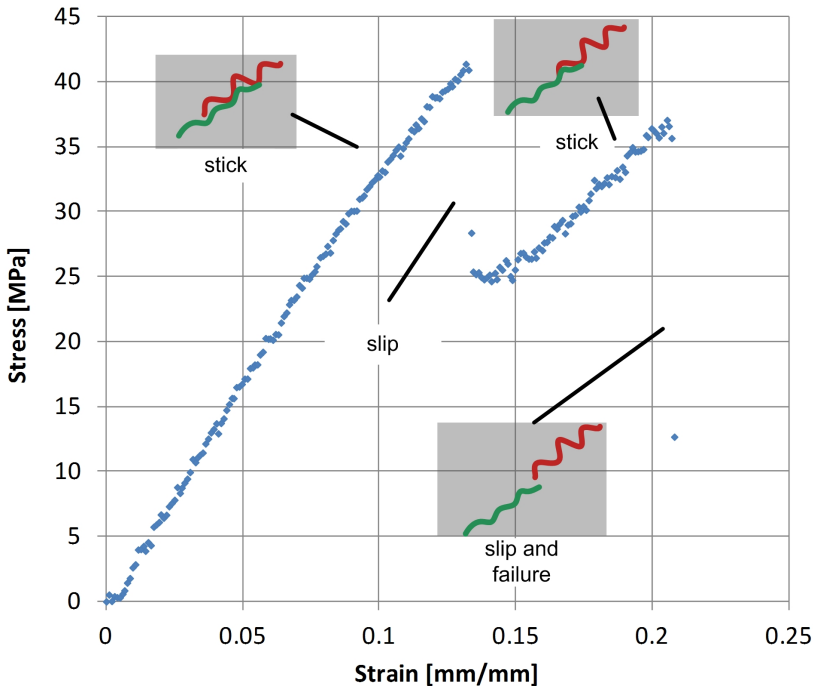

Figure 8.6 Mechanical strength of CNT strips. Stress-strain curves for the CNT strips show distinct continuities followed by stiffness recovery as the loading proceeds. These can be explained by stick-slip mechanism of CNTs at the joints as shown in the schematics. When the total slip exceeds the overlapping length, total separation and failure occurs.

The strips were also tested to failure to determine their strength and response at large strain values. **Figure 8.6** shows an exemplary tension test on a 3 mm gauge length CNT strip. The loading curve has a discontinuity in the stress value at 13% strain. However,

the strip didn't break. In fact, as the chuck displacement continued, the strip was pulled straight again until another discontinuity occurred at which the strip broke after reaching 21% strain. Notably, the change in slope after the discontinuity is small (only a few %). This strip strength and stiffness of this sample are 42 MPa and 330 MPa respectively. The SEM images of this strip (**Figure 8.7**) show that it failed due to CNT tearing within the stripes and at the interpenetrated joints. Length measurements of the overlapping stripes show no signs of slip except at the location of the failure where large slip lengths are observed. Also, high resolution SEM of the interpenetrated joint where slip is not observed shows no signs of joint tear.

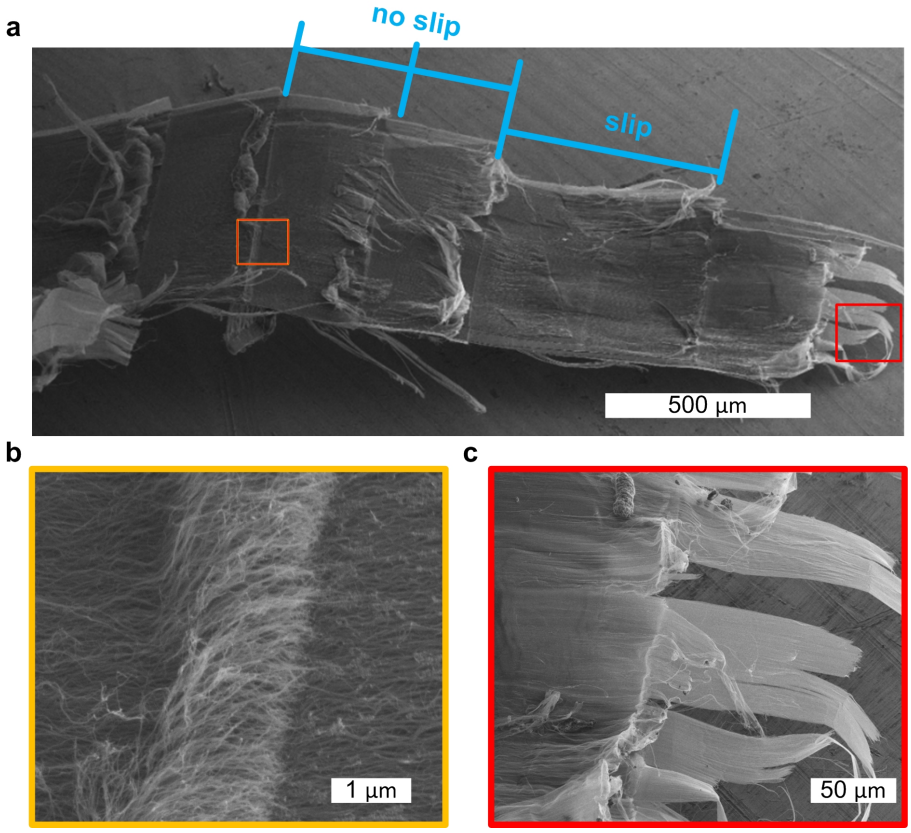

Figure 8.7 SEM showing the CNT strip after failure. (a) the strip where the location of slip is indicated. (b) High resolution SEM of a CNT joint showing no signs of tearing. (c) SEM showing that ht e failure is characterized by CNT tearing and separation at the joint.

The measured strength and stiffness of multi-segment CNT strips are comparable to previous measurements of individual VA-CNT microstructures prepared in our growth system. The individual microstructures (which have continuous CNTs and no joints)

have maximum strength and stiffness of 70 MPa and 1.7 GPa.[8] The maximum strength and stiffness of CNT strips with interpenetrated joints described in this study are 60 MPa and 750 MPa. The results indicate that interpenetrated CNT joints formed by rolling and capillary densification of CNT line patterns can withstand large shear stresses. As indicated by the SEMs of **Figure 8.7**, failure can occurs within the CNTs themselves and at the interpenetrated joints following Mode II toughness failure mechanism of joints (in-plane shear). The difference in the strength between the continuous CNT microstructures and the long strips with interpenetrated joints is remarkably low. This indicates that the strength in both test specimen architectures (continuous and overlapping CNTs) is limited by the same mechanism. Notably, it is known that CNT bundles fail at low strength due to weak load transfer among the individual CNTs within the bundle. This is confirmed by the observation of sword-sheath failure mode where the CNT within the bundles separate from the CNTs at the circumference due to tension.[2, 9] Moreover, due to the entangled structure of the CNT from our growth process, only a small percentage of the CNTs within the bundle are fully extended and hence bearing the tension load. The mechanical strength for both continuous and overlapping CNT is therefore limited by the same mechanisms.

On the other hand, the stiffness of CNT strips is significantly lower than the continuous CNT microstructures. This may be due to nanoscale stick-slip events occurring as the load on the CNT strips is increased. This mechanism is typical for fibers based on hierarchical assembly of short fibers and has been studied for example in wood.[10] Stick-slip in wood fibers is characterized by the presence of discontinuities in stress-strain relations, after which the strips can almost restore their initial stiffness.

The results show a great promise for making CNT strips and other load-bearing CNT materials using this method. The properties of the interpenetrated joints can be enhanced by (i) chemical binding among the CNTs at the joints for example by coating and/or electron or ion irradiation; and/or (ii) twisting the strips thus enhancing the mechanical load-transfer mechanism among the individual CNT segments.

8. 3 Electrical conductivity of CNT joints

Large scale CNT sheets from HA-CNTs have potential applications ranging from organic conducting films to substrates with hierarchical aligned micro- and nanoscale topographies for biological tissue growth. The fabrication of the sheets is enabled by rolling, overlapping and capillary induced joining of CNTs. It is therefore to desirable to characterize the electrical conductivity at the joint interface.

To this end, CNT sheets with variable spacing and overlap were designed as described in **Figure 8.3**. VA-CNT lines were grown by CVD, rolled and capillary densified as described in Chapter 4. After preparing the sheets, Au electrodes (5 nm Ti / 400 nm Au) were deposited by sputtering through a shadow mask at the edges of the CNT sheets.

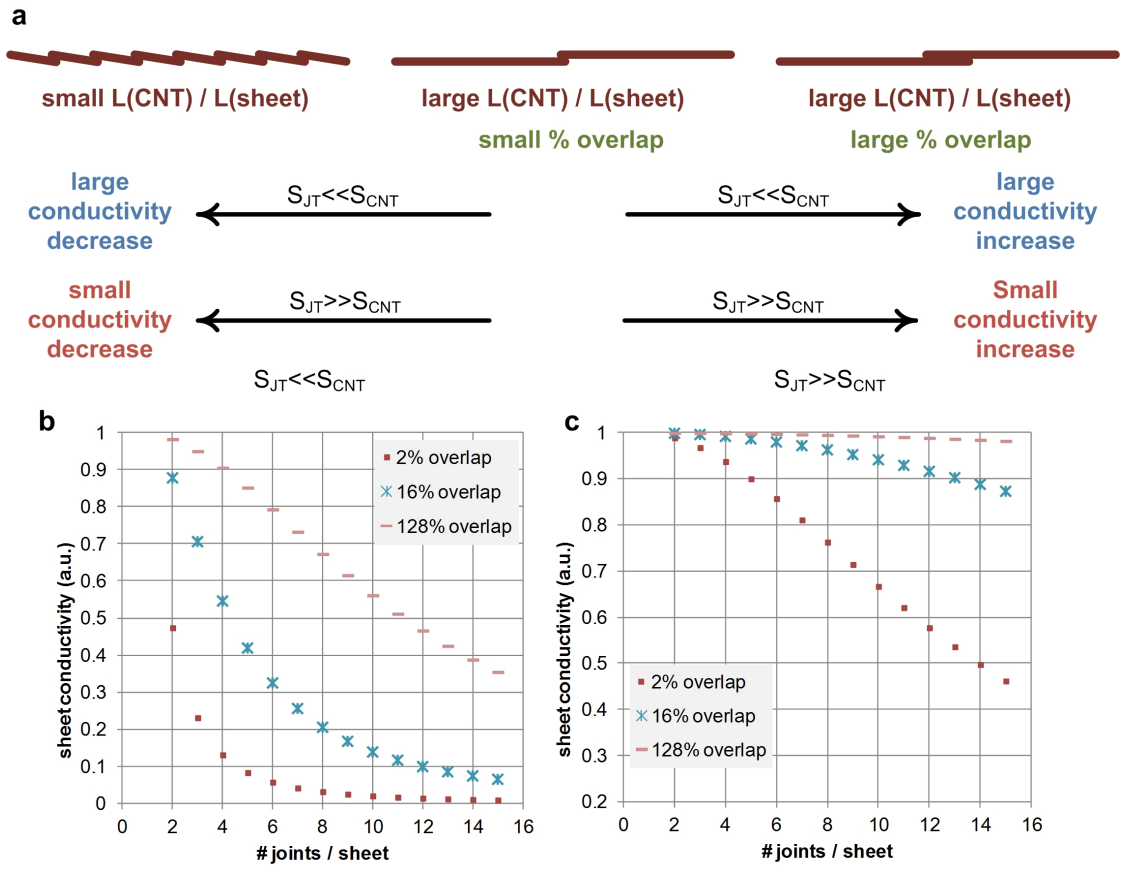

Figure 8.8 Electrical model of CNT sheet conductivity with various number and length of overlapping joints. (a) Schematic of the model showing the summary of the simulation results at the low (b) and high (c) S_{JT} limits.

The design of the CNT sheets takes into consideration the trends of electrical properties scaling discussed in Section 9.1. More specifically, in HA-CNT sheets made from overlapping stripes, the conductivity of the CNTs (S_{CNT}) and of the joint (S_{JT}) are coupled as shown in **Figure 8.7**. The joint conductivity by definition increases with contact area. Thus, CNT sheets with greater overlap can be expected to have higher overall. The enhancement resulting from increasing the overlap depends on the relative magnitudes of S_{CNT} and S_{JT} as shown in **Figure 8.7**. This model predicts that for CNT sheets with high S_{JT}, the relative enhancement in conductivity as a result of increasing the overlap from 16% to 128% is less than 10%. It also shows the potential of making CNT sheets having electrical conductivity approaching that of a single line by engineering the number of joints and the % overlap.

a

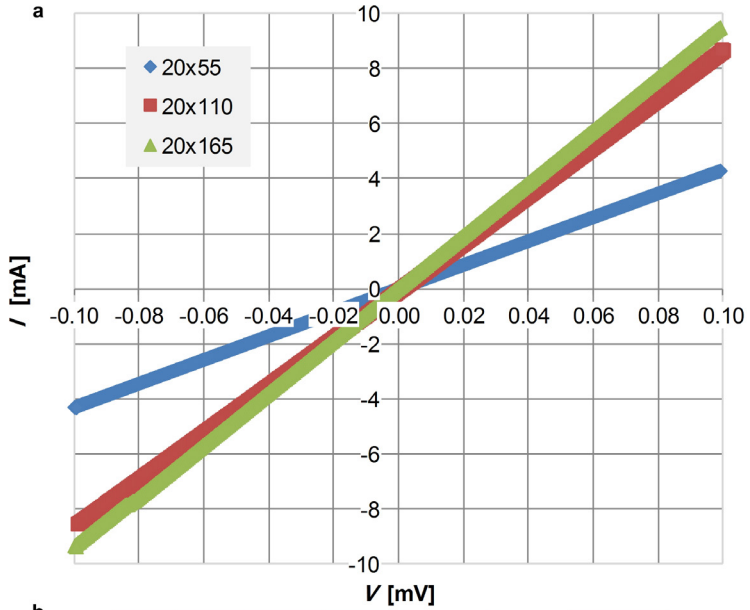

b

	20 x 55	20 x 110	20 x 165	
spacing	55	110	165	μm
# Joints	72	36	24	
% overlap	264	82	21	%
Contact resistance	0.1	0.1	0.1	mΩ-cm^2
Predicted Resistance	23.14	13.62	10.47	Ω
Measured Resistance	23	11.6	10.5	Ω

Figure 8.9 Electrical characterization of the CNT joint. (a) *I-V* measurement of CNT sheets with various number of joints and overlapping lengths (b) Table summarizing the electrical measurements of various CNT sheet designs.

To investigate the validity of the model, *I-V* curves were measured across the CNT sheets using a 2-probe setup by sweeping the voltage from -0.1 to 0.1 mV. The curves are linear which confirm that the contact among the CNT lines is Ohmic. The measurements were performed parallel to the alignment of the CNTs. The values in **Figure 8.8** show that a 2- and 3-fold increase in % OVLP leads to 43% and 57% decrease in the CNT sheet resistance. By comparison of these values to the curves in **Figure 8.2**, we conclude that the sheets characteristics follow the high S_{JT} trend. In fact, by substituting the measured values for the sheet resistivity into the model used to predict the trends shown in **Figure 8.2**, the value of R_{JT} is estimated to be 0.1 mΩ-cm^2. This value is 3-4 orders of magnitude higher than contact resistance between two polished metal surfaces with externally applied pressure. However, noting that the surface the CNT stripes is characterized by low surface density and high roughness, the value of the estimated S_{JT} is realistic and promising for the fabrication of large scale CNT sheets.

8. 4 Bibliography

1. Li, Y.-L.; Kinloch, I. A.; Windle, A. H., Direct Spinning of Carbon Nanotube Fibers from Chemical Vapor Deposition Synthesis. *Science* **2004,** *304* (5668), 276-278.

2. Naraghi, M.; Filleter, T.; Moravsky, A.; Locascio, M.; Loutfy, R. O.; Espinosa, H. D., A Multiscale Study of High Performance Double-Walled Nanotubeâˆ’Polymer Fibers. *Acs Nano* **2010,** *4* (11), 6463-6476.

3. Wu, Z.; Chen, Z.; Du, X.; Logan, J. M.; Sippel, J.; Nikolou, M.; Kamaras, K.; Reynolds, J. R.; Tanner, D. B.; Hebard, A. F.; Rinzler, A. G., Transparent, Conductive Carbon Nanotube Films. *Science* **2004,** *305* (5688), 1273-1276.

4. Wang, D.; et al., Highly oriented carbon nanotube papers made of aligned carbon nanotubes. *Nanotechnology* **2008,** *19* (7), 075609.

5. Reddy, A. L. M.; Shaijumon, M. M.; Gowda, S. R.; Ajayan, P. M., Coaxial MnO2/Carbon Nanotube Array Electrodes for High-Performance Lithium Batteries. *Nano Letters* **2009,** *9* (3), 1002-1006.

6. Cao, Q.; Hur, S. H.; Zhu, Z. T.; Sun, Y. G.; Wang, C. J.; Meitl, M. A.; Shim, M.; Rogers, J. A., Highly Bendable, Transparent Thin-Film Transistors That Use Carbon-Nanotube-Based Conductors and Semiconductors with Elastomeric Dielectrics. *Advanced Materials* **2006,** *18* (3), 304-309.

7. Hu, L.; Hecht, D. S.; Grí¼ner, G., Percolation in Transparent and Conducting Carbon Nanotube Networks. *Nano Letters* **2004,** *4* (12), 2513-2517.

8. Hill, F. A.; et al., Characterizing the failure processes that limit the storage of energy in carbon nanotube springs under tension. *Journal of Micromechanics and Microengineering* **2010,** *20* (10), 104012.

9. Filleter, T.; Bernal, R.; Li, S.; Espinosa, H. D., Ultrahigh Strength and Stiffness in Cross-Linked Hierarchical Carbon Nanotube Bundles. *Advanced Materials* **2011,** *23* (25), 2855-2860.

10. Keckes, J.; Burgert, I.; Fruhmann, K.; Muller, M.; Kolln, K.; Hamilton, M.; Burghammer, M.; Roth, S. V.; Stanzl-Tschegg, S.; Fratzl, P., Cell-wall recovery after irreversible deformation of wood. *Nat Mater* **2003,** *2* (12), 810-813.

Chapter 9
Fabrication and elastocapillary densification of silicon nanowires

This chapter describes the fabrication and elastocapillary densification of silicon nanowires (SiNWs). Films of vertically aligned (VA-) SiNWs were fabricated by Metal Assisted Chemical Etching (MACE). The MACE process creates single crystal nanowires that have potential applications in optical and electromechanical devices such as solar cells and transducers. Further this process can serve as platform for studying elastocapillary densification of nano-scale filaments. SiNWs with (100) orientation were fabricated by MACE using a metal salt in acid solution, and using a patterned metal mesh in an acid solution. The salt solution provides a facile approach to fabricate SiNWs without the need for pre-patterning. However the process results in a broad diameter distribution (40-200 nm). The process non-uniformity also leaves ridges that restrict the hierarchical aggregation of SiNWs during elastocapillary densification. Therefore a recently published process was adopted to use a nanoporous metal mesh template to accurately control the diameter and spacing. Metal meshes were fabricated by transferring the patterns of Anodic Aluminum Oxide (AAO) membranes with uniform pore diameters of 18 nm and 80 nm. The SiNW prepared by this method hierarchically aggregate into larger bundles which scale with the SiNW diameter and spacing as expected from elastocapillary aggregation theory. Finally, SiNW microstructures were fabricated by combining salt based MACE with standard photolithography and DRIE.

9. 1 SiNW by MACE using salt solution

MACE using salt solutions is the popular process for top-down fabrication of single crystal SiNW from a Si wafer.[1-3] The advantage of this method is the formation of SiNW in the range of 40 to 200 nm at low temperatures without the need to make any patterns (for example by lithography) or deposit metal films or catalysts.[4] The process consists of two steps: etching and cleaning. The etch bath consisted of 5M HF (hydrofluoric acid) and .04M $AgNO_3$ (silver nitrate) at 50℃. The Si wafer is cut into small pieces and cleaned right before the etching. Pre-etch cleaning was done by immersing in acetone for 10 minutes, 2-propanol for 5 minutes, and then hot piranha (H_2SO_4 3:H_2O_2 1) etch for 40 minutes. The samples were cleaned in DI-H_2O before transferred to the etch solution. The etching reaction proceeds as follows. The Ag^+ ions are reduced ($Ag^+ \rightarrow Ag$) forming nanoparticles on the surface of Si as they inject holes into the Si valence band thus locally oxidizing it ($Si \rightarrow SiO_2$) as illustrated in Figure 8.1. The etch rate is about 0.7 μm/min. Cleaning of the Si after etch is done in Aqua Regia (HNO_3 1: HCL 3) at 80°C for two hours to dissolve the metal nanoparticles.

In Figure 8.1, low and high resolution SEM images are shown for the SiNW forest etched for three hours. The images show that the SiNWs laterally deform and aggregate. However, the images also show that the aggregation morphology of the SiNWs is different from that of CNT forests[5, 6] or microscale bristles[7]. More specifically, The SiNWs don't form the cellular structure (foam) seen in densified CNT forests nor do they form separate hierarchical bundles as seen in the densification of bristles[7]. Instead, they tend to only bend and partially aggregate without forming individual bundles or leaving large voids in the pattern.

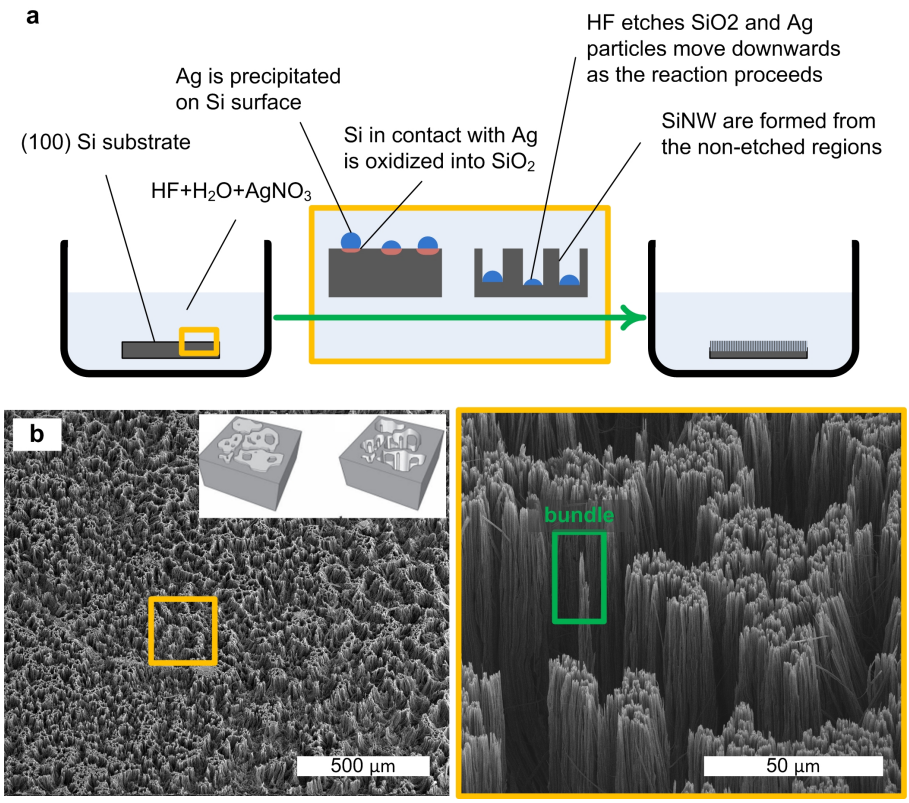

Figure 9.1 Fabrication of silicon nanowires (SiNWs) by Metal Assisted Chemical Etching (MACE) using salt solution. (a) MACE process schematic. (b) SEM image of SiNWs fabricated using the process in (a). Inset shows the non-uniform morphology of the Ag catalyst deposited from the solution. Image on the right is a high resolution SEM image showing the aggregation morphology of the SiNWs.

The schematic of the process shown in **Figure 9.1b** illustrates the shape of the SiNWs formed by MACE from salt solution. The schematic illustrates the presence of ridges between the nanowires which are caused due to the local variations in catalyst particle density. Because of their high lateral stiffness, these ridges (**Figure 9.8**) do not allow the bundles of SiNWs to freely bend to make larger bundles and reach the typical final aggregation morphology.[2] Instead, small pairs form and they locally aggregate around the stiff ridges and they form small bundles. The high resolution SEM of **Figure 9.1b** (right) shows a bundle forming where possibly the random fluctuations of particle density lead to an area of SiNWs free from ridges.

Experiments performed by Py et al on a model system consisting of micron sized filament assemblies having uniform diameter distribution and spacing show that the

filaments first bundle in pairs, then pairs form larger bundles and so on.[8] This hierarchical pairing continues until forming a large individual bundle. The final bundle diameter is shown to be ~ $(L/L_S)^{4/3}$ where L is the height of the filaments and L_S is their sticking height. The sticking height, also defined in Chapter 6, is the height of the filaments above the substrate at which they form a single aggregate. This depends on their diameter, spacing and contact angle with the liquid. Using the values of Table 9.1, the bundle size relation predicts that the bundle size for SiNW from the MACE process should be ~10 μm.[9] This is not seen in the SEM of **Figure 9.1**.

Table 9.1 The mechanical properties of SiNWs prepared by MACE using ($AgNO_3$+HF) in a MEMS testing cell inside the SEM chamber.

Material	**E (modulus)**	**Cross section form**	**Diameter**	**Spacing**	**Length**
CNT	~500 GPa	circular	8-14 nm	50-100 nm	150 μm
SiNW	~ 130 GPa	Non-uniform /ridges	40-200 nm	100 – 500 nm	150 μm

9. 2 SiNW by MACE using a metal mesh

To achieve better control on the diameter distribution, MACE can be performed using a pre-patterned metal mesh, which replaces the salt used in the first process.[10, 11] In this case, the etch solution consists of HF, H_2O_2 and DI-H_2O. The H_2O_2 (hydrogen peroxide) causes the local oxidation of Si at the metal-Si interface (Si → SiO_2). The metal mesh can be Au or Ag or a bilayer Au-Ag films. Ag leads to a higher etching rate than Au however is less chemically stable and hence it gets etched itself as the etching proceeds.[12]

To make a metal mesh with small pores (<100 nm) I adapted the method reported by Kim et al. using a commercially-available Anodic Aluminum Oxide (AAO) membrane.[12] AAO membranes of 18 nm and 80 nm pore diameter and 50 μm thickness were bought from Synkera (**Figure 9.2**).[13] The membranes are fabricated by standard electrochemical anodization process.[14] As-bought membranes were coated with bilayered film of Ag (20 nm) / Au (5nm) or Au only (20 nm) by sputtering. The coated membranes were then

gently placed on the surface of 0.1 M NaOH solution which etches completely dissolves the membrane in 45 minutes. The solution was carefully replaced using a syringe with DI-H_2O. This process results in the metal mesh floating on the surface of the water as shown in **Figure 9.2**. Before the membrane is transferred to the Si, it needs to be floated for a short time on the surface of an acidic solution. This is a critical step in this process. The bottom of the metal mesh (in contact with the solution) is very rough as shown in **Figure 9.3**. This is due to the surface roughness of the AAO membranes bought from Synkera and to the formation of small metal particles in the holes during sputtering. These two effects can lead to non-uniform etching or in some cases no etching at all. Thus, to clean the bottom of the mesh, it was left to float on diluted Aqua Regia (10 wt%) for 30-60 seconds. The acid was then replaced by DI-H_2O then transferred to clean Si as shown in **Figure 9.2**. The Si substrate with the metal mesh was placed in the etching solution consisting of 10M HF and 2 M H_2O_2 to form the SiNWs. The etching rate is approximately 0.5 µm/min.

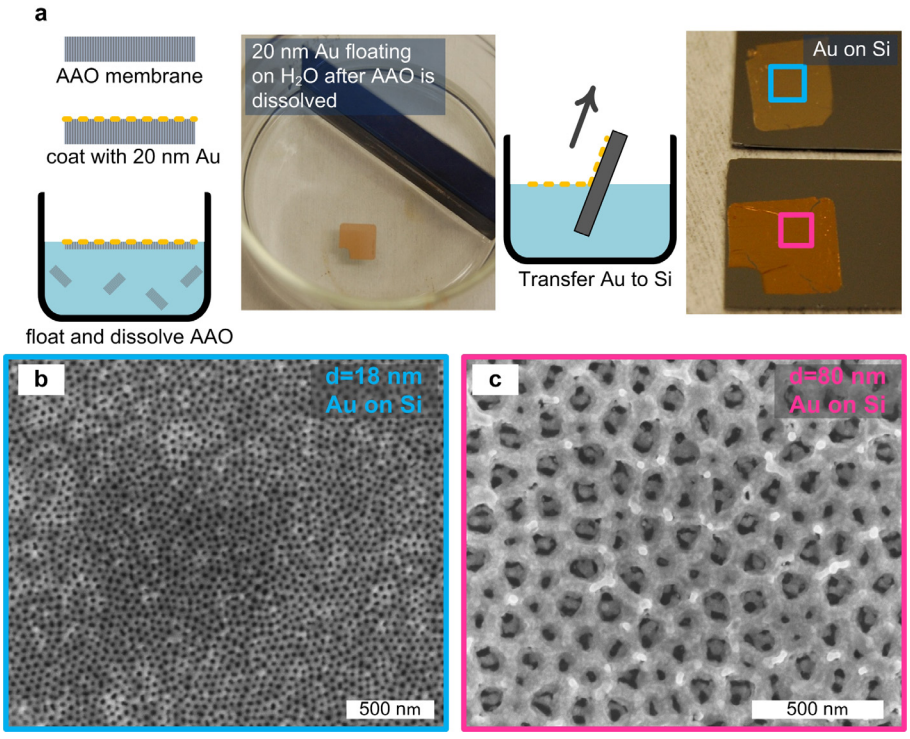

Figure 9.2 Fabrication of SiNWs by MACE using HF/H_2O_2 solution and a metal mesh. (a) MACE process schematic. Optical images show 20 nm thick metal mesh floating on the surface of water (left) and the metal mesh with 18 and 80 nm pore diameter after transfer to the Si (right). (b) 18 nm pore diameter Au mesh on Si. (c) 80 nm pore diameter metal mesh on Si.

Figure 9.4a shows a Au membrane with 80 nm pore diameter after the transfer to Si. **Figure 9.4b** shows the results from etching in the HF/H_2O_2 solution for 2 minutes followed by critical point drying. The image shows that the nanowires have uniform shape and diameter following the Au membrane. However, not all the holes have nanowires. This is due to the metal particles forming in the holes during sputtering, which are not 100% successfully removed during the acid etch step (**Figure 9.3**). Thus the silicon in these areas gets entirely etched away by the solution.

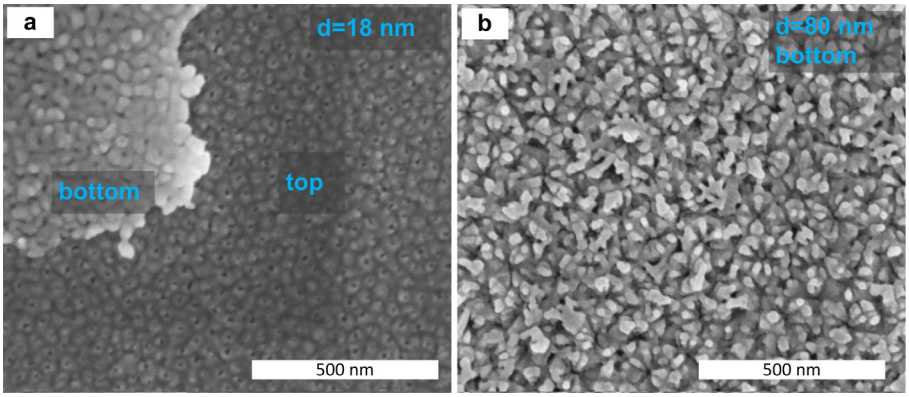

Figure 9.3 SEM image showing the surface morphology of the metal mesh. (a) SEM showing an 18 nm pore diameter Au mesh which was accidently folded. The bottom which was in contact with the Anodic Aluminum Oxide (AAO) membrane is rough and has nanoparticle sin the holes. (b) SEM showing 80 nm pore diameter Au mesh where the bottom side is rough.

The elastocapillary aggregation of the SiNW formed from AAO template mesh follows the theory very closely as shown in **Figure 9.5**. According to the relation described in Section 9.1, the 18 nm and 80 nm diameter SiNW should form individual bundles of 1.5 μm and 2.8 μm respectively. This is expected not only because of the uniformity in the SiNW diameter, but also because the nanowires are isolates (i.e., not connected by ridges as in the MACE result).

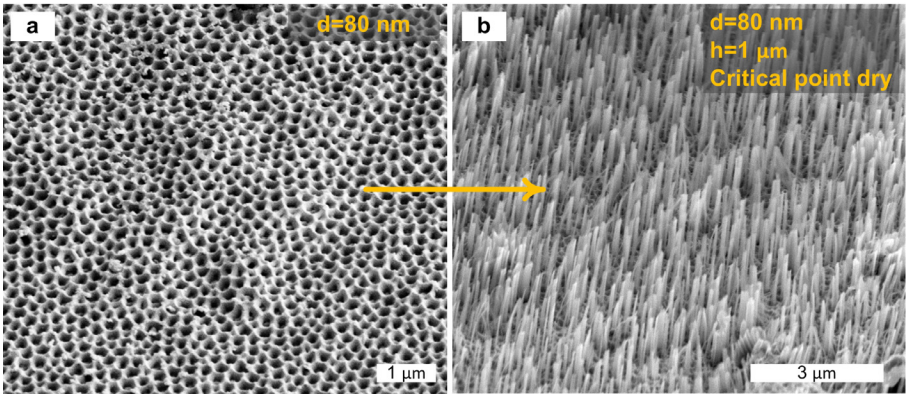

Figure 9.4 SEM image showing the morphology of the metal mesh and the resulting SiNWs. (a) 80 nm pore diameter metal mesh. (b) 80 nm diameter SiNW emerging from the pores.

Figure 9.6 shows the results of etching using 18 nm holes diameter mesh for two hours. The expected height is 60 µm. The SiNW aggregation in this case doesn't follow the expected bundle morphology. The SiNWs travel parallel to the substrate in a flat geometry before they aggregate into vertical geometries. Two types of vertical geometries are observed: short thin walls and short twisted bundles. The thin walls are similar to the thin walls forming the cellular morphology in the elastocapillary densified CNT forests. Py et al. discuss in their conclusion that the cellular morphology is a more complicated problem to study.[7] In fact, I expect that the walls and the twisted bundles are formed due to two types of interaction with the substrate. The first interaction is elastocapillary buckling, as discussed in Chapter 6.[15] When the wires height L is >> the elastocapillary height L_{EC}, the wires can buckle. As a result of this buckling, the wires come in contact with the substrate and stick to it. If the SiNW break and detach from the substrate, thin walls are formed. This is the case for morphology seen in capillary densified CNT forests. Alternatively, the SiNWs do not detach from the substrate and they travel long distances flat on the substrate before they meet and form short twisted bundles as shown in **Figure 9.6b**.

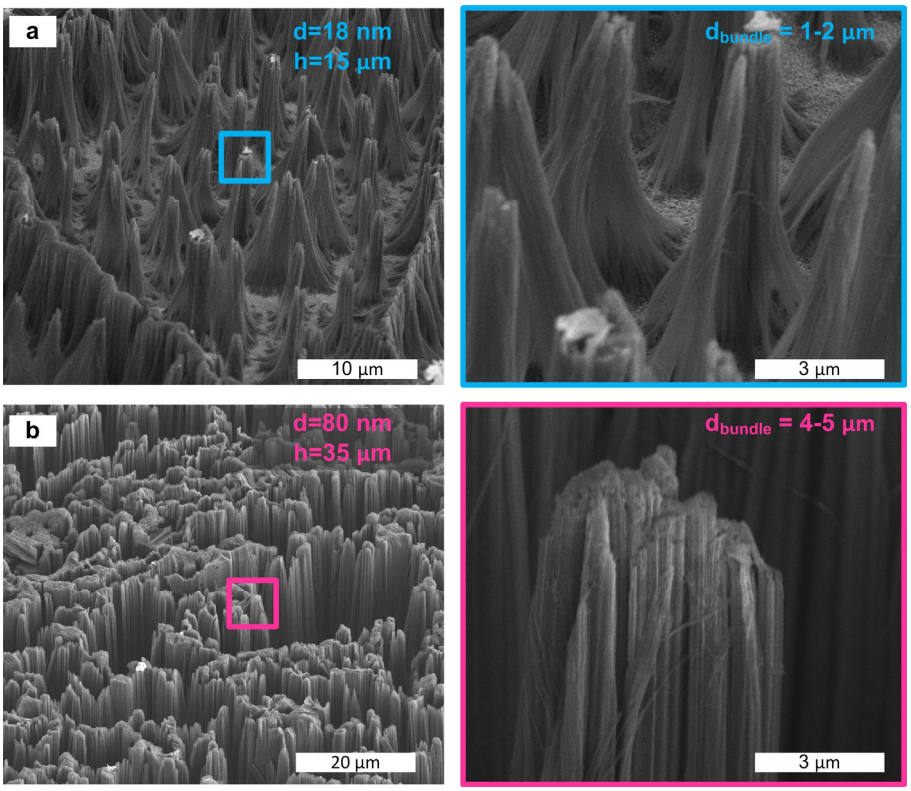

Figure 9.5 SEM showing the elastocapillary aggregation of SiNWs using a metal mesh. (a) Aggregation morphology for 18 nm diameter SiNWs having 15 µm height. Right frame showing high resolution image of the formed bundles with 1-2 µm diameter. (b) Aggregation morphology for 80 nm diameter SiNWs having 35 µm height. Right frame showing high resolution image of the formed bundles with 4-5 µm diameter.

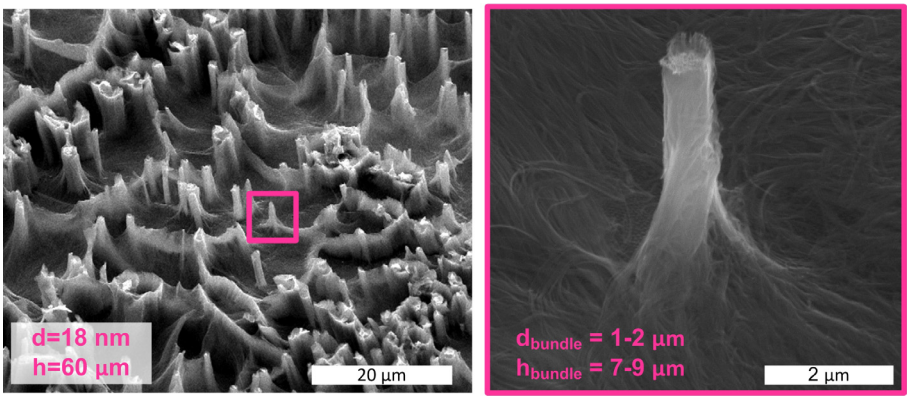

Figure 9.6 SEM showing the aggregation morphology of high aspect ratio SiNWs. (a) Aggregation morphology for 18 nm diameter SiNWs having 60 µm height. Right frame showing high resolution image of the twisted bundles.

9. 3 Fabrication of SiNW microstructures by MACE

Attempts were made toward making 3-D SiNW structures by capillary forming.[16] Combination of MACE and microfabrication can be used to fabricate SiNW microstructures. **Figure 9.7** shows the process schematic and results. The first step in process consists of fabricating Si microstructures using standard photolithography and Deep Reactive Ion Etching (DRIE). The last step in the DRIE etch is set to deposit (C_4F_8 flow for 15 s) a thin layer of Teflon on the substrate. This thin layer can protect the side walls and the substrate ground from being etched with MACE. After cleaning the substrate in acetone and O_2 plasma RIE for a short time, the top surface of the Si microstructures are exposed. The substrate is then submerged in the salt ($AgNO_3$) based MACE etching solution. **Figure 9.7b** shows the Si microstructures with Ag nanoparticles on top of the microstructures after a short etch. The image demonstrates how the Ag particles are formed on top of the Si microstructures before the etching of the SiNWs proceeds.

The results after etching the microstructures for 10 minutes are shown in **Figure 9.8**. The images show that the SiNWs are formed in the microstructures. They also form interconnected ridges which prohibits the formation of the expected elastocapillary morphology as discussed in Section 9.1.

Alternatively, the Au metal mesh can be transferred to the substrate with the Si microstructures fabricated by DRIE (without the C_4F_8 deposition step) as shown in **Figure 9.9a**. The samples were cleaned with O_2 plasma and piranha after DRIE. Interestingly , the metal mesh remains suspended across up to 10x10 arrays of closely spaced Si micropillars (space < 10 μm). (**Figure 9.9b** and **c**). The result after etching HF-H_2O_2 solution for 30 minutes is shown in **Figure 9.9d**. The metal mesh breaks and falls on the substrate. Surprisingly, the metal mesh etches SiNWs on the substrate but not on the Si microstructures (where etching is desired).

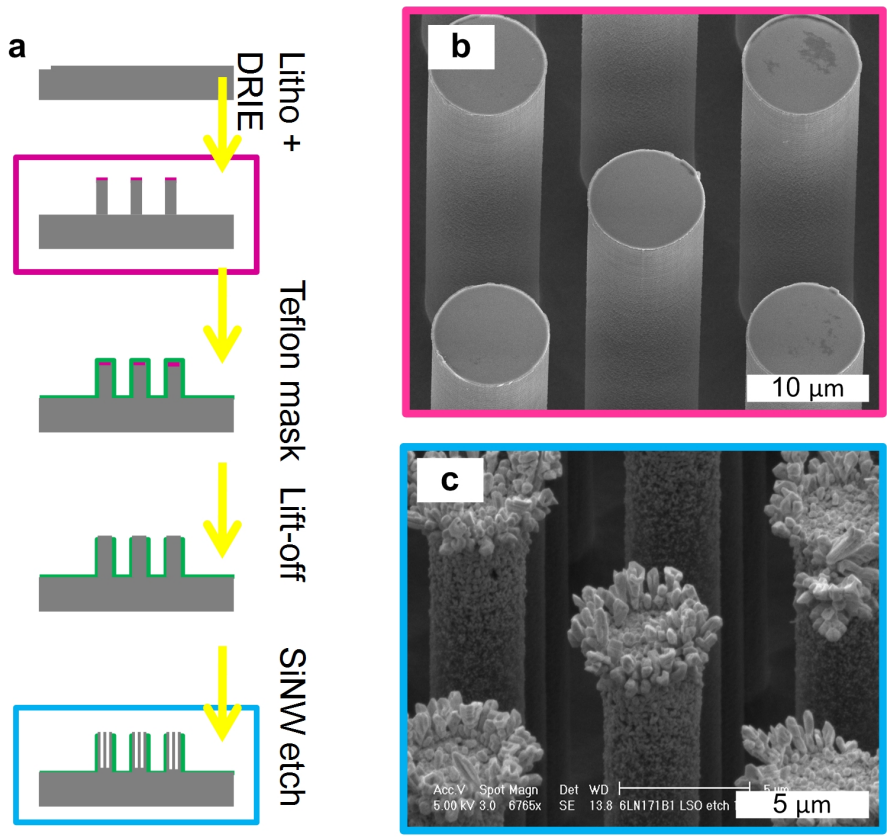

Figure 9.7 Fabrication of SiNW microstructures by MACE using salt solution. (a) Process schematic. (b) SEM image showing 10 µm diameter Si microstrcutures fabricated by DRIE. (c) SEM image showing Ag nanoparticles deposited on top of the Si microstructures from the salt solution.

A close examination of the metal mesh on the top of the Si microstructures offers insights into the mechanism responsible for suppressing the etching of the microstructures while allowing it everywhere else. The metal mesh is wrapping around the sidewalls of the Si microstructure. The mechanism of etching relies on the metal mesh "piercing" into the Si while the SiNWs emerge from within the holes where no etching occurs. In the case of **Figure 9.9d**, the mesh on top of the Si microstructure is constrained due to sidewall wrapping. The etching would proceed if the mesh breaks at the edges of the top surface so it is not constrained. The effect of boundary condition of the metal catalyst on MACE has been studied by Wong et al. In particular, they patterned thin lines of photoresist on a Au film before they placed the samples in the etching solution. By doing this, not only did they suppress the etching below the photoresist (as expected) but also the etching of the exposed parts of the film didn't proceed as expected.

The film slightly bent downwards (**Figure 2.6**) like a simply supported beam and the etching self terminated.

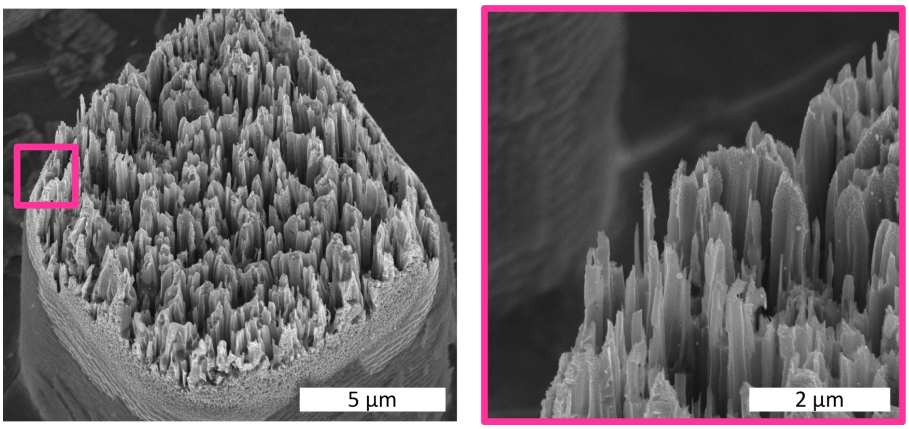

Figure 9.8 SEM images of SiNW microstructures by MACE using salt solution. (a) SEM image showing that the SiNW etching occurs only within the Si microstructure. (b) High resolution SEM image showing the ridge morphology restricting the elastocapillary aggregation of the SiNWs. [Images taken by Sibu Kuruvilla, NNIN-REU summer 2010]

This indicated that by mechanically constraining the metal film, the etching can be suppressed. This is the effect seen in the un-etched Si microstructures shown in **Figure 9.9d**. Thus, to overcome this effect, the metal mesh has to precisely cut to the shape of microstructure before MACE. This can be done by developing a photolithography process for patterning the mesh before DRIE. In this approach, the process steps would proceed in the following order: (i) prepare and transfer the mesh on un-patterned Si substrate (**Figure 9.2**), (ii) photolithography and etching of the metal mesh to form (for example 10 µm diameter circular) micropatterns, (iii) Form Si microstructures by DRIE, (vi) remove photoresist and clean all contamination that would affect MACE, and (v) submerge substrate (having Si microstructures with the metal mesh on top) in MACE to form SiNWs. Overcoming the contamination of the metal mesh surface and of the metal-Si interface during microfabrication is expected to be the main challenge that needs to be overcome.

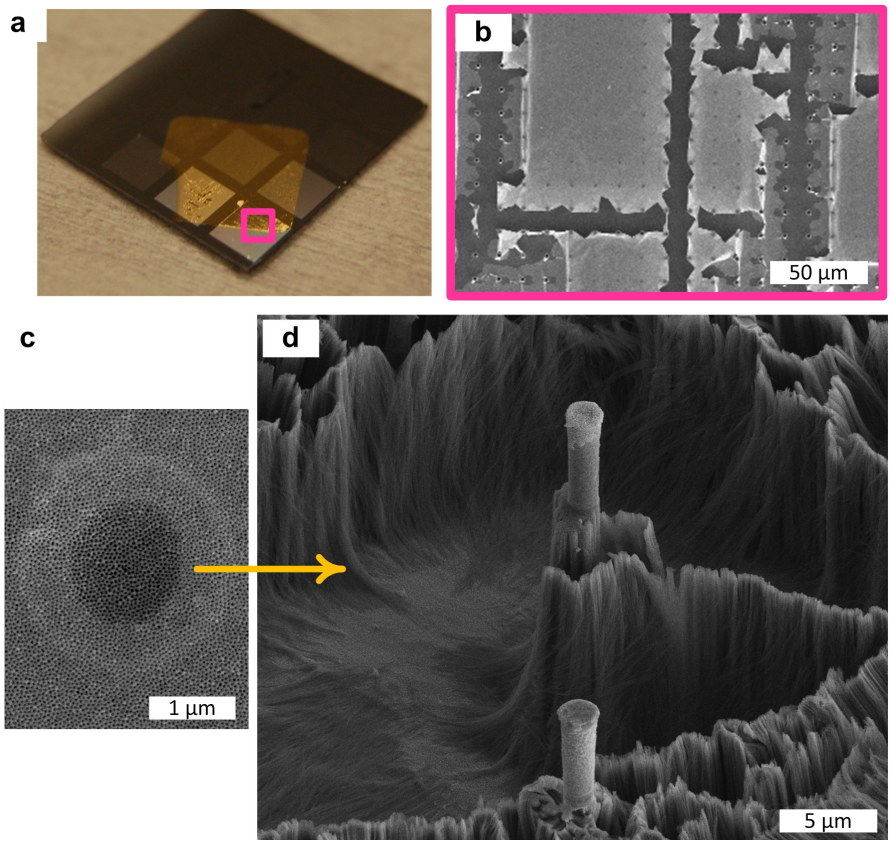

Figure 9.9 Fabrication of SiNW microstructure by MACE using a metal mesh. (a) Transfer of the metal mesh on a Si substrate having microstructures fabricated by DRIE. (b) SEM image of the mesh partially suspended across the Si microstructures. (c) SEM image of the metal mesh on 3 µm diameter microstructure. (d) SEM image showing SiNW are etched on the bottom of the substrate but not on top of the Si microstructure. The metal mesh wraps the side walls of the Si microstructures.

9. 4 Bibliography

1. Peng, K. Q.; Yan, Y. J.; Gao, S. P.; Zhu, J., Dendrite-assisted growth of silicon nanowires in electroless metal deposition. *Advanced Functional Materials* **2003,** *13* (2), 127-132.

2. Huang, Z.; Geyer, N.; Werner, P.; de Boor, J.; Gösele, U., Metal-Assisted Chemical Etching of Silicon: A Review. *Advanced Materials* **2010,** *23* (2), 285-308.

3. Peng, K. Q.; Fang, H.; Hu, J. J.; Wu, Y.; Zhu, J.; Yan, Y. J.; Lee, S., Metal-particle-induced, highly localized site-specific etching of Si and formation of single-crystalline Si nanowires in aqueous fluoride solution. *Chemistry-a European Journal* **2006,** *12* (30), 7942-7947.

4. Hochbaum, A. I.; Chen, R.; Delgado, R. D.; Liang, W.; Garnett, E. C.; Najarian, M.; Majumdar, A.; Yang, P., Enhanced thermoelectric performance of rough silicon nanowires. *Nature* **2008,** *451* (7175), 163-167.

5. Chakrapani, N.; Wei, B. Q.; Carrillo, A.; Ajayan, P. M.; Kane, R. S., Capillarity-driven assembly of two-dimensional cellular carbon nanotube foams. *Proceedings of the National Academy of Sciences of the United States of America* **2004,** *101* (12), 4009-4012.

6. Liu, H.; Li, S.; Zhai, J.; Li, H.; Zheng, Q.; Jiang, L.; Zhu, D., Self-Assembly of Large-Scale Micropatterns on Aligned Carbon Nanotube Films. *Angewandte Chemie International Edition* **2004,** *43* (9), 1146-1149.

7. Py, C.; Bastien, R.; Bico, J.; Roman, B.; Boudaoud, A., 3D aggregation of wet fibers. *EPL (Europhysics Letters)* **2007,** *77* (4), 44005.

8. Py, C.; Reverdy, P.; Doppler, L.; Bico, J.; eacute; Roman, B.; icirc; Baroud, C. N., Capillary Origami: Spontaneous Wrapping of a Droplet with an Elastic Sheet. *Physical Review Letters* **2007,** *98* (15), 156103.

9. Dongfeng, Z.; Breguet, J. M.; Clavel, R.; Sivakov, V.; Christiansen, S.; Michler, J., In Situ Electron Microscopy Mechanical Testing of Silicon Nanowires Using Electrostatically Actuated Tensile Stages. *Microelectromechanical Systems, Journal of* **2010,** *19* (3), 663-674.

10. Peng, K. Q.; Zhang, M. L.; Lu, A. J.; Wong, N. B.; Zhang, R. Q.; Lee, S. T., Ordered silicon nanowire arrays via nanosphere lithography and metal-induced etching. *Applied Physics Letters* **2007,** *90* (16).

11. Huang, Z.; Zhang, X.; Reiche, M.; Liu, L.; Lee, W.; Shimizu, T.; Senz, S.; Goƶˆsele, U., Extended Arrays of Vertically Aligned Sub-10 nm Diameter [100] Si Nanowires by Metal-Assisted Chemical Etching. *Nano Letters* **2008,** *8* (9), 3046-3051.

12. Kim, J.; Han, H.; Kim, Y. H.; Choi, S.-H.; Kim, J.-C.; Lee, W., Au/Ag Bilayered Metal Mesh as a Si Etching Catalyst for Controlled Fabrication of Si Nanowires. *Acs Nano* **2011,** *5* (4), 3222-3229.

13. http://www.synkera.com/ceramic-membranes/symmetric-membranes.html.

14. Routkevitch, D.; Bigioni, T.; Moskovits, M.; Xu, J. M., Electrochemical Fabrication of CdS Nanowire Arrays in Porous Anodic Aluminum Oxide Templates. *The Journal of Physical Chemistry* **1996,** *100* (33), 14037-14047.

15. Tawfick, S.; De Volder, M.; Hart, A. J., Structurally Programmed Capillary Folding of Carbon Nanotube Assemblies. *Langmuir* **2011,** *27* (10), 6389-6394.

16. De Volder, M.; Tawfick, S. H.; Park, S. J.; Copic, D.; Zhao, Z. Z.; Lu, W.; Hart, A. J., Diverse 3D Microarchitectures Made by Capillary Forming of Carbon Nanotubes. *Advanced Materials* **2010,** *22* (39), 4384-4389.

Chapter 10
Findings and next steps

10. 1 Thesis contributions

The thesis comprised three main efforts: the development of various fabrication processes for manipulating CNTs and SiNW using mechanical and capillary forces; investigation of the liquid surface forces and the material stresses governing the mechanics of organization and interactions in filamentary materials; and characterization of the electrical and mechanical properties of mechanocapillary formed and/or coated CNTs. The major contributions can be summarized as follows:

Methods for fabrication of VA-CNT microstructures

- Development of standard procedures for photolithographic patterning and deposition of CNT growth catalyst by e-beam evaporation or sputtering.
- Determination of key variables affecting the CVD growth process of CNTs, such as the effect of the annealing recipes and their interplay with ambient humidity; and accordingly modifying the standard recipes to suppress adverse ambient effects.
- A systematic study of the effects of pattern size and density on growth of VA-CNT microstructures, which determined that the growth rate is increased for dense patterns but is less correlated to pattern sizes >100 μm^2.

Methods to coat VA-CNTs with polymers and ceramics, and therefore modify their structural properties

- Development of ceramic coating by Atomic Layer Deposition of Al_2O_3 to enhance the mechanical properties of CNT microstructures.

- Development of functional and reactive coatings (with Xiaopei Deng) by CVD of nanoscale conformal layers of parylene to enhance the chemical functionality of CNT microstructures.
- Precise control of the mechanical stiffness of VA-CNT using thin polymer coatings and the development of models to predict the changes in mechanical properties.

Fabrication of HA-CNT films by mechanical rolling

- Design and fabrication of a bench-top CNT rolling machine able to accommodate rollers with arbitrary diameter and hence roll short and tall VA-CNTs.
- Fabrication of high density HA-CNT interconnects with controlled placement and dimensions.
- Transfer printing of HA-CNT to arbitrary (e.g. plastic, flexible) substrates using dry PDMS stamps without carrier films.
- Joining VA-CNT line patterns by rolling, overlapping and capillary induced interpenetration, thus making HA-CNT sheets with cm-scale dimensions.

Fabrication of 3-D CNT microarchitectures by capillary forming

- Co-invention (with A. John Hart and Michael De Volder) of the capillary forming of 3D fabrication by manipulating CNT microstructures by controlled condensation and evaporation of solvents.
- Design of precisely controlled 3-D CNT geometries programmed by catalyst shape, structural modifications and coatings; and the identification of design rules for making void free robust 3-D CNTs.
- The in situ imaging and understanding of capillary forming process dynamics, along with identification of how the interactions among internal and external capillary forces and the CNT structural properties governing the capillary forming process.
- Development of the capillary folding method for fabricating multi-directional multilayered HA-CNT films and studying the mechanics of instability of thin CNT structures.

- Development of standard procedures for the integration of 3-D CNTs with microfabrication including photolithography, polymer infiltration, metal patterning and plasma etching.
- Characterization of the enhancements in mechanical stiffness and electrical conductivity resulting from capillary forming and/or polymer infiltration; and fabricating CNT-polymer composites with the highest reported stiffness (CNT-PMMA composites of 25 GPA).
- Development (with Michael De Volder) of CNT-hydrogel transducers, along with in situ observation of their shape-directed actuation due to changes in ambient humidity.

Understanding and control of the characteristics of CNT-CNT joints

- Measurements of the mechanical strength, stiffness and electrical conductivity of cm scale CNT sheets and comparison of their performance to individual CNT microstructures.
- Preliminary understanding of the mechanics of CNT joints and identification of the stick-slip interactions which improve the maximum allowable strain without compromising the strength; and decrease the stiffness due to nanoscale slip.
- Measurements of the DC conductivity of CNT joints and the identification of interpenetration of CNTs which explain the high conductivity of the overlapping sheets; due to. Thus, to enhance the properties of CNT sheets the quality of individual CNTs must be improved.

Fabrication and elastocapillary densification of SiNWs

- Synthesis of single crystal SiNW by Metal Assisted Chemical Etching, and precise control of their dimensions using a nanoporous AAO mask.
- Observation of the morphology of elastocapillary aggregation of SiNWs as related to their structure, diameter, spacing and height.

The outcomes of the thesis wouldn't have been as fruitful and rewarding without collaborating with outstanding and enthusiastic fellow students and post-docs. Countless discussions and coordinated experiments led to the current advancement and

understanding of mechanocapillary forming. And, in addition to the work presented here, several major collaborative milestones and ongoing directions are mentioned below.

- Erik Polsen and Ryan Oliver: Systematic identification and control of the effect of ambient pressure and water vapor content on the growth. Motivated by the nuisance caused by these variations, Erik and Ryan led the reference growth study which I contributed to by designing the experiments and analyzing the data.
- Jong Ok: I worked with Jong to fabricate hybrid CNT-ZnO nanowires sheets and characterize their photoelectric properties.[1]
- Megan Roberts: I worked with Megan to fabricate HA-CNT sheets which she used to understanding the effect of hierarchical nanoscale topology on the growth of motor neurons.
- Sei Jin Park: I worked with Sei Jin on designing a low pressure/temperature chamber which he fabricated and used to precisely control the condensation and evaporation of acetone thus enabling better control of the capillary forming process.
- Eric Meshot and Keval Patel: I worked with Eric and Keval to fabricate various HA- and 3-D CNTs patterns which they used to understand the crystallization and orientation of C60 rods on CNT topography, resulting in hybrid C60-CNT structures.[2]
- Davor Copic: I worked with Davor to fabricate 3-D CNTs and design the material system to replicate them in polymers; he then developed a process for uniform large area replication molding of 3-D CNT microstructures.[3]
- Zhouzhou Zhao and Professor Wei Lu: I worked closely with them to identify the mechanics involved in capillary forming; they then built numerical models for the collective bending and shape changes seen in the process.[4]
- NNIN-REU[1] students: Michael Moebius (2008) CNT nanoporous filters; Alex Hryn (2009) ALD coating of CNTs; Sibu Kuruvilla (2010) SiNW synthesis; Yuki Matsuoka (2011) Effect of pattern size and density on CNT growth.

[1] National Nanotechnology Infrastructure Network-Research Experience for Undergraduates program

- Michael De Volder (last but not least, co-inventor and enthusiastic leader of capillary forming): I worked with Michael to fabricate and characterize corrugated 3-D CNTs by cycling the growth and capillary forming processes. Using this process soft CNT springs with precisely tunable mechanical stiffness were fabricated.[5] Michael also integrated CNT-hydrogel sensors in microfluidic devices for electrical sensing of solvent chemistry.[6] And, we are currently developing various new techniques to fabricate bent and helical CNTs by controlling the catalyst support layer morphology and offset. This is complementary to my efforts with Yuki Matsuoka to understand the effect of gradient in growth rate on VA-CNT microstructure bending during growth.

10. 2 Future directions

Capillary forming offers a unique combination of scalability and specificity as a microfabrication process, and shows the promise to harness the attractive properties of CNTs in micro- and cm scale applications. A myriad of devices and applications are yet to be explored to harness the properties of capillary-formed structures. I consider the most important of which to be:

- Shape changing surfaces and MEMS transducers. The CNT-hydrogel actuation described in Chapter 7 is an attractive framework for the electrical transduction of chemical and mechanical changes in a material system. In particular, the lateral electrical conductivity (perpendicular to the axial direction) in aligned CNTs results from CNT interactions and is hence very sensitive to both mechanical and chemical changes in the material. For example, proteins could bind to specifically attached functional groups; and changes in spacing and contact resistance among the tubes could be electrically measured with great sensitivity due to the high surface area of CNTs.
- 3-D CNTs could make anisotropic surfaces for directional wetting and adhesion. Directional wetting is the ability to arbitrary control the wetting of liquids in all directions. Owing to hierarchical 3-D geometries, capillary formed CNTs could make surfaces with arbitrary topographies and precisely designed wetting characteristics such as surfaces that passively transport liquids and droplets to

specific directions or into particular points. This would be useful for open channel microfluidic and lab-on-a chip for point of care diagnostics.

- 3-D CNTs could be used as scaffolds to guide tissue growth. The nanoscale topography aligned to complex microscale geometries could be used as hierarchical scaffolds for mechanically, chemically and/or electrically guiding tissue growth.
- The properties of CNT-CNT joints made by rolling and capillary interpenetration demonstrate the potential to fabricate large scale yarns and sheets with outstanding performance. In particular, the mechanical strength and stiffness could be enhanced by twisting and/or coating and binding, which could result in performance exceeding the best organic yarns. Further, the architectures of the CNT joint and skeletal muscles are similar which motivates the studies of artificial muscles based on CNT joints. In fact, the contraction of muscles by the relative actin-myosin motion is comparable to the stick-slip mechanism of CNT joints; except that the latter is currently irreversible. Thus attaching a mechano-chemical group to the CNTs at the joint could lead to reversible high stroke actuation.

The findings of this thesis also raise many important scientific questions. It is known that the enhancement in the measured properties of CNT microstructures is due to the density increase and the enhancement in interactions among the CNTs. The former is understood and can be measured. The latter is not.

- What are the interactions among the CNTs? Are there chemical interactions between them (chemical bonds)? Could these interactions be quantified?
- How do these interactions affect the mechanical and chemical properties in different directions?
- How do they change (quantitatively) with diameter, density and alignment?
- Could the mechanical interactions be modeled using classical (constitutive) material properties? For example, in Chapter 6, the effect of the shear modulus of the CNT material on capillary forming is discussed. Is the modulus constant or changes with strain?

The properties of the CNT microstructures show that there still is a vast room for potential improvements in their performance. Specifically, the scaling trends presented in Chapter 2 (for example for CNT interconnects) demonstrate that the best results in this thesis are still far from the expected properties of the corresponding packing fraction of high quality CNT assembles.

- Why?
- Could we precisely measure the quality of the CNTs grown using our current CVD process? And could the measured quality be accurately correlated to the observed electrical and/or mechanical properties?
- Are the inner walls of the CNTs actively bearing mechanical load (in tension, compression, and shear)? Are they transporting electrical current?

Therefore, future directions should continue working on fabricating the ultimate CNT material by capillary forming. Before this can be achieved, the following improvements are needed:

- Achieve better control on the CNT growth process. Uncontrolled variations in CNT growth repeatedly restricted our efforts to precisely measure the materials properties or understand the material response to capillary forces. Variations due to ambient conditions are currently being addressed. For example, water vapor content in the growth gases should be monitored and at least a consistent baseline should be achieved. Other variations that are yet to be discovered include the as deposited catalyst composition and morphology.
- Have an accurate and reliable technique to measure the quality of the MWCNTs (e.g. defect density) to guide our efforts to making the ultimate CNT materials. The trends (G/D peak ratio) currently obtained from Raman spectroscopy do not offer reliable means to quantitatively measure the quality of the CNTs.
- The alignment of the CNTs limits the mechanical properties of the capillary formed microstructures and the CNT joints. Tension tests revealed that only a fraction of the CNTs are bearing the loads due to the high entanglement. Hence, growth leading to better alignment needs to be achieved.

- Based on the questions regarding the internal walls role in transport and mechanical performance, capillary forming of single walled CNTs would lead to a higher performance.

Second, while the work of this thesis (with all the fruitful collaborations and team work) led to good understanding of capillary forming, this understanding needs to be tested and evaluated by numerical models which focus on precisely taking into consideration the interactions among the CNTs as previously discussed. For example, the basic material properties (elastic and shear moduli and Poisson's ratio in all three directions as a function of applied strain) of the as-grown and densified CNTs need to be accurately measured and incorporated in the numerical models. Robust material properties models can lead to the design of new capillary forming geometries and shapes which enable the fabrication of new 3-D geometries with outstanding engineered properties.

During the past four years, I became fascinated with the mechanics of interactions and organization of filaments. I found various sources of exciting inspiration in cellular biology (e.g. the cell cytoskeleton and microtubules[7]), animal physiology (e.g. muscles and tendons of the turkey[8]), and plant mechanics and actuation (e.g. actuation of pine cones and wheat awns, and hierarchical wood mechanics[9, 10]). These readings influenced my perspective of the research topic and catalyzed ideas for future directions. For example, understanding CNT-CNT joints is not only useful to fabricate CNT yarns and sheets with outstanding properties, but also to transfer this understanding to other filamentary materials. Might we use our current understanding of nanoscale filamentary materials and interactions to understand the mechanics of the cytoskeleton network organization and growth involved in cell proliferation and tissue growth? or mechanism and forces of passively actuated plants?

I hope to investigate these and other questions in the near future.

10. 3 Bibliography

1. Ok, J. G.; Tawfick, S. H.; Juggernauth, K. A.; Sun, K.; Zhang, Y.; Hart, a. J., Electrically Addressable Hybrid Architectures of Zinc Oxide Nanowires Grown on Aligned Carbon Nanotubes. *Advanced Functional Materials* **2010,** *20*, 2470-2480.

2. Meshot, E.; Patel, K.; Tawfick, S.; Juggernauth, A.; Bedewy, M.; Verploegen, E.; Volder, M. D.; Hart, A. J., Photoconductive hybrid films via directional self-assembly of C60 on aligned carbon nanotubes. *Advanced Functional Materials* **2011,** (in press).

3. Copic, D.; Park, S. J.; Tawfick, S.; De Volder, M. F. L.; Hart, A. J., Fabrication of high-aspect-ratio polymer microstructures and hierarchical textures using carbon nanotube composite master molds. *Lab on a Chip* **2011,** *11* (10), 1831-1837.

4. Zhao, Z.; Tawfick, S. H.; Park, S. J.; De Volder, M.; Hart, A. J.; Lu, W., Bending of nanoscale filament assemblies by elastocapillary densification. *Phys. Rev. E* **2010,** *82* (4), 041605.

5. De Volder, M. l. F. L.; Tawfick, S.; Park, S. J.; Hart, A. J., Corrugated Carbon Nanotube Microstructures with Geometrically Tunable Compliance. *Acs Nano* **2011**, null-null.

6. De Volder, M.; Tawfick, S. H.; Copic, D.; Hart, A. J., Hydrogel-driven carbon nanotube microtransducers. *Soft Matter* **2011**.

7. Reymann, A. C.; Martiel, J. L.; Cambier, T.; Blanchoin, L.; Boujemaa-Paterski, R.; Thery, M., Nucleation geometry governs ordered actin networks structures. *Nature Materials* **2010,** *9* (10), 827-832.

8. Roberts, T. J.; Marsh, R. L.; Weyand, P. G.; Taylor, C. R., Muscular force in running turkeys: The economy of minimizing work. *Science* **1997,** *275* (5303), 1113-1115.

9. Keckes, J.; Burgert, I.; Fruhmann, K.; Muller, M.; Kolln, K.; Hamilton, M.; Burghammer, M.; Roth, S. V.; Stanzl-Tschegg, S.; Fratzl, P., Cell-wall recovery after irreversible deformation of wood. *Nat Mater* **2003,** *2* (12), 810-813.

10. Fratzl, P.; Burgert, I.; Gupta, H. S., On the role of interface polymers for the mechanics of natural polymeric composites. *Physical Chemistry Chemical Physics* **2004,** *6* (24), 5575-5579.